Rafael Roldán Toro

Electronic Correlations Effects in Layered Two-Dimensional Materials

Dissertion submitted for the degree of Ph.D. in Physics

Universidad Autónoma de Madrid (Spain)

Advisor: Mª Pilar López Sancho
Tutor: Guillermo Gómez Santos

Madrid, Junio 2007

Resumen

En este trabajo se estudian los efectos de la interacción electrón-electrón en las propiedades de baja energía de materiales laminares como cupratos, rutenatos o grafeno. Se calcula la auto-energía por diferentes aproximaciones, para analizar las correcciones que produce en la toplogía de la superficie de Fermi. El método seguido para calcular la auto-energía es independiente del modelo microscópico utilizado para describir el material. Es especialmente útil en materiales anisotrópicos como es el caso de los materiales laminares y que además presentan propiedades no convencionales debido a la interacción electrónica. Como la dispersión electrónica depende del momento y de la energía, el cálculo de la auto-energía es complicado.

En el esquema seguido, las expresiones analíticas para los efectos de la interacción se derivan partiendo de características locales de la superficie de Fermi. Esto nos permite obtener una estimación de la auto-energía de una manera sencilla. Estudiamos la importancia de la correlación electrónica en la interpretación de los resultados obtenidos por espectroscopía de fotoemisión con resolución en ángulos (ARPES).

La importancia de incluir los efectos de correlación en el estudio de los materiales laminares también se demuestra al analizar el diagram de fases del $Ca_{2-x}Sr_xRuO_4$.

Los resultados reflejan que la correlación electrónica resulta ser fundamental para poder relacionar las propiedades medidas con la física micróscopica que subyace en estos sistemas de baja dimensionalidad.

Conclusiones.

Los efectos de la correlación electrónica en las propiedades de baja energía de los materiales laminares resultan ser importantes en la interpretación de los datos experimentales.

Tanto en la red cuadrada como en la hexagonal, incluso en el límite de interacción débil, se encuentran correcciones significativas a la topología de la superficie de Fermi. También se encuentra una renormalización de la velocidad de Fermi de acuerdo con otros cálculos teóricos así como con resultados experimentales. La auto-energía calculada depende del momento.

En el caso de un material multi-orbital como es el $Ca_{2-x}Sr_xRuO_4$, se demuestra que además de la carga y el espín es fundamental tener en cuenta el grado de libertad orbital del electrón. El modelo seguido, teniendo en cuenta la posibilidad de una trasición de Mott selectiva en orbitales (OSMT), reproduce el diagrama de fases obtenido experimentalmente.

Abstract

The electron-electron interaction effects on the low energy properties of layered materials such as copper oxides, ruthenates or graphene are analyzed. By computing the self-energy by different approaches, the corrections induced in the Fermi surface topology have been studyed. The method of calculation of the self energy does not depend on the microscopic model used to describe the material. It is particularly useful in layered materials which show a strong anisotropy and exotic properties induced by many-body interactions. The electron scattering presents momentum and energy dependence, therefore calculating the self-energy is not trivial. In the scheme here presented, analytical expressions of the interactions effects are derived from local features of the Fermi surface. By comparison with experimental results and with band structure calculations, the role of the electron correlation in the interpretation of Angle Resolved Photoemission Experiments (ARPES) is evaluated.

The importance of including correlation effects on the two-dimensional materials is as well demonstrated in the study of the phase diagram of the $Ca_{2-x}Sr_xRuO_4$, when doping is varied. The interpretation of the highly precise experimental data is of fundamental interest in order to gain insight on the microscopic physics from which the unconventional properties arise. The self-energy plays a key role in this complex task.

List of publications

Part of the contents of this work can be found in the following publications.

- *Deformation of anisotropic Fermi surfaces due to electron-electron* interactions.
  R. Roldán, M. P. López-Sancho, F. Guinea and S.-W. Tsai.
  Europhysics Letters **76**, 1165-1171 (2006).

- *Self-energy corrections to anisotropic Fermi surfaces.*
  R. Roldán, M. P. López-Sancho, F. Guinea and S.-W. Tsai.
  Phys. Rev. B **74**, 235109 (2006).

- *Electronic correlation effects in graphene.*
  R. Roldán, M. P. López-Sancho and F. Guinea.
  In preparation.

- *Interplay of metamagnetic and structural transitions in* $Ca_{2-x}Sr_xRuO_4$.
  R. Roldán, A. Rüegg and M. Sigrist.
  In preparation.

Other publications by the author of this thesis are

- *Wide-frequency-range dielectric response of polystyrene latex dispersions.*
  R. Roldán-Toro and J. D. Solier.
  J. Colloid Interface Sci. **274**, 76-88 (2004).

- *Eliashberg theory for anisotropic couplings: a renormalization-group approach.*
  R. Roldán and S.-W. Tsai.
  cond-mat/0702673 (2007). Submitted for publication.

Acknowledgements

I would like to express my gratitude to all the people and friends from the ICMM who have helped me during these four years, especially to my advisor, Pilar.

Contents

Chapter 1

Motivation

The study of Strongly Correlated Electron Systems constitutes nowadays one of the most active fields in Condensed Matter Physics. The common feature of those systems is the dominant role that electron-electron interactions play in their physics. In these materials, the electron motions are strongly modified by the repulsive forces exerted by their neighbors, that they cannot be studied by the independent electron approximation. The strongly correlated materials exhibit exotic transitions at absolute zero temperature, and different kinds of order, conventionally thougth to compete, as antiferromagnetism and superconductivity, coexist. Their properties cannot be described within the Landau theory of the Fermi liquid a paradigm that allowed the enormous development reached by Solid State Physics in the second half of XX century. Transition metal oxides, especially copper oxide hight T_c supercondutors, heavy fermion metals, organic charge transfer compounds, one- and two-dimensional electron gas systems are among the new materials that cannot be understood in the traditional framework. They all present promising technological applications. In spite of the enormous effort done in both experimental and theoretical fields a complete theory to descibe the strongly correlated electron systems is still lacking. On the experimental size, coordinated work has been carried out synthesizing new materials, growing better samples and improving characterization techniques. A huge amount of data are available expecting understanding. They present one of the deepest conceptual challenges in modern physics. Superfluidity, superconductivity at high critical temperature or quantum Hall effect are phenomena without a complete theory, they emerge from the collective behavior of enormous number of interacting particles. The macroscopic properties measured by the experimental techniqes arise from a microscopic word which obeys the quantum mechanical laws. Condensed matter physics had a great developpement in the second half of the twentyeth century based on some fundamental discoveries. To understand the new phenomena shown by the strongly correlated systems, although we need new theories,

we have the background of the powerful knowledge that gave us the Solid State physics, so successful in the study of metals. Two of the most influential conceps which play a main role are **renormalization** and **quasiparticle**:

-Renormalization: the basic assumption of the renormalization is that the physics of a system at a given energy does not depend on all its details. Then, to study the low-energy properties of the system the hole Hamiltonian is not necessary, the *renormalized* Hamiltonian will give the relevant physics. Renormalization is the technique of removing the high degrees of freedom, above an energy cutoff Λ, and adjusting the Hamiltoniam to those modes of the low-energy physics. The new Hamiltonian depends on the energy cutoff Λ, $\mathcal{H}(\Lambda)$ and as Λ decreases the Hamiltonian describes longer time processes ($\tau \approx h/\Lambda$) until a value of Λ is reached where $\mathcal{H}(\Lambda)$ does not change any more. Then, it is said that the system has reached a 'fixed point' and this $\mathcal{H}(\Lambda)$ governs the low-energy, long-time properties of the material. The concept of renormalization is one of the most powerful in Physics and is widely used.

-Quasiparticles: are the elementary excitations of the material. This excitations are like 'single-particles' but with its properties modified by the interactions with the rest of particles. At zero temperature, in the ground state, the lowest-energy state of the system, electrons occuppy the momentum states up to the Fermi momentum, which marks the Fermi surface. To add energy to this state is only possible by adding an electron above the Fermi surface or remove one below it (create a hole). At low temperature the fluid of quasiparticles formed around the Fermi surface (FS) is called a Fermi liquid. Following the renormalization group lenguage quasiparticles are the electrons near the FS with its properties renormalized by interactions. The quasiparticles controll the transport properties of the metal and can be treated as independent particles because the gas of electrons have been renormalized away in the corrections to single-particles properties. These two basic conceps are fundamental for the Landau theory of Fermi Liquid and most of the new theories are based on them.

In this work I study, from a theoretical point of view, the effects of correlation in some fundamental properties of low dimensional systems. Within the Strongly Correlated Electron Systems I will focus on layered materials as transition-metal oxides and graphene. Layered materials present important physics and their unusual properties are derived from the anisotropy and periodicity along the axis perpendicular to the planes. Particularly the structure of the collective excitations is absent in two dimensional and three dimensional systems.

Cuprates, ruthenates, manganites or graphite are layered materials formed by the stacking of planes. They present both scientific fundamental interest and enormous application potential. There is a huge amount of experimental data obtained by different techniques of the properties of these materials. It is re-

markable the role of angle-resolved photoemision spectroscopy (ARPES) which provides information of the single-particle Green's function, directly comparable to the theoretical results calculated from a microscopic Hamiltonian. The recent improvement of energy and momentum resolutions have allowed to extract, under certain assumptions, the real and imaginary part of the self-energy and compare with many-body theory results.

To obtain a direct description of the behavior experimentally measured of the strongly correlated materials is of crucial interest. It is not an easy task since it implies to understand the connections between the response functions and the electronic interactions.

Among the layered materials, transition-metal oxides present a very rich phase diagram. Interactions between electrons drive hase transitions such as metal-insulator transitions, magnetic ordering and superconductivity. Many of these materials are Mott insulators, i.e., although expected to be metallic by band theory considrations, the Coulomb interaction makes them insultaors. Upon doping, by changing some elements of the parent compound, carrieres are introduced in the material and then different ground state of the system controlled by doping, can be obtained. At zero temperature, in teh quantum critical regime, phase transitions may occur due to the quantum fluctuations. quantum critical points appear in teh phase diagram of some transition-metal oxides. By increasing the temperature, thermal fluctuations change the scenario.

The low energy properties and the phase diagram of layere-transition-metal oxides is a central issue in Condensed Matter Physics, since many questions are open. In this work the self-energy corrections, induced by electronic correlation, on the low energy-physics of these materials is analyzed. The self-energy deformation of the 2D Fermi surface topology has been calculated by different approximations and results are discussed and compare with experimental data. Electronci correlation is also considered to analyze the phase diagram of $Ca_{2-x}Sr_xRuO_4$ when x is varied. In the first chapter a summarized introduction of the main concepts and models followed in this work are given. Inthe following three chapters, the main results obtained are expossed. At the end the details of some calculations are explicity written in order to clarify aspects of the followed method.

Chapter 2

Introduction

2.1 Landau Fermi liquid theory.

The Landau's theory of Fermi liquid (FL) [1, 2, 3] describes well the thermodynamic and transport properties of usual metallic systems. The idea is that the low temperature behavior of some quantities like the specific heat, resistivity or optical conductivity can be understood by assuming that the electrons in a metal could be thought of as a gas of non-interacting fermions, i.e., in terms of quantum mechanical particles which do not have any direct interaction but which do obey Fermi statistics. This idea, originally from Sommerfeld, together with the temperature independent paramagnetic susceptibility of non-interacting electrons (calculated by Pauli), were the basis for the Fermi liquid theory. The basic idea underlying it is that of analyticity, i.e., that states with the same symmetry can be adiabatically connected. This means that whether or not we can actually carry out the calculation we know that the eigen-states of the full Hamiltoinan of the same symmetry can be obtained perturbatively from those of a simpler Hamiltoinan. At the same time states of different symmetry cannot be obtained by continuation from the same state (FL theory breaks down in the fluctuation regime of classical phase transitions). This suggest that given a tough problem which is impossible to solve, we may guess a right simple problem. The low energy and long wavelength excitations, as well as the correlation and the response functions of the impossible problem bear a one-to-one correspondence with the simpler problem in their analytic properties. This leaves fixing only numerical values, to be determined by parameters. The proper guess for the simple problem can be provided by experiments. For example, interacting electrons in the metallic range of densities is the problem of kinetic energy of particles with Fermi statistics. As far as we are not close to a phase transition, the qualitative behavior of the non-interacting and interacting system does not change. This theory can be applied even to strongly interacting systems, which low energy excitations

will have strongly renormalized values of their parameters compared to the non-interacting problem, but their qualitative behavior is still the same as that of the simpler problem.

So far we have talked about non-interacting and interacting fermion systems. But what is the difference between a non-interacting Fermi gas (a free electron system) and an interacting Fermi liquid? Let us consider a simple microscopic perspective. For a free electron gas, the momentum states $|\vec{\mathbf{k}}\rangle$ are also eigenstates of the Hamiltonian with eigenvalue $\varepsilon^0_{\vec{\mathbf{k}}} = \hbar^2 k^2/2m$, where $k = |\vec{\mathbf{k}}|$ and m is the (bare) mass of the electrons. In this case, the occupation number $n_{\vec{\mathbf{k}}\sigma} = c^\dagger_{\vec{\mathbf{k}}\sigma} c_{\vec{\mathbf{k}}\sigma}$ are good quantum numbers, where $c^\dagger_{\vec{\mathbf{k}}\sigma}$ ($c_{\vec{\mathbf{k}}\sigma}$) creates (annihilates) an electron with momentum $\vec{\mathbf{k}}$ and spin $\sigma =\uparrow,\downarrow$. The momentum distribution $n_{\vec{\mathbf{k}}} \equiv \langle n_{\vec{\mathbf{k}}\sigma}\rangle$ is given by the Fermi-Dirac function and at $T = 0$ is characterized by a sudden drop from 1 (all states occupied within the Fermi surface) to 0 (no states occupied without the Fermi surface) at $|\vec{\mathbf{k}}| = k_F$ and energy $\varepsilon^0_{\vec{\mathbf{k}}} = \mu$, where μ is the chemical potential (see Fig.2.1). According to this, we can define the *the Fermi surface as the constant energy contour in the reciprocal space that separates the occupied from the unoccupied electronic levels.*

The FL theory makes the assumption that the excitations induced in system by adding a particle in the proximity of the Fermi level, can be described as the particles of the non-interacting system but with the parameters renormalized by the interactions with the rest of the particles.

2.1.1 Green's function formalism.

It is worth defining at this point the single particle Green's function. The Green's-function formalism is a powerful technique to describe the propagation of a single electron in a many-body system. In fact, the time-ordered Green's function $\mathcal{G}(t - t')$ can be interpreted as the probability amplitude that an electron added to the system in a Bloch state with momentum $\vec{\mathbf{k}}$ at a time zero will still be in the same state after a time $|t - t'|$. We shall work in the reciprocal space, in which the Green function can be expressed as $\mathcal{G}(\vec{\mathbf{k}}, \omega) = G^+(\vec{\mathbf{k}}, \omega) + G^-(\vec{\mathbf{k}}, \omega)$, where the +(-) superindex set for the one-electron addition (removal) Green's function. At zero temperature

$$G^\pm(\vec{\mathbf{k}}, \omega) = \sum_m \frac{|\langle \Psi^{N\pm1}_m | c^\pm_{\vec{\mathbf{k}}} | \Psi^N_i \rangle|^2}{\omega - E^{N\pm1}_m + E^N_i \pm i\delta} \tag{2.1}$$

where Ψ^N_i is the N-particle initial state. The summation runs over all possible $(N\pm1)$-particle eigenstates $\Psi^{N\pm1}_m$ with eigenvalues $E^{N\pm1}_m$, and δ is a positive infinitesimal. In the limit $\delta \to 0^+$ one can make use of the identity $(x \pm i\delta)^{-1} =$

$\mathcal{P}(1/x) \mp i\pi\delta(x)$, where $\mathcal{P}$ denotes the principle value, to obtain the *one-particle spectral function* $A(\vec{\mathbf{k}},\omega) = A^{+}(\vec{\mathbf{k}},\omega) + A^{-}(\vec{\mathbf{k}},\omega) = -(1/\pi)\mathrm{Im}\, G(\vec{\mathbf{k}},\omega)$, with:

$$A^{\pm}(\vec{\mathbf{k}},\omega) = \sum_{m} |\langle \Psi_m^{N\pm1} | c_{\vec{\mathbf{k}}}^{\pm} | \Psi_i^{N} \rangle|^2 \delta(\omega - E_m^{N\pm1} + E_i^{N}) \tag{2.2}$$

and $G(\vec{\mathbf{k}},\omega) = G^{+}(\vec{\mathbf{k}},\omega) + [G^{-}(\vec{\mathbf{k}},\omega)]^{*}$, which defines the *retarded* Green's function. The spectral function $A(\vec{\mathbf{k}},\omega)$ gives the distribution of energies ω in the system when a particle with momentum $\vec{\mathbf{k}}$ is added or removed (creating a hole) from it. For the non-interacting system $A_0(\vec{\mathbf{k}},\omega)$ is simply a Dirac-δ function centered at the band energy $\epsilon_{\vec{\mathbf{k}}}^{0} = \varepsilon_{\vec{\mathbf{k}}}^{0} - \mu$, because all momentum states are also energy eigenstates. Therefore the spectral function can be expressed in terms of the single-paticle Green function $G(\vec{\mathbf{k}},\omega)$ which is defined in terms of the correlation function of particle creation and annhihilation operators[4, 5, 6, 7, 8]

$$A_0(\vec{\mathbf{k}},\omega) = -\frac{1}{\pi}\mathrm{Im}G_0(\vec{\mathbf{k}},\omega) = -\frac{1}{\pi}\mathrm{Im}\frac{1}{\omega - \epsilon_{\vec{\mathbf{k}}}^{0} + \imath\delta} = \delta(\omega - \epsilon_{\vec{\mathbf{k}}}^{0}) \tag{2.3}$$

Using this definition, the *Fermi surface will be that defined by the poles of the single-particle Green's function.* In the reciprocal space, the *retarded* Green function can be obtained from the spectral function as

$$G(\vec{\mathbf{k}},\omega) = \int_{-\infty}^{\infty} d\omega' \frac{A(\vec{\mathbf{k}},\omega')}{\omega - \mu - \omega' + \imath\delta\mathrm{sgn}(\omega - \mu)} \tag{2.4}$$

If we now switch on the interactions, the corrections to the Green's functions originating from electron-electron correlations can be conveniently expressed in terms of the single-particle self-energy $\Sigma(\vec{\mathbf{k}},\omega) = \mathrm{Re}\Sigma(\vec{\mathbf{k}},\omega) + \imath\mathrm{Im}\Sigma(\vec{\mathbf{k}},\omega)$. The real and imaginary part of the self-energy carry all the information on the energy renormalization and lifetime, respectively, of an electron with band energy $\epsilon_{\vec{\mathbf{k}}}$ and momentum $\vec{\mathbf{k}}$ propagating in a many-body system. The Green's and spectral function of the interacting system can be expressed in terms of the single-particle self-energy as

$$G(\vec{\mathbf{k}},\omega) = \frac{1}{\omega - \epsilon_{\vec{\mathbf{k}}} - \Sigma(\vec{\mathbf{k}},\omega)} \tag{2.5}$$

$$A(\vec{\mathbf{k}},\omega) = -\frac{1}{\pi}\frac{\mathrm{Im}\Sigma(\vec{\mathbf{k}},\omega)}{\Big(\omega - \epsilon_{\vec{\mathbf{k}}} - \mathrm{Re}\Sigma(\vec{\mathbf{k}},\omega)\Big)^2 + \Big(\mathrm{Im}\Sigma(\vec{\mathbf{k}},\omega)\Big)^2} \tag{2.6}$$

$$\tag{2.7}$$

Notice that because $G(t,t')$ is a linear response function to an external perturbation, the real and imaginary parts of its Fourier transform $G(\vec{\mathbf{k}},\omega)$ have to

satisfy causality and therefore are related by Kramers-Kronig relations. Let us consider the form of the the spectral function when we add a particle to an interacting system of fermions. Due to the interaction between the added particle and those already in the Fermi sea. The added particle will kick particles from below the Fermi surface to above. the possible terms in a perturbative description of this proces are constrained by the conservation laws of charge, spin, momentum and particle number. Those which are allowed by these conservation laws can be expressed as

$$|\Psi^{N+1}_{\vec{\mathbf{k}}\sigma}\rangle = Z^{1/2}_{\vec{\mathbf{k}}} c^{\dagger}_{\vec{\mathbf{k}}\sigma}|\Psi^{N}_{\vec{\mathbf{k}}\sigma}\rangle + \frac{1}{V^{3/2}} \sum_{\vec{\mathbf{k}}_1,\vec{\mathbf{k}}_2,\vec{\mathbf{k}}_3} \sum_{\sigma_1,\sigma_2,\sigma_3} \gamma_{\vec{\mathbf{k}}_1\sigma_1\vec{\mathbf{k}}_2\sigma_2\vec{\mathbf{k}}_3\sigma_3} c^{\dagger}_{\vec{\mathbf{k}}_3\sigma_3} c_{\vec{\mathbf{k}}_2\sigma_2} c^{\dagger}_{\vec{\mathbf{k}}_1\sigma_1} |\Psi^{N}_{\vec{\mathbf{k}}\sigma}\rangle + ... \tag{2.8}$$

where the dots indicates higher-order terms for which two or more particle-hole pairs are created. Therefore the system has been left in an excited state in which additional electron-hole pairs have beeen created. The momentum distribution $n_{\vec{\mathbf{k}}}$ will not look like a step function anymore and will show a finite discontinuity smaller than 1 at the Fermi level $\vec{\mathbf{k}}_F$ and a finite occupation probability for $\vec{\mathbf{k}} > \vec{\mathbf{k}}_F$ even at zero temperature (see Fig.2.1). Therefore, an added particle with fixed total memntum has a wide distribution of energies. However, as long as $Z_{\vec{\mathbf{k}}}$ defined in Eq.(2.8) is finite, $n_{\vec{\mathbf{k}}}$ will show a finite discontinuity at $\vec{\mathbf{k}} = \vec{\mathbf{k}}_F$ there will still be a well-defined Fermi surface. This makes possible the description of the system in terms of *quasiparticles* that can be understood as electrons dressed with a manifold of excited states, which are chareacterized by a pole structure similar to that of the noninteracting system but with a finite lifetime $\tau_{\vec{\mathbf{k}}}$ and renormalized energy $\epsilon_{\vec{\mathbf{k}}}$ and mass m^*. Therefore the *bare-fermion* character of the quasiparticle comes defined by the so-called *quasiparticle weigth* $Z_{\vec{\mathbf{k}}} < 1$ and it is useful to separate the well defined feature from the broad continuum by writing the spectral and Green's functions as the sum of two terms, a coherent pole part and an incoherent somooth part without poles, $G(\vec{\mathbf{k}},\omega) = G_{coh}(\vec{\mathbf{k}},\omega) + G_{incoh}(\vec{\mathbf{k}},\omega)$ and $A(\vec{\mathbf{k}},\omega) = A_{coh}(\vec{\mathbf{k}},\omega) + A_{incoh}(\vec{\mathbf{k}},\omega)$ with

$$G_{coh}(\vec{\mathbf{k}},\omega) = \frac{Z_{\vec{\mathbf{k}}}}{\omega - \epsilon_{\vec{\mathbf{k}}} + \imath/\tau_{\vec{\mathbf{k}}}} \tag{2.9}$$

This term gives, for large lifetimes, a Lorentzian peak in the spectral density at the quasiparticle energy $\epsilon_{\vec{\mathbf{k}}}$. The incoherent Green's function is smooth and hence for large $\tau_{\vec{\mathbf{k}}}$ corresponds to the smooth background in the spectral density. Necessary conditions for the Fermi liquid theory to apply are that $\Sigma(\vec{\mathbf{k}},\omega)$ have an analytic expansion about $\omega = 0$ and $\vec{\mathbf{k}} = \vec{\mathbf{k}}_F$ and that its real part is much larger than its imaginary part. One can make the indentifications[10] $\epsilon_{\vec{\mathbf{k}}} = Z_{\vec{\mathbf{k}}}(\epsilon^0_{\vec{\mathbf{k}}} + \mathrm{Re}\Sigma(\vec{\mathbf{k}},\omega))$, $\tau^{-1}_{\vec{\mathbf{k}}} = Z_{\vec{\mathbf{k}}}|\mathrm{Im}\Sigma(\vec{\mathbf{k}},\omega)|$ and

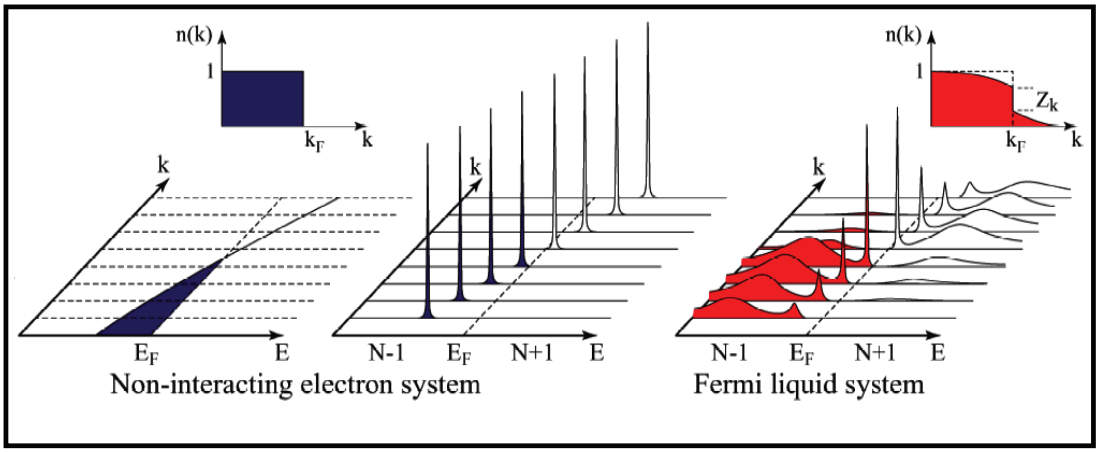

Figure 2.1: On the left hand side it is represented the momentum-resolved one-electron removal and addition spectra for an non-interacting electron system with a single energy band dispersing across E_F. On the right hand side it is shown the same spectra for an interacting FL system. For both cases, the corresponding ground-state zero temperature momentum distribution function $n(\vec{\mathbf{k}})$ is also shown. Figure adapted from Ref.[9].

$$Z_{\vec{\mathbf{k}}} = \left(1 - \frac{\partial \mathrm{Re}\Sigma(\vec{\mathbf{k}},\omega)}{\partial\omega}\right)^{-1}_{\omega\to 0,\vec{\mathbf{k}}=\vec{\mathbf{k}}_F} \tag{2.10}$$

The effect of the self-energy corrections in the interacting system becomes evident if we look at the single-particle spectral function for the two cases (Fig.[]). Due to the finite value of $\mathrm{Im}\Sigma(\vec{\mathbf{k}},\omega)$, the quasiparticle peak has a finite life-time in the interacting case compare to the Dirac-δ shape of the bare system. In addition, the peak position is shifted with respect to the bare-band energy $\epsilon^0_{\vec{\mathbf{k}}}$ due to the finite contribution of $\mathrm{Re}\Sigma(\vec{\mathbf{k}},\omega)$: the total dispersion (or bandwidth) will be smaller for the interacting system due to the enhancement of the band mass due to interactions ($m^* > m$). On the other hand, $Z_{\vec{\mathbf{k}}}$ can be understood as the overlap of the ground state wavefunction of a system of interacting $N\pm 1$ fermions of total momentum $\vec{\mathbf{k}}$ with the wavefunction of N interacting particles and a bare particle of momentum $\vec{\mathbf{k}}$, $Z^{1/2}_{\vec{\mathbf{k}}} = \langle \Psi^{N+1}_{\vec{\mathbf{k}}} | c^\dagger_{\vec{\mathbf{k}}} | \Psi^N \rangle$. As far as we have a finite $Z_{\vec{\mathbf{k}}}$, the FL theory asserts that for small frequencies ω and for wave vectors $\vec{\mathbf{k}}$ close to the Fermi level $\vec{\mathbf{k}}_F$, the physical properties of the interacting system can be calculated from quasiparticles which carry the same quantum numbers as the particles, i.e., charge, spin and momentum but with renormalized parameters. The distribution function of the quasiparticles close to $\vec{\mathbf{k}}_F$ and for T small compared to the Fermi energy, is assumed to be the Fermi-Dirac distribution in terms of th renormalized

quasiparticle energies. This distribution is quiet different to the bare particle one (Fig.2.1). One of the main results of the FL theory is that close to the Fermi energy at zero temperature, the inverse lifetime $1/\tau_{\vec{\mathbf{k}}}$ of the coherent quasiparticle peak is proportional to $\epsilon^2_{\vec{\mathbf{k}}}$ so that near the Fermi energy the lifetime is long and quasiparticles are well-defined.

Another important result derived from the microscopic theory is the so-called *Luttinger theorem*, which states that the volume enclosed by the Fermi surface does not change due to interactions[7]: under the assumption of FL theory, the number of poles in the interacting Green's function below the chemical potiential is the same as that for the non-interacting Green's function. Notice that the latter is just the number of particles in the system.

2.2 Measurement of Fermi surfaces by ARPES.

Once we understand the theoretical notion of Fermi surface, let us describe the most widely used technique to measure it: the Angle Resolved Photoemission Spectroscopy. ARPES is the most direct method of studying the electronic structure of layared materials and it provides information on the single-particle Green's function which, as we have already seen, can be calculated theoretically starting from a microscopic Hamiltonian. The discovery of high-T_c cuprates superconductors[11] and the convenience of ARPES to study the electronic structure of these systems has made possible a significant improvement in instrumental resolution and detection efficiency over the last years. In these experiments, based on the photoelectric effect, a monochromatized radiation is incident on a properly aligned single crystal sample. The electrons that are emitted by the photoelectric effect can be collected with an electron energy analyzer. This analyzer can rotate in angles so that it measures the kinetic energy of the photoelectrons for a given emission angle. As a result, one obtains a very accurate information about the component of the momentum of the electrons parallel to the surface of the sample, as well as the binding energy of the electrons in the crystal [9].

The total photoemission intensity measured as a function of the kinetic energy at a momentum $\vec{\mathbf{k}}$ is proportional to the single particle spectral function $I(\vec{\mathbf{k}},\omega) \propto f(\omega)A(\vec{\mathbf{k}},\omega)$ where $\vec{\mathbf{k}} = \vec{\mathbf{k}}_{\parallel}$ is the in-plane electron momentum, ω is the electron energy with respect to the Fermi level an $f(\omega) = 1/(1+e^{\omega/k_BT})$ is the Fermi function which accounts for the fact that direct photoemission probes only the occupied electronic states. Therefore ARPES provides information about the spectral function $A(\vec{\mathbf{k}},\omega)$ which, in turn, depends on the single-particle self-energy $\Sigma(\vec{\mathbf{k}},\omega)$ as we have seen in Eq.(2.7).

Finally, it should be pointed out that the first technique developed to measure

the Fermi surface of a metal was based on the so called de Haas-van Alphen effect. At low temperature an high magnetic fields H, the magnetization of a crystal oscillates as the magnetic field increases. The oscillations are due to the quantization of electron energy levels in a magnetic field [12]. The orbits are quantized and there is a simple relation between the change in $1/H$ through a single period oscillation and the area of the Fermi surface in a plane normal to the magnetic field [13]. Therefore information can be extracted to reconstruct the actual shape of the Fermi surface.

2.3 The Hubbard model.

This model has been widely used in the last decades since Anderson proposed that it would capture the essential physics of the cuprate superconductors [14]. The Hubbard model [15] contains a single kinetic-energy term proportional to the nearest neighbor hopping integral t, in addition to the Hubard U term that favors electron localization and results in *frustration* of the kinetic energy:

$$\mathcal{H}_U = \sum_{\sigma;i,j} t_{ij} c^{\dagger}_{\sigma,i} c_{\sigma,j} + U \sum_{i} n_{i\uparrow} n_{i\downarrow} \tag{2.11}$$

where $c_{\sigma,i}(c^{\dagger}_{\sigma,i})$ are destruction (creation) operators for electrons of spin σ on site i, $n_{i,\sigma} = c^{\dagger}_{\sigma,i} c_{\sigma,i}$ is the number operator, U is the on-site repulsion, and $t_{ij} = t$ is the nearest neighbor hopping amplitude. The local nature of the real space interaction results in a momentum independent coupling constant in the reciprocal space and the Hamiltonian can be written as

$$\mathcal{H}_U = \sum_{\vec{\mathbf{k}}\sigma} \varepsilon(\vec{\mathbf{k}}) c^{\dagger}_{\vec{\mathbf{k}}\sigma} c_{\vec{\mathbf{k}}\sigma} + \frac{U}{2\mathcal{V}} \sum_{\vec{\mathbf{k}},\vec{\mathbf{k}}',\vec{\mathbf{q}}} \sum_{\sigma,\sigma'} c^{\dagger}_{\vec{\mathbf{k}}+\vec{\mathbf{q}},\sigma} c_{\vec{\mathbf{k}}'-\vec{\mathbf{q}},\sigma'} c_{\vec{\mathbf{k}}',\sigma'} c_{\vec{\mathbf{k}},\sigma} \tag{2.12}$$

where $\mathcal{V}$ is the volume of the system. The non interacting dispersion relation is defined by:

$$\varepsilon(\vec{\mathbf{k}}) = 2t \left[\cos(k_x a) + \cos(k_y a)\right] \tag{2.13}$$

where a is the lattice constant. In the strong coupling limit $U \gg t$ at half filling, the antiferromagnetic state results from the fact that, when nearest-neighbor spins are antiparallel to each other, the electrons gain kinetic energy by undergoing virtual hopping to neighboring sites (because of the Pauli principle, hopping is forbidden for parallel spins).

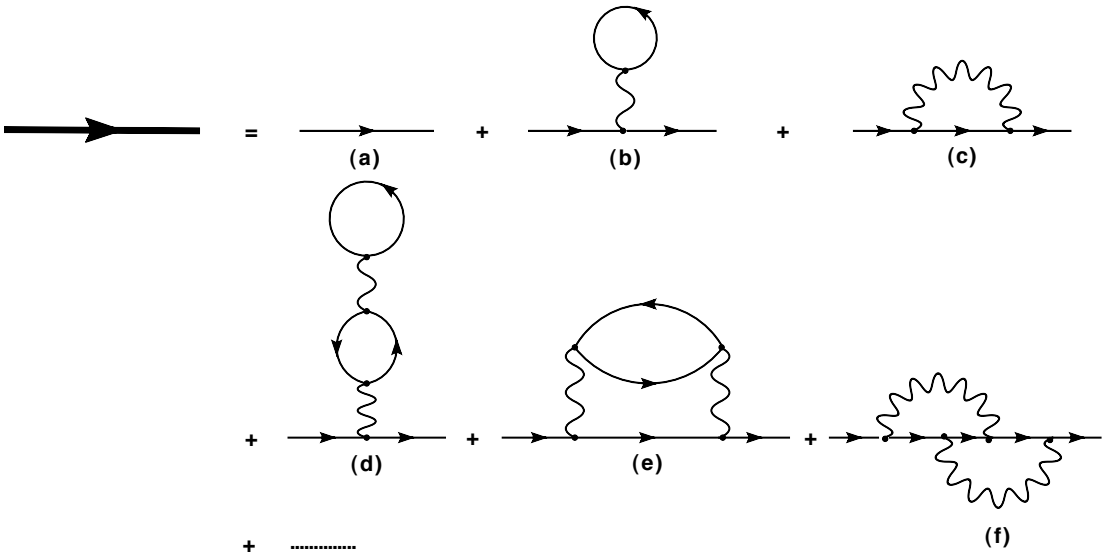

Figure 2.2: Perturbative expansion of the single particle Green's function.

2.4 Perturbation theory

Perturbation theory is a method for the systematic estimation of the effective interaction, certainly justified in the weak coupling regime. In the context of the Hubbard model, the expansion parameter is U/W, where U is the on-site Coulomb repulsion and W is the band width. The principle of the adiabatic continuity in the FL theory requires the regularity of the expansion. In the periodic system, the perturbation theory method is expected to be useful to understand the qualitative natures in the weak coupling region $U < W$, as long as no long-range order occur.

As we pointed out above, the dressed Fermi surface depends on the self-energy correction, which is given by the irreducible part of the corrections to the two-point function and it is related to the full propagator by

$$G^{-1} = \left(G^{(0)}\right)^{-1} - \Sigma \tag{2.14}$$

where Σ is the self-energy. This is the well know Dyson equation. Eq.(2.14) gives the series expansion for the propagator shown in Fig.(2.2), where the first contributions in perturbation theory are drawn. Here the wiggly lines represent the interaction potential $V(\vec{\mathbf{k}}, \omega)$, while the weak (thick) directed line represent the free (interacting) one-particle propagator. In this thesis, we will focus especially on the case of a constant coupling U acting between particles with opposite spins, although some momentum dependent interaction corrections will be studied as well (see Chapter4). The restriction to a momentum-independent coupling corresponds to a local interaction in real space, which is the case for a short-

range interaction. In the first line in the left hand side we represent the dressed single-particle Green's function G, while in the right hand side of the identity we represent the bare one-particle propagator $G^{(0)}$ (diagram (a)) plus the one-loop diagrams. The diagram (b), Hartree term, contributes to the self-energy with a constant term. This is due to the momentum conservation, which makes the momentum carried by the interaction to be $\vec{\mathbf{q}} = 0$. This loop then is the integral over momenta and frequencies of the bare Green's function, giving the density of particles ($\Sigma^{(1)}_{(b)} = Un/2$), contribution which can be reabsorbed in the chemical potential by a shift $\delta\mu_{1b} = Un/2$ in order to keep the density fixed. However this diagram does not induce changes in the shape of the FS because it cannot give rise to a correction depending on the external frequency or momentum. The second one-loop contribution, diagram (c) in figure (2.2), is the 'exchange' term. The contribution of this term is zero for a local interaction U, but it gives a momentum dependent contribution in the case of a non-local interaction $V(\vec{\mathbf{k}}, \omega)$. Looking at the two-loops diagrams, second line in Fig.(2.2), we see that some of them, like diagram (f), are a real constant which is completely cancelled by a new shift of the chemical potential $\delta\mu_{2f}$. Then, for a local interaction U, we must calculate the self-energy contribution given by the two-loop diagram of the form (d), since it is the first which gives a non-trivial contribution to this case and generates a Fermi surface deformation.

It should be noticed that ordinary perturbation theory is helpless when confronted with the big interactions in a many-body system. In typical cases nearly all terms in the propagator and vacuum amplitude perturbation expansions are diergent. To get any sensible results, one is therefore forced to use a method which goes beyond ordinary perturbation theory.

2.5 Mean field approximation.

Mean-field is often used to study phase transitions and thus changes of symmetry. This will be the technique used in Chapter 5 when studying the phase diagram of $Ca_{2-x}Sr_xRuO_4$. Although it implies a drastic simplification of the problem, mean field theory is well suited to detect phases with spontaneously broken symmetry where operators $\mathcal{O}_\alpha$, whose expectation value $\langle\mathcal{O}_\alpha\rangle$ is identically zero for finite systems due to symmetry, acquire a finite expectation value in the thermodynamic limit. The symmetry group of the sysem is spontaneously reduced to a subgroup and the different subgroups characterize the various possible phases. The basic idea of the mean-field theory is the assumption that the ground state can be reasonably well described by a Slater determinant, i.e., that the ground state of the interacting system can be apprximated by the ground state, $|\Psi\rangle$, of a non-

interacting Hamiltonian. Let us describe our interacting particles system by the Hamiltonian,

$$\mathcal{H} = \mathcal{H}_0 + \mathcal{H}_{int} \tag{2.15}$$

where $\mathcal{H}_0 = \sum_\alpha \zeta_\alpha c_\alpha^\dagger c_\alpha$ and the quartic term reads,

$$\mathcal{H}_{int} = \frac{1}{2} \sum_{\alpha\alpha'\beta\beta'} V_{\alpha\beta,\alpha'\beta'} c_\alpha^\dagger c_\beta^\dagger c_\beta^\dagger c_{\alpha'} \tag{2.16}$$

In the ground state $|\Psi\rangle$ the expectation value of an operator can be evaluated by applying the Wick theorem[8], which states that if the particles can be treated as being independent (mean field assumption) then the four-term average $\langle c_\alpha^\dagger c_\beta^\dagger c_\beta^\dagger c_{\alpha'}\rangle$ factorizes into two-term averages,

$$\langle c_\alpha^\dagger c_\beta^\dagger c_\beta^\dagger c_{\alpha'}\rangle = \langle c_\alpha^\dagger c_{\alpha'}\rangle\langle c_\beta^\dagger c_{\beta'}\rangle \pm \langle c_\alpha^\dagger c_{\beta'}\rangle\langle c_\beta^\dagger c_{\alpha'}\rangle \tag{2.17}$$

where the +(-) sign is for bosons (fermions). The first term on the right hand side of Eq.(2.17) is the Hartree term, while the second term is the exchange term. The mean field approximation consist on substitute the quartic term in the interacting Hamiltonian Eq.(2.16) by the decoupling

$$\begin{aligned} c_\alpha^\dagger c_\beta^\dagger c_\beta^\dagger c_{\alpha'} \simeq\ & c_\alpha^\dagger c_{\alpha'}\langle c_\beta^\dagger c_{\beta'}\rangle + \langle c_\alpha^\dagger c_{\alpha'}\rangle c_\beta^\dagger c_{\beta'} \\ & \pm c_\alpha^\dagger c_{\beta'}\langle c_\beta^\dagger c_{\alpha'}\rangle \pm \langle c_\alpha^\dagger c_{\beta'}\rangle c_\beta^\dagger c_{\alpha'} \\ & -\langle c_\alpha^\dagger c_{\alpha'}\rangle\langle c_\beta^\dagger c_{\beta'}\rangle \mp \langle c_\alpha^\dagger c_{\beta'}\rangle\langle c_\beta^\dagger c_{\alpha'}\rangle \end{aligned} \tag{2.18}$$

In the previous approximation we have assumed that the density operators $c_\alpha^\dagger c_{\alpha'}$ deviate only little from their average value $\langle c_\alpha^\dagger c_{\alpha'}\rangle$, so we neglect products of the form $(c_\alpha^\dagger c_{\alpha'} - \langle c_\alpha^\dagger c_{\alpha'}\rangle)(c_\beta^\dagger c_{\beta'} - \langle c_\beta^\dagger c_{\beta'}\rangle)$.

Chapter 3

Self-energy corrections the Fermi surface topology. Application to the square lattice.

3.1 Introduction

Anisotropic materials present different physics at different energy scales, and their behavior or response to external probes is difficult to interpret. A big amount of experimental works have made possible to study the puzzling electronic properties of many anisotropic materials which, in general, present potential technological applications. More theoretical effort is needed in order to understand the detailed experimental data which reveal an unconventional behavior. In conventional metals, the excitations that govern their low-temperature physics present well defined momenta lying at the three-dimensional Fermi surfaces. In the anisotropic materials, as layered transition metal oxides, unusual electronic properties appear and, under certain conditions, changes of the effective dimensionality occur. The electronic interaction effects are enhanced as the dimensionality decreases and can change the fundamental properties of the material[16]. Therefore, due to both the anisotropy and the periodicity along the axis perpendicular to the planes, specific collective excitations appear absent in two-dimensional (2D) and three-dimensional (3D) electron gases[17, 18]. In Fig.3.1 a schematicc representation of the perovskite structure, common to cuprates and ruthenates, is depicted.

The high-temperature cuprate superconductors are among the most studied layered transition metals oxides, treated as 2D systems in many approaches, due to its strong anisotropy. In the hole doped cuprates the FS topology changes with doping from hole-like to electron-like [19, 20]. Recently a change in the sign of the Hall coefficient has been reported for heavily overdoped $LaSrCuO_4$ [21]. The evolution of the FS in electron-doped copper oxide superconductors with

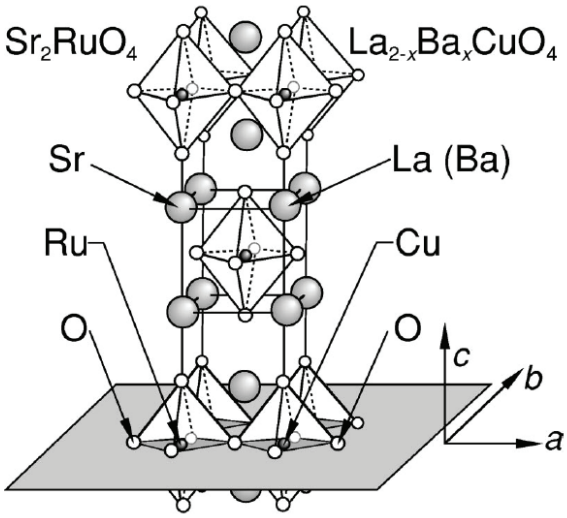

Figure 3.1: Layered perovskite structure common to cuprate superconductors and ruthenates.

doping has been reported by ARPES experiments to change from electron-pocket centered at the $(\pi, 0)$ point of the Brillouin zone at low doping to a hole-like FS centered at (π, π) at higher doping[22].

Other transition metal oxides as cobaltates or ruthenates are multiorbital systems and their FS present a complex topology with different sheets derived from the different bands at the Fermi energy. A correlated 2D material particularly interesting is the Sr_2RuO_4, a ruthenate considered a model Fermi liquid system with important electronic correlations which have to be taken into account when interpreting photemission spectra[23] to obtain a clear picture of the electronic properties, especially in the vicinity of the Fermi energy. In Sr_2RuO_4 the FS separates into three sheets α, β, and γ, coming from the d_{xz}, d_{yz} and d_{xy} orbitals. In the study of the electron-electron interactions in anisotropic metallic systems an open question is the deformation of the Fermi surface induced by these interactions. The Fermi surface is one of the key features needed to understand the physical properties of a material and its shape provides important information. Recent improvements in experimental resolution have led to high precision measurements of the Fermi surface, and also to the determination of the many-body effects in the spectral function, as reported by angle resolved photoemission spectroscopy (ARPES) experiments [9]. However the interpretation of the data obtained by different experimental techniques in anisotropic strongly correlated systems remains a complex task[24].

The Fermi surface depends on the self-energy corrections to the quasiparticle energies, which, in turn, depend on the shape of the Fermi surface. Hence, there is

an interplay between the self-energy corrections and the Fermi surface topology. For weak local interactions, the leading corrections to the Fermi surface (FS) arise from second order diagrams. The self energy, within this approximation, can show a significant momentum dependence when the initial FS is anisotropic and lies near hot spots, where the quasiparticles are strongly scattered[25]. This simultaneous calculation of the FS and the second order self-energy corrections is a formidable task. However, the knowledge of the exact shape of the FS of a material is very important since it may affect the transport properties as well as the collective behavior, and have a valuable information from the point of view of theory in orther to find the appropriate model to study the system. Many approaches have been used to study this problem like mean-field[26], pertubation theory[27], bosonization methods[28, 29], or perturbative Renormalization Group calculations[30, 31, 32], and the cellular dynamical mean-field theory (CDMFT), an extension of Dynamical Mean Field Theory[33], and many others. In spite of the great theoretical effort done in the last years, there is a need to develop alternative new methods in order to understand the origin of the electronic properties in materials with strong correlations.

In this chapter, we calculate perturbative corrections and use Renormalization Group arguments[34, 35] in order to study analytically the qualitative corrections to the shape of the FS induced by the electron-electron interaction. This method allows us to classify the different features of the FS from the dependence of the self-energy corrections on the value of the high energy cutoff, Λ, defined at the beginning of the Renormalization process. As it will be shown later, one can also analyze the effects of variations in the Fermi velocity and the curvature of the non interacting FS on the self-energy corrections. The calculations do not depend on the microscopic model which gives rise to a particular Fermi surface, so that it can be useful in different situations. By concretion we will consider the $t-t'$ Hubbard model to study two dimensional Fermi surfaces of cuprates and an extension of it to study the case of Sr_2RuO_4. The chapter is organized as follows. We define the model in Section3.2 and describe the way the corrections induced by different features of the FS depend on the high energy cutoff Λ. In Section3.3 we present a detailed calculation of the changes expected for a regular FS, as well as for a FS showing singular points like Van Hove singularities, nesting or inflexion points. We compare with results from ARPES experiments on anisotropic materials. In the last section we highlight the most relevant aspects of our calculation, and compare them with results obtained using alternative schemes.

3.2 The method

The method of calculation of the self-energy corrections does not depend on the microscopic model used to obtain the electronic structure and the FS. In our scheme simple analytical expressions of the effects induced by the interactions are deduced from local features of the Fermi surface, and we are able to treat, on the same footing, the regular and singular regions of the FS. Therefore the method is particularly useful in correlated anisotropic materials which present exotic properties and deviate from band structure calculations. The importance of considering correlation effects when interpreting experimental data is already known and recently a great effort has been made in order to evaluate the self-energy from ARPES spectra[36]. The evaluation of many body effects in these complex materials is far from trivial since the electron scattering presents a dependence on momentum and energy. We limit the study to the weak coupling regime, considering weak local interactions, consistent with the Hubbard model.

3.2.1 The model.

We consider the $t-t'$ Hubbard model which is the simplest theoretical model which allows us to study different correlated materials and describes the shape of the FS observed by ARPES in different materials as cuprates (see ref.[9] and references therein). Depending on the ratio t'/t and on the band-filling, different phases and stabilities appear, as found in early mean-field and Quantum Monte Carlo (QMC) studies of the model[37]. By changing the parameters a rich phase diagram, including antiferromagnetic, ferromagnetic and superconducting phases, has been found for the 2D $t-t'$ Hubbard model which describes many physical features of copper oxides and of Sr_2RuO_4[38]. For the cuprates, the most studied model is the Hubbard model on a square lattice and considering an effective single band. The hamiltonian of the $t-t'$ Hubbard model is:

$$\mathcal{H} = \sum_{\sigma;i,j} t_{ij} c^{\dagger}_{\sigma,i} c_{\sigma,j} + U \sum_{i} n_{i\uparrow} n_{i\downarrow} \tag{3.1}$$

where $c_{\sigma,i}(c^{\dagger}_{\sigma,i})$ are destruction (creation) operators for electrons of spin σ on site i, $n_{i,\sigma} = c^{\dagger}_{\sigma,i} c_{\sigma,i}$ is the number operator, U is the on-site repulsion, and $t_{ij} = t$ are the nearest and $t_{ij} = t'$ the next-nearest neighbors hopping amplitudes, respectively. The Fermi surfaces of the non interacting systems are defined by:

$$\epsilon_{\mathrm{F}} = \varepsilon(\vec{\mathbf{k}}) = 2t\left[\cos(k_x a) + \cos(k_y a)\right] + 4t' \cos(k_x a)\cos(k_y a) \tag{3.2}$$

where a is the lattice constant.

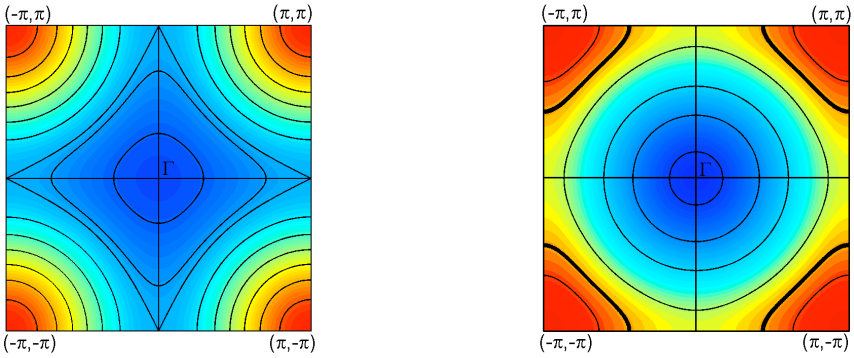

(a) Constant energy contours for $t' = -0.3t$ (b) Constant energy contours for $t' = 0.3t$

Figure 3.2: Qualitative picture of the evolution of the FS with filling from almost isotropic to convex, going through a FS exhibiting inflexion points, and one with van Hove singularities (panel (a), $t' = -0.3t$). A region with almost perfect nesting ishown in panel (b) ($t' = 0.3t$).

Assuming that $t < 0, t' > 0$ and $|2t'| < |t|$, the Fermi surface is convex for $-2t+4t' \leq \epsilon_{\rm F} \leq \epsilon_0 = -8t' + 16t'^3/t^2$. For $-8t' + 16t'^3/t^2 \leq \epsilon_{\rm F} \leq -4t'$ the Fermi surface shows eight inflection points, which begin at $k_x = k_y = k_0 = a^{-1}\cos^{-1}(-2t'/t)$ and move symmetrically around the $(\pm 1, \pm 1)$ directions, towards the center of the edges of the square Brillouin zone, $(0, \pm\pi), (\pm\pi, 0)$. For $\epsilon_{\rm F} = 4t'$ the Fermi surface passes through the saddle points (Van Hove singularities) located at these special points of the Brillouin zone. For $4t' < \epsilon_{\rm F} \leq -4t$, the Fermi surface is convex and hole like, centered at the corners of the Brillouin Zone, $(\pm\pi, \pm\pi)$. In Fig.[3.2] the variation of the FS shapes with doping is qualitatively shown. When only nearest-neighbor hopping is considered, $t' = 0$, the model has particle hole symmetry, and the Fermi surface shows perfect nesting for $\epsilon_{\rm F} = 0$. FS shapes similar to these shown in Fig.[3.2] have been experimentally observed by ARPES on different cuprate samples, at different doping levels.

3.2.2 Self-energy analysis.

We will analyze the interplay between the electron-electron interactions and the FS topology in the weak-coupling regime. The corrections to the non-interacting Fermi surface are given by the real part of the self-energy. For each filling n, a Fermi surface is defined. The electron-electron interaction leads to a self-energy

$$\Sigma(\vec{\mathbf{k}}, \omega) = {\rm Re}\Sigma(\vec{\mathbf{k}}, \omega) + i{\rm Im}\Sigma(\vec{\mathbf{k}}, \omega) \tag{3.3}$$

which modifies the bare one-particle propagator $G_0(\vec{\mathbf{k}}, \omega)^{-1} = \omega - \epsilon_{\vec{\mathbf{k}}} + i\delta\,{\rm sgn}\,\epsilon_{\vec{\mathbf{k}}}$ (where $\delta \to 0^+$) to

$$G(\tilde{\mathbf{k}},\omega) = \frac{1}{\omega - [\varepsilon(\vec{\mathbf{k}}) - \epsilon_{\rm F}] - \Sigma(\vec{\mathbf{k}},\omega)} \tag{3.4}$$

and the FS of the interacting system is given by the solution of the equation

$$\epsilon_{\rm F} - \varepsilon(\vec{\mathbf{k}}) - {\rm Re}\Sigma(\vec{\mathbf{k}},\omega=0) = 0 \tag{3.5}$$

where ${\rm Re}\Sigma(\vec{\mathbf{k}},\omega)$ is the real part of the self-energy. The diagrams that renormalize the one-particle Green function up to second order in perturbation theory are depicted in Figure[3.3]. The Hartree diagram, shown at the left of the figure, gives a contribution which is independent of momentum and energy, hence it cannot deform the FS. The two-loop diagram (right of Fig.[3.3]), modifies the FS through its $\vec{\mathbf{k}}$ dependence and, in addition, it changes the quasiparticle-weight through its ω dependence.

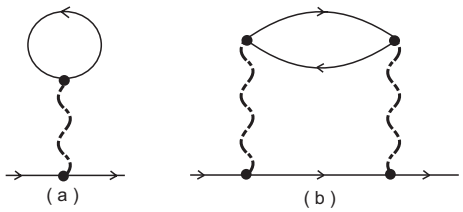

Figure 3.3: Low order self-energy diagrams. (a) Hartree diagram. (b) Two loop correction.

As explained above there are many possible shapes of the FS which fit the experimental results from copper-oxide or ruthenate samples. The conventional perturbation theory fails on describing FS for which logarithmic divergences in the density of states (DOS) appear at certain values of the parameters of Eq.(3.1). Then we proceed to calculate the self-energy by adopting a Renormalization Group strategy[34, 35]. It is assumed that the effect of the high energy electron-hole pairs on the quasiparticles near the Fermi surface have been integrated out, leading to a renormalization of the parameters t, t' and U of the hamiltonian. The possibility that other couplings are generated in the system is not allowed. Thus, the hamiltonian, Eq.(3.1), describes low temperature processes below a high energy cutoff, $\Lambda \ll t, t'$. For consistency, we consider the Hubbard interaction $U \lesssim \Lambda$, as well below the energy cutoff. Therefore the corrections to the quasiparticle energies are determined as a function of Λ, which defines an energy scale about the Fermi line which will contain the modes we are interested on (low energy excitations with $|\epsilon_{\vec{\mathbf{k}}}| < \Lambda$), separated from the high energy excitations (with $|\epsilon_{\vec{\mathbf{k}}}| > \Lambda$) which will be integrated out. We have to notice that we are restricting ourselves to a momentum-independent coupling U which corresponds to a local interaction in the real space. During the process we assume that the Fermi

surface of the interacting system exists, and that this FS, dressed by the corrections due to the interactions, has the same topology as that of the non-interacting system.

The two-loop self-energy shown in Fig.[3.3](b) can be computed from

$$i\Sigma_2(\vec{\mathbf{k}},\omega) = \frac{1}{(2\pi)^3}\int d\omega' \int d^2q \mathrm{G}_0(\tilde{\mathbf{k}}-\tilde{\mathbf{q}},\omega-\omega')\Pi(\tilde{\mathbf{q}},\omega') \tag{3.6}$$

where the particle-hole polarizability, in terms of the one-particle propagator, reads

$$i\Pi(\vec{\mathbf{q}},\omega) = \frac{U^2}{(2\pi)^3}\int d\omega' \int d^2k\, \Theta(\Lambda-|\epsilon_{\vec{\mathbf{k}}}|)\Theta(\Lambda-|\epsilon_{\vec{\mathbf{k}}+\vec{\mathbf{q}}}|)G_0(\vec{\mathbf{k}},\omega')G_0(\vec{\mathbf{k}}+\vec{\mathbf{q}},\omega+\omega') \tag{3.7}$$

The cutoff in energies Λ is used to implement the RG scheme[34]: the virtual states in the loop of the diagram shown in Fig.[3.3](b) have to be kept in the energy range determined by the cutoff.

3.3 Results

After we compute the self-energy as explained above, we will analyze the deformation induced in the Fermi surface shape. We are interested in anisotropic two-dimensional FS similar to those measured for the cuprates which present regions with different scattering rates. By clarity, we consider first Fermi surfaces with hot spots, which are regions where the scattering of the quasiparticles is strongly enhanced. At these points, the scattering could be singular giving divergences of the susceptibility. Separately we address the deformations of regular FS, curved surfaces which do not have singularities. These surfaces present a scattering rate relatively weak. We will show that once the Fermi velocity and curvature of the non-interacting FS are known, we can evaluate the corrections to the FS shape. Even considering a weak local interaction, without momentum dependence, the effects are strongly dependent of the location at the FS.

3.3.1 Self-energy corrections to the Fermi surface near hot spots.

In anisotropic materials, the FS can present regions or special points which are called hot spots where the quasiparticles become strongly scattered and their behavior deviates from the conventional Landau Fermi liquid. The FS of layered

transition oxides, as have been shown above, changes with doping adopting different shapes which lie close to Van Hove singularities, or present nested flat regions or inflexion points combined with regular sectors.

The effects of the Hubbard interaction have been studied when the Fermi surface presents hot spots both, near the perfect nesting[39, 40, 41] or near a Van Hove singularity[42, 43, 44, 45, 46, 47, 48, 49]. The curvature of the FS has important implications in the properties of the system and the inflection points, which separate regions where the curvature has opposite signs, may induce anomalous effects[50, 51]. The crucial role that the FS geometry plays on the unusual physics of 2D systems, makes it desirable a deeper insight in the interplay between it and measurable parameters. The functional dependence of the self-energy on the cutoff is different in the vicinity of the hot spots than in regular zones of the FS. Near the hot spots to be considered here, the dispersion relation satisfies, near the Fermi level:

$$\epsilon_{\vec{\mathbf{k}}} \approx \begin{cases} \pm\frac{k_x^2}{m_x} \mp \frac{k_y^2}{m_y} & \text{Van Hove} \\ v_F k_\perp & \text{nesting} \end{cases} \tag{3.8}$$

where $\epsilon_{\vec{\mathbf{k}}} = \varepsilon(\vec{\mathbf{k}}) - \epsilon_{\mathrm{F}}$, $k_\perp$ is the momentum perpendicular to the FS relative to k_F, $k_\perp = (\vec{\mathbf{k}} - \vec{\mathbf{k}}_F)_\perp$, v_F is the Fermi velocity at any particular point and $m_x \sim m_y$.

Unlike the usual quadratic dependence expected in a Fermi liquid, the frequency dependence of the imaginary part of the self-energy in a nested region of the Fermi surface, or at Van Hove singularities is known to be linear:

$$\mathrm{Im}\Sigma_2(\vec{\mathbf{k}}, \epsilon_{\vec{\mathbf{k}}}) \propto |\epsilon_{\vec{\mathbf{k}}}| \tag{3.9}$$

At the FS parts away from the hot spots, the leading contribution to the two loop self-energy, when the Fermi surface is near a Van Hove singularity, comes from diagrams where the polarizability bubble, $\Pi(\vec{\mathbf{q}}, \omega)$ expressed in Eq.(3.7), involves transitions near the saddle point[52].

Only particles in the vicinity of hot spots on the FS are strongly scattered and present an anomalously large life-time, while away the hot spots the single particle lifetime follows the Landau's Fermi liquid theory energy dependency. At some values of the band filling the FS is near a nesting situation, as shown in Fig.[3.2], then the polarizability at low momenta is similar to that of a one dimensional Fermi liquid, due to the flat FS regions. The susceptibilities can be written as:

$$\Pi(\vec{\mathbf{q}}, \omega) \sim \begin{cases} W^{-1}\tilde{\Pi}_{\mathrm{vH}}\left(\frac{\omega}{m^*|\vec{\mathbf{q}}|^2}\right) & \text{Van Hove} \\ W^{-1}\tilde{\Pi}_{\mathrm{1D}}\left(\frac{\omega}{v_{\mathrm{F}}|\vec{\mathbf{q}}|}\right) & \text{nesting} \end{cases} \tag{3.10}$$

where m^* is an average of the second derivative of the bands at the saddle point. Note that, in both cases, the density of states is proportional to the inverse bare bandwidth $W^{-1} \sim t^{-1}, t'^{-1}$.

The imaginary part of the second order self-energy near the regular regions of the Fermi surface can be written as[52]:

$$\mathrm{Im}\Sigma_2(\vec{\mathbf{k}}, \epsilon_{\vec{\mathbf{k}}}) \sim \int_0^{\epsilon_{\vec{\mathbf{k}}}} d\omega \int_0^{q_{\max}} dq\, \mathrm{Im}\Pi(q, \omega) \tag{3.11}$$

where $q_{\max} \sim |\Lambda|/v_{\mathrm{F}}$, and v_{F} is the Fermi velocity in these regions. By combining Equations(3.10) and (3.11), we find:

$$\mathrm{Im}\Sigma_2(\vec{\mathbf{k}}, \epsilon_{\vec{\mathbf{k}}}) \propto \begin{cases} \epsilon_{\vec{\mathbf{k}}}^{3/2} & \text{Van Hove} \\ \epsilon_{\vec{\mathbf{k}}}^{2} & \text{nesting} \end{cases} \tag{3.12}$$

According to Eq.(3.12) the usual Fermi liquid result is recovered for the regular parts of the Fermi surface near almost nested regions. This result arises from the fact that the small momentum response of a quasi–one–dimensional metal does not differ qualitatively from that predicted by Landau's theory of a Fermi liquid while, close to the Van Hove singularities, the energy dependence of the $\mathrm{Im}\Sigma_2(\vec{\mathbf{k}}, \epsilon_{\vec{\mathbf{k}}})$ presents anomalous exponents.

The effects induced by inflection points have been addressed in [50, 51], where the instabilities of anisotropic 2D systems are analyzed. Near the inflexion points, the dispersion relation can be expanded about the Fermi level and satisfies

$$\epsilon_{\vec{\mathbf{k}}} \approx \begin{cases} v_F k_\parallel + b_1 k_\perp^3 & \text{inflexion point} \\ v_F k_\parallel + b_2 k_\perp^4 & \text{special inflexion point} \end{cases} \tag{3.13}$$

where $k_\parallel$ is the momentum parallel to the FS relative to k_F, $k_\parallel = (\vec{\mathbf{k}} - \vec{\mathbf{k}}_F)_\parallel$, $k_\perp$ is the momentum perpendicular to the FS relative to k_F, $k_\perp = (\vec{\mathbf{k}} - \vec{\mathbf{k}}_F)_\perp$, and $b_{1,2}$ are constants. The special inflexion points lie along a reflection symmetry axis of the BZ[51] (the $k_x = k_y = k_0$ points). We use the techniques previously developed in Ref.[[50, 51]] to obtain the second order self-energy near an inflection point:

$$\mathrm{Im}\Sigma_2(\vec{\mathbf{k}}, \epsilon_{\vec{\mathbf{k}}}) \propto \epsilon_{\vec{\mathbf{k}}}^{3/2} \tag{3.14}$$

In the case of an special inflexion point, where the Fermi surface changes from convex to concave and a pair of inflection points are generated for $\epsilon_{\mathrm{F}} = \epsilon_0$ and $\tilde{\mathbf{k}} \equiv (k_0, k_0)$ defined earlier, the imaginary part of the self-energy behaves as $\mathrm{Im}\Sigma_2(\vec{\mathbf{k}}, \epsilon_{\vec{\mathbf{k}}}) \propto \epsilon_{\vec{\mathbf{k}}}^{5/4}$.

Once the imaginary part of the self-energy is known, we can obtain the real part of the self-energy from it by means of a Kramers-Kronig transformation. Although $\mathrm{Im}\Sigma_2(\vec{\mathbf{k}}, \epsilon_{\vec{\mathbf{k}}})$ has been given for $\omega = \epsilon_{\vec{\mathbf{k}}}$, since we are in the weak coupling

regime $U \simeq \Lambda \ll \epsilon_{\rm F}$, where $\epsilon_{\rm F}$ is of the order of the non-interacting bandwidth, then the imaginary part of the self-energy associated to a state with energy $\epsilon_{\tilde{\mathbf{k}}}$ is only significant in an energy range $-\Lambda + \epsilon_{\tilde{\mathbf{k}}} \leq \omega \leq \Lambda + \epsilon_{\tilde{\mathbf{k}}}$. We assume that one can approximate ${\rm Im}\Sigma_{\tilde{\mathbf{k}}}(\omega)$ in this range by an expansion on $(\omega - \epsilon_{\tilde{\mathbf{k}}})/W$, where W is an energy scale of the order of the bandwidth in the non interacting problem, and keep only the lowest order term. This approximation neglects contributions from a region of energies centered around $|\omega - \epsilon_{\tilde{\mathbf{k}}}| \simeq \Lambda$ and of width $\delta\Lambda$, which is, at most, a fraction of Λ. The contribution of the Kramers-Kronig transformation performed in this region of energies is, at most, of order ${\rm Im}\Sigma_{\tilde{\mathbf{k}}}(\Lambda)$ and does not modify the dependence of ${\rm Re}\Sigma_{\tilde{\mathbf{k}}}(\epsilon_{\tilde{\mathbf{k}}})$ on the local properties of the Fermi surface. Therefore we can obtain the real part of the self-energy from the imaginary part by a Kramers-Kronig transformation, and restricting the frequency integral to the interval $0 \leq \omega \leq \Lambda$, we obtain:

$$
{\rm Re}\Sigma_2(\vec{\mathbf{k}}, \epsilon_{\vec{\mathbf{k}}}) \propto -g^2 |\Lambda| \times \begin{cases} \log^2 \left(\frac{\Lambda}{\epsilon_{\vec{\mathbf{k}}}} \right) & \text{Van Hove} \\ \log \left(\frac{\Lambda}{\epsilon_{\vec{\mathbf{k}}}} \right) & \text{nesting} \end{cases} \tag{3.15}
$$

where the negative sign is due to the fact that it is a second order contribution in perturbation theory, and g is a dimensionless coupling constant of order U/W. The sign is independent of the sign of U in Eq.(3.1). In the regular parts of the Fermi surface, Eq.(3.12) leads to:

$$
{\rm Re}\Sigma_2(\vec{\mathbf{k}}, \epsilon_{\vec{\mathbf{k}}}) \propto \begin{cases} -g^2 \frac{|\Lambda|^{3/2}}{W^{1/2}} & \text{Van Hove} \\ -g^2 \frac{|\Lambda|^2}{W} & \text{nesting} \end{cases} \tag{3.16}
$$

where the additional powers in W arise from the m^* and $v_{\rm F}$ factors in the susceptibility, expressed in Eq.(3.10).

In the limit $\Lambda/W \rightarrow 0$, the different dependence on Λ of the self-energy corrections at different regions of the Fermi surface is enough to give a qualitative description of the changes of the Fermi surface. For instance, when the non interacting Fermi surface is close to the saddle point, $\tilde{\mathbf{k}} \equiv a^{-1}(\pm\pi, 0), a^{-1}(0, \pm\pi)$, the self-energy correction is negative and highest in this region. Note that the logarithmic divergences in Eq.(3.15) are regularized by the temperature or elastic scattering.

At band fillings where the FS lies close to the Van Hove singularities, most part of the low energy states close to the Fermi energy, are around the saddle points $(0, \pm\pi)$ and $(\pm\pi, 0)$ (see Fig.(3.2)). Strong screening processes arise due to the big density of states at these points, and if the chemical potential of the system is kept fixed, i.e., the system is in contact with a charge reservoir, the number of particles varies and the Fermi energy tends to be pinned at the Van Hove singularities [53]. Then, in order to remove the Fermi surface from a Van

Hove point or nesting situation, a large number of electrons must be added to the regular regions. When the points of the FS near these hot spots are at distance k from the hot spot, the change in the self-energy needed to shift the Fermi surface by an amount δk is, using Eq.(3.15),

$$\delta\Sigma \propto g^2 \Lambda \frac{\delta k}{k} \tag{3.17}$$

with additional logarithmic corrections near a Van Hove singularity. Near the regular regions of the Fermi surface, a shift in energy of order $\delta\Sigma$ leads to a change in the momentum normal to the Fermi surface of magnitude $\delta k_{\rm reg} \sim \delta\Sigma / v_{\rm F}$. The area covered in this shift gives the number of electrons which are added to the system near the regular regions of the Fermi surface. We find

$$\delta n \sim k_{\rm max} \delta k_{\rm reg} \sim g^2 \frac{k_{\rm max}\Lambda}{v_{\rm F}} \frac{\delta k}{k} \tag{3.18}$$

where $k_{\rm max} \sim a^{-1}$ determines the size of the regular regions of the Fermi surface. The value of δn diverges as the Fermi surface moves towards the hot spot, $k \to 0$. Hence, the number of electrons needed to shift the FS away from the hot spot also diverges. This result has been obtained from calculations at fixed chemical potential[49, 53], where the presence of a charge reservoir is considered, with regular self-energy corrections. This situation has particular interest when studying the physics of high-T_c cuprates, where doping of the CuO_2 layers and interactions with the rest of the perovskite structure are important. The pinning of the Fermi level to the Van Hove singularity has been investigated in the 2D $t-t'$ Hubbard model by RG techniques[54], taking into account the formation of flat bands due to the renormalization of the electron spectrum. The pinning of the Fermi level to the Van Hove singularities is found without making use of a reservoir, and the chemical potential of the system remains practically constant in a range of dopings near the Van Hove filling.

3.3.2 Self-energy corrections to regular Fermi surfaces.

In this section we study a 2D system at a band filling which yields a curved FS, slightly anisotropic, in the absence of singularities. Near the Fermi surface, by choosing an appropriate coordinate system, the electronic dispersion can be approximated by:

$$\epsilon_{\vec{\mathbf{k}}} = v_F k_\perp + \beta k_\parallel^2 \tag{3.19}$$

where $\epsilon_{\vec{\mathbf{k}}} = \varepsilon(\vec{\mathbf{k}}) - \epsilon_{\rm F}$, $k_\perp$ is the momentum perpendicular to the FS relative to k_F, $k_\perp = (\vec{\mathbf{k}} - \vec{\mathbf{k}}_F)_\perp$, $k_\parallel$ is the momentum parallel to the FS relative to k_F, $k_\parallel = (\vec{\mathbf{k}} - \vec{\mathbf{k}}_F)_\parallel$, $v_{\rm F}$ is the Fermi velocity at any particular point $v_{\rm F} = \hat{\mathbf{n}}_\perp \cdot \nabla\varepsilon(\vec{\mathbf{k}})$,

and β is related to the local curvature of the Fermi surface $b = \hat{\mathbf{n}}_{\|} \cdot \left(\nabla^2 \varepsilon(\vec{\mathbf{k}}) \right) \hat{\mathbf{n}}_{\|}$, by $\beta = b v_F/2$. This expansion implies, without assuming any rotational symmetry, a FS locally indistinguishable from a circular one, where the energy Eq.(3.19) would correspond to a radius $k_F = m_F v_F$, where we have renamed $\beta = 1/2m_F$, being m_F the effective mass. The Fermi velocity v_F and the FS curvature b, are functions of $t, t', \epsilon_{\mathrm{F}}$ and the position along the Fermi line. We calculate the second order diagram of Fig.(3.3), assuming that the main contribution to the self-energy arises from processes where the momentum transfer is small, forward scattering channel, or from processes which involve scattering from the region under consideration to the opposite part of the Fermi surface, *i. e.*, backward scattering. This assumption can be justified by noting that we are considering a local Hubbard interaction, which is momentum independent, so that the leading effects are associated to the structure of the density of states. The processes discussed here have the highest joint density of states.

These polarizabilities are calculated in order to obtain the self-energy Eq.(3.6). The imaginary part of $\Pi(\vec{\mathbf{q}}, \omega)$ for the forward channel is, using Eq.(3.7) and the parametrization from Eq.(3.19) (see A for details on the calculation):

$$\mathrm{Im}\Pi^{\mathrm{F}}(\tilde{\mathbf{q}}, \omega) = -\frac{\mathrm{U}^2}{16\pi} \frac{|\omega|}{\beta \mathrm{v_F}} \sqrt{\frac{2\beta}{\omega - \mathrm{M}^{\mathrm{F}}_{\tilde{\mathbf{q}}}}} \tag{3.20}$$

where $\vec{\mathbf{q}}$ is a small vector that connects two pieces close together in the FS and $\mathrm{M}^{\mathrm{F}}_{\tilde{\mathbf{q}}} = \mathrm{v_F} \mathrm{q}_{\perp} + \frac{2}{9}\beta \mathrm{q}^2_{\|}$. The argument of the square root has to be positive, what gives an extra condition, $\omega \, \mathrm{sgn}(\beta) > \mathrm{M}^{\mathrm{F}}_{\tilde{\mathbf{q}}} \, \mathrm{sign}(\beta)$. Similarly, for the backward scattering we obtain:

$$\mathrm{Im}\Pi^{\mathrm{B}}(\tilde{\mathbf{Q}}+\tilde{\mathbf{q}}, \omega) = -\frac{\mathrm{U}^2}{16\pi} \frac{1}{\beta \mathrm{v_F}} \begin{cases} \sqrt{2\beta(|\omega| + \mathrm{M}^{\mathrm{B}}_{\tilde{\mathbf{q}}})} - \sqrt{2\beta(\mathrm{M}^{\mathrm{B}}_{\tilde{\mathbf{q}}} - |\omega|)} \, \text{if } |\omega| < \mathrm{M}^{\mathrm{B}}_{\tilde{\mathbf{q}}} \, \mathrm{sgn}(\beta) \\ \mathrm{sgn}(\beta) \sqrt{2\beta(|\omega| \mathrm{sgn}(\beta) + \mathrm{M}^{\mathrm{B}}_{\tilde{\mathbf{q}}})} \qquad \text{if} \quad |\omega| > |\mathrm{M}^{\mathrm{B}}_{\tilde{\mathbf{q}}}| \end{cases} \tag{3.21}$$

where $\vec{\mathbf{q}}$ is the deviation of the wave-vector from the vector $\vec{\mathbf{Q}}$ that connects the region studied with the opposite part of the FS, and $\mathrm{M}^{\mathrm{B}}_{\tilde{\mathbf{q}}} = \mathrm{v_F} \mathrm{q}_{\perp} - \frac{2}{9}\beta \mathrm{q}^2_{\|}$. For $\vec{\mathbf{q}} = 0$ we have that $\mathrm{Im}\Pi^{\mathrm{B}}(\tilde{\mathbf{Q}} + \tilde{\mathbf{q}}, \omega) \sim \sqrt{|\omega|}$, in accordance with Ref.[55], where they study a spin-fluctuation model for the $Q = 2k_F$ instability. For small ω and fixed $\vec{\mathbf{q}}$ we have, expanding Eq.(A.21) up to first order in $|\omega|/\mathrm{M}^{\mathrm{B}}_{\tilde{\mathbf{q}}}$ (for the case $|\omega| < \mathrm{M}^{\mathrm{B}}_{\tilde{\mathbf{q}}} \, \mathrm{sgn}(\beta)$), that $\mathrm{Im}\Pi^{\mathrm{B}}(\tilde{\mathbf{Q}} + \tilde{\mathbf{q}}, \omega) \sim |\omega|$, as expected for a Fermi-liquid[55].

Introducing the values of $\Pi(\vec{\mathbf{q}}, \omega)$ in Eq.(3.6) we can obtain the imaginary part of the self-energy, which describes the decay of quasiparticles in the region under consideration and that it is independent of the cutoff Λ. The contribution from

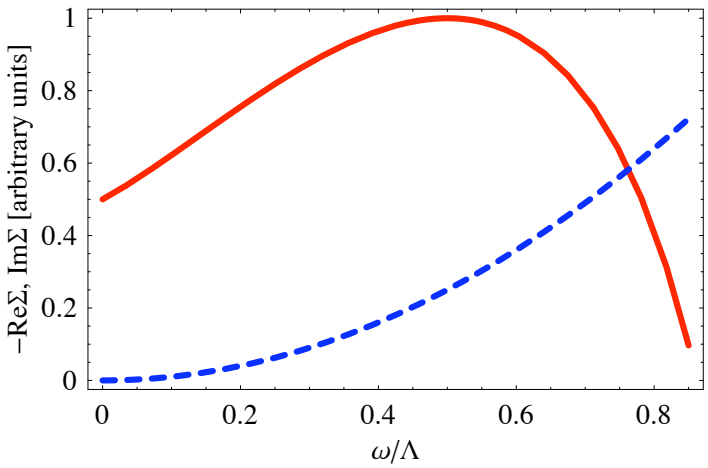

Figure 3.4: Real and imaginary parts of the self energy as a function of the energy ω: full red line $-\mathrm{Re}\Sigma$, dashed blue line $\mathrm{Im}\Sigma$

forward scattering processes is:

$$\mathrm{Im}\Sigma_2(\tilde{\mathbf{k}},\omega) = \frac{3}{64}\frac{\mathrm{U}^2\mathrm{a}^4}{\sqrt{2}\pi^2}\frac{\omega^2}{\mathrm{v}_\mathrm{F}^2|\beta|} \ . \tag{3.22}$$

The quadratic dependence of energy is expected, and consistent with Landau's theory of a Fermi liquid. This contribution diverges as $v_\mathrm{F} \to 0$, that is, when the Fermi surface approaches a Van Hove singularity, or as $|b| \to 0$ which signals the presence of an inflection point or nesting. The contribution due to backward scattering is exactly the same as that from forward scattering, Eq.(A.32), with the same numerical prefactors.

Using a Kramers-Kronig transformation, and integrating in the interval $0 \leq \omega \leq \Lambda$, we obtain:

$$\mathrm{Re}\Sigma_2(\tilde{\mathbf{k}},\omega) = -\frac{3}{64}\frac{\mathrm{U}^2\mathrm{a}^4}{\sqrt{2}\pi^3}\frac{1}{\mathrm{v}_\mathrm{F}^2|\beta|}\left[\Lambda^2 + 2\Lambda\omega + 2\omega^2\log\left|\frac{\Lambda-\omega}{\omega}\right|\right] \tag{3.23}$$

From the experimental point of view the determination of the scattering rate ($\mathrm{Im}\Sigma(\vec{\mathbf{k}},\omega)$) presents particular interest and big effort has been devoted in order to obtain it: by ARPES because of the momentum and energy resolved measurements [56, 57, 36, 23] and recently by electrical transport experiments at microwave frequencies[58]. The extraction of the correlation functions from the experimental data is a complicated task and, although many theoretical approximations exist, the computation of correlation effects is also difficult. From ARPES results in underdoped and optimally doped cuprate samples [57] an anisotropic

scattering rate around the Fermi surface have been found and the bare Fermi velocity has been directly obtained. By using a different methodology the real and imaginary parts of the self-energy has been obtained from photoemission data by a self-consistent procedure [36].

In Fig.[3.4] we represent the self-energy as a function of the frequency according to results from Eqs.(A.32,3.23), where the linear (quadratic) behavior of the real (imaginary) part of the self-energy at low frequencies, typical of a Fermi liquid system, is recovered. We find a qualitative agreement with the low-energy part of the self-energy functions extracted self-consistently from the experiment in Ref.[36]. It should be notice that we consider here the electron-electron scattering only. The impurity and electron-phonon scattering will, no doubt, cause finite life-time and energy renormalization of the excitations but our main concern is the self-energy due to electron-electron correlation. The impurity scattering term can be considered to be isotropic (from an isotropic distribution of static impurity scatterers) an it will give a constant term in $\mathrm{Im}\Sigma(\vec{\mathbf{k}},\omega)$. The electron-phonon self-energy can be assumed to be small at low temperature. Then, the assumption that the dominant scattering mechanism is the electron-electron interaction in the systems under study is justified[23].

As a last result, from the real part of the self-energy Eq.(3.23), we can calculate the quasiparticle-weight

$$Z_{\vec{\mathbf{k}}_F} = \left(1 - \frac{\partial \mathrm{Re}\Sigma(\tilde{\mathbf{k}}_\mathrm{F},\omega)}{\partial\omega}\right)^{-1}_{\omega\to 0} \tag{3.24}$$

which for our case reads

$$Z_{\vec{\mathbf{k}}_\mathrm{F}} = \frac{1}{1+\frac{3\sqrt{2}a^4}{64\pi^3}\frac{U^2\Lambda}{|\beta|v_\mathrm{F}^2}} \tag{3.25}$$

The result given in Eq.(3.25) seems reasonable: in the limit of $U \to 0$ (no correlations) the Z = 1 quasiparticle spectral weight would be that of a free electron gas at $T = 0$. The opposite limit, when $U \to \infty$ for a extremely correlated system, leads to the destruction of the quasiparticle coherence (Z $\to$ 0). In the weak coupling regime, the quasiparticle-weight would be minimum either if the Fermi velocity becomes very small (Van Hove singularity, consistent with results in Ref.[59]) or if the curvature of the Fermi surface changes sign (inflexion point).

Finally, from Eq.(3.23) we obtain the expression which gives the zero frequency limit of the real part of the self-energy

$$\mathrm{Re}\Sigma_2(\tilde{\mathbf{k}},\omega=0) = -\frac{3}{64}\frac{\mathrm{U}^2\mathrm{a}^4}{\sqrt{2}\pi^3}\frac{\Lambda^2}{\mathrm{v}_\mathrm{F}^2|\beta|} \tag{3.26}$$

which renormalizes the FS according to

$$\epsilon_{\rm F} - \varepsilon(\vec{\mathbf{k}}) - {\rm Re}\Sigma(\vec{\mathbf{k}}, \omega = 0) = 0 \tag{3.27}$$

3.3.3 Application to Fermi surfaces of copper oxides superconductors

As stated in the Introduction, copper oxides superconductors have a strongly anisotropic layered structure. Cuprates present anomalous properties in many physical aspects and are one of the main challenges to condensed matter physics. The peculiarities of the phase diagram have been addressed by different techniques and no consensus has been reached. Experimental results indicate a behavior far from the Fermi liquid, and the changes induced by doping on the ground state character of the normal state add complexity to the problem. Both, the low dimensionality (CuO_2 planes) together with the strong electronic correlations, have to be taken into account to understand the low energy excitation spectrum of the cuprates. The effects of the strong correlations on the Fermi surface shapes of the cuprates is a hot issue. Recently Civelli *et al.* [33] have addressed the problem by using an extension of the dynamical mean-field theory, the cellular dynamical mean-field theory (CDMFT) which allows the study of $k-$dependent properties. They study the 2D Hubbard model in the strongly correlated regime ($U = 16t$). A strong renormalization of the FS shape, due to interactions, is found together with a momentum space differentiation: appearance of hot and cold regions in the Brillouin zone.

We study as well the two dimensional Hubbard model on a square lattice, and we will consider hopping amplitudes t_{ij} to nearest-neighbors t and to next nearest neighbors t'. Since we are in the perturbative regime we consider local weak coupling instead the strong coupling addressed in reference [33]. We adopt the hopping values $t = -1$ and $t' = -0.3t$ which mimic the hole-doped cuprates ($t/t' < 0$), and we will consider two different doping levels. In Eq.(3.26) we can see how the self-energy corrections due to electron-electron interactions depend on local features of the non-interacting FS, as the Fermi velocity $v_{\rm F}$ and the curvature b. For the dispersion relation given by Eq.(4.3), the expressions derived for the Fermi velocity and the curvature (taking for simplicity $a = 1$) at the Fermi level, are:

$$v_F(\vec{\mathbf{k}}) = \sqrt{(t + 2t'\cos k_y)^2 \sin^2 k_x + (t + 2t'\cos k_x)^2 \sin^2 k_y} \tag{3.28}$$

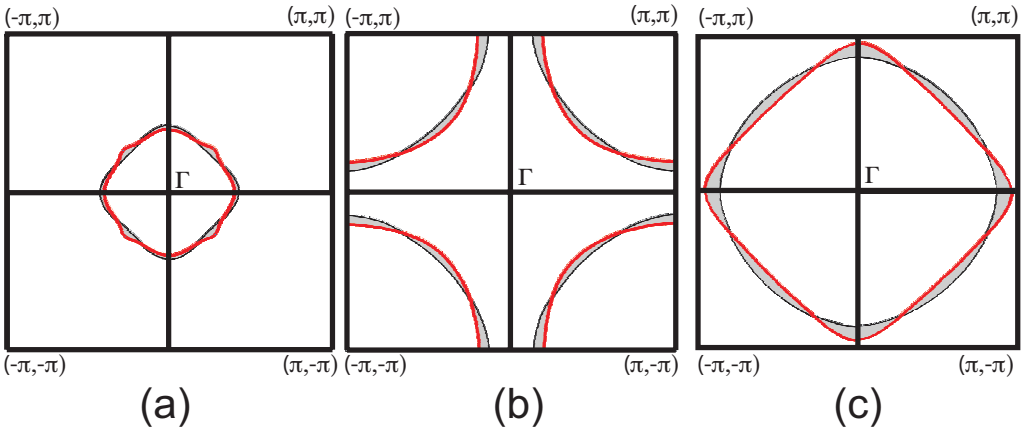

Figure 3.5: (Color online) Deformations induced by the interactions on the FS of the $t - t'$ Hubbard model. The axes are labelled in units of a^{-1}, where a is the lattice constant. Black line represents the unperturbed FS while the red line represents the FS corrected by the interaction. For $t'/t = -0.3$ (a): high doping range and (b) close to half filling. (c) For $t'/t = +0.3$ close to half filling.

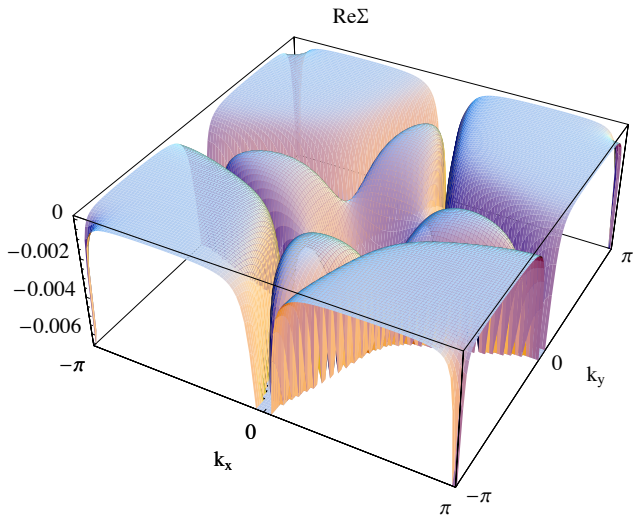

Figure 3.6: Real part of the self-energy for $t' = -0.3t$ represented in the square Brilluoin zone.

$$b(\vec{\mathbf{k}}) = -\frac{(t+2t'\cos k_x)(t+2t'\cos k_y)}{\left[(t+2t'\cos k_y)^2\sin^2 k_x + (t+2t'\cos k_x)^2\sin^2 k_y\right]^{3/2}} \times \\ \left[t\cos k_y \sin^2 k_x + 2t'\cos^2 k_y \sin^2 k_x + (t\cos k_x - t'(-3+\cos 2k_x))\sin^2 k_y\right] \tag{3.29}$$

where $\vec{\mathbf{k}} = (k_x, k_y)$ sets for the Fermi momentum $\vec{\mathbf{k}}_F = (k_{\mathrm{Fx}}, k_{\mathrm{Fy}})$These expressions illustrate the momentum dependence of the self-enegy corrections. At high doping, the FS presents an almost square shape with rounded corners. We find that the self-energy corrections are stronger for the regions with the smallest curvature at the diagonal parts of the BZ. This behavior, shown in Figure[3.5](a) for $\epsilon_{\mathrm{F}} = -2.3 \approx 8t'$, is similar to the result obtained by Freire *et al.* in [60] for the renormalization of a flat FS by a two-loop field theory RG approach, where interactions induce a small curvature to the bare flat FS. They found as well that, the renormalized FS, becomes truncated due to the interactions, not found here. Next we will consider a lower doping level. By changing the filling, the FS shape varies, and close to half-filling, for $\epsilon_{\mathrm{F}} = -0.9 = 3t'$, the FS has the form shown in Figure[3.5](b). The change in shape qualitatively agrees with the doping evolution of k_F measured by ARPES on cuprates [19, 20], and the FS shape is similar to the FS reported in different experiments. At this doping, close to half-filling, the self-energy corrections enhance the hole-like curvature around $(\pm\pi, \pm\pi)$ and $(\pm\pi, \mp\pi)$, and flatten the FS close to the $(\pm\pi, 0)$ and $(0, \pm\pi)$ points of the BZ as it is shown in Fig.[3.5](b). This result coincides with the renormalization found in [33] even though they are in the strongly correlated regime.

Corrections found in Figure[3.5] can be understood by looking at Figure[3.6], where the real part of the self-energy is depicted at $\omega = 0$ in the square BZ. At the central region of the BZ near the Γ point, the main corrections occur around the diagonal of the BZ, as we have found in the high doping case, where the flat parts of the non-interacting FS become curved. At this point, the larger contribution to $\mathrm{Re}\Sigma(\vec{\mathbf{k}}, \omega)$ will be due to the curvature of the Fermi surface, which is almost flat in the nodal region at this value of the band filling. In fact, it can be observed in Figure[3.6], following the $(-\pi, -\pi) - (\pi, \pi)$ diagonal line, that the minima of $\mathrm{Re}\Sigma(\tilde{\mathbf{k}}, \omega)$ coincide with the minima of the curvature, that corresponds to the maximum correction to the non-interacting FS.

Looking again at Figure[3.6] we see that, for higher fillings, the corrections are more pronounced where inflexion points start to appear in the Fermi surface (see Figure[3.2]). The first of these inflexion points k_0 occurs in the diagonal of the BZ, in the nodal direction. Once this first inflexion point appears, if we increase the occupation of the BZ towards half-filling, new inflexion points merge in each FS

and they distribute themselves symmetrically with respect to the diagonals of the BZ. This is why the *divergence valley* has this star-like structure. Finally, at lower doping levels, as that represented on the right panel of Figure[3.5], the Fermi line reaches the region closer to the border of the BZ, and the main corrections appear at the proximity of the antinodal points $(0, \pm\pi)$, $(\pm\pi, 0)$. As can be observed in Figure[3.6], $\mathrm{Re}\Sigma(\vec{\mathbf{k}}, 0)$ shows pronounced dips close to the saddle points, and therefore the FS is renormalized in this region. These minima are due to Van Hove singularities where the v_{F} vanishes.

This result agrees with one-loop functional RG calculation of the self-energy in the weak coupling regime of the 2D $t-t'$- Hubbard model at Van Hove band fillings [59] where vanishing of the quasiparticle-weight on approaching the antinodal points is found. Away from the Van Hove fillings a quasiparticle peak, with small spectral weight, emerges at $(\pi, 0)$ and $(0, \pi)$.

The case of an electron doped system can be analyzed by a particle-hole transformation of the Hamiltonian which reverses the sign of t', $(t/t' > 0)$. For $t' = +0.3t$ we find that, close to half-filling, the self-energy corrections are stronger in the proximity of the saddle points, where $v_{\mathrm{F}} \to 0$. As can be seen in Fig.[3.5](c), the corrected FS is closer to a nesting situation than the bare FS.

Our results, near half-filling, are in overall agreement with those of reference[33], although we find that the self-energy corrections are stronger at the antinodal region in both, hole-like and electron-like, Fermi surfaces.

3.3.4 Application to Fermi surface of Sr_2RuO_4

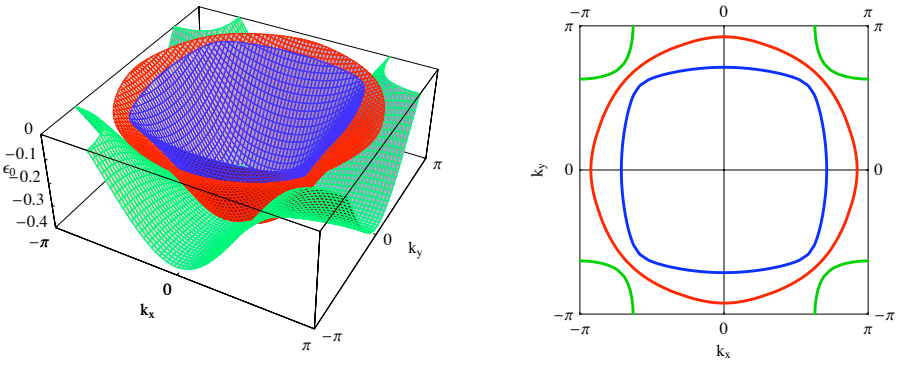

Figure 3.7: (Color online) Left: Band structure of Sr_2RuO_4 obtained from Eq.(3.30) using the parameter values given in Ref.[61]. The blue sheet corresponds to the α-band, the red sheet is the β-band and the green sheet correspond to the γ-band. Right: Corresponding Fermi surface.

Sr_2RuO_4 is a highly anisotropic layered compound, with an electrical anisotropy

of about 4000 [62]. It has a strongly two-dimensional electronic structure and exhibits a good Fermi liquid behavior below 30K, as probed by bulk transport measurements[62]. The Fermi surface measured by ARPES matches the de Haas van Alphen measurements and it can be well described by band structure calculations. Therefore Sr_2RuO_4 is considered a correlated 2D material. As it occurs in the cuprates, the competition between superconducting and magnetic instabilities play an important role in the low energy physics of Sr_2RuO_4 which, with a critical temperature of about $T_c \approx 1.5$K, presents an unconventional superconductivity with a p-wave and spin-triplet pairing[63]. This material has three relevant bands[64], α, β, and γ, of t_{2g} symmetry, formed from the $4d$-orbitals of the Ru^{4+} ion. The $\{\alpha, \beta\}$ bands are derived from $\{d_{xz}, d_{yz}\}$ orbitals and form two quasi-one-dimensional bands along the directions z and y respectively, that are weakly hybridized. The γ band is derived from the d_{xy}-orbital and disperses into a real 2D band. In Figure[3.7] are depicted the electronic structure, left panel and corresponding FS, right panel, calculated following the dispersion relation

$$\begin{aligned}
\varepsilon_\gamma(\vec{\mathbf{k}}) &= -2t_{1\gamma}(\cos(k_x a) + \cos(k_y a)) - 4t_{2\gamma}\cos(k_x a)\cos(k_y a) - \varepsilon_{0\gamma} \\
\varepsilon_{\alpha,\beta}(\vec{\mathbf{k}}) &= -(t_{1\alpha,\beta} + t_{2\alpha,\beta})(\cos(k_x a) + \cos(k_y a)) \\
&\quad \pm\sqrt{((t_{1\alpha,\beta} - t_{2\alpha,\beta})(\cos(k_x a) - \cos(k_y a)))^2 + 16t_{3\alpha,\beta}^2 \sin(k_x a)^2 \sin(k_y a)^2} - \varepsilon_{0\alpha,\beta}
\end{aligned} \tag{3.30}$$

The tight-binding parameters are taken from references[61, 64]. This FS is in good agreement with that reported by ARPES experiments and obtained by band calculations. As before the self-energy corrections to the three sheets of the FS depend on the Fermi velocity and the curvature (not given here due to its size). In Figure[3.9] we can see the momentum dependence of the Fermi velocity for the three bands. It is easy to appreciate that the minima of the three plots are, besides in the Γ point, in the antinodal points, $(\pm\pi, 0)$ and $(0, \pm\pi)$, and in the diagonal of the BZ, $(\pm\pi, \pm\pi)$ and $(\pm\pi, \mp\pi)$.

The momentum dependence of the real part of the self-energy for the three bands is shown in Figure[3.10]. In the left hand side we can see the correction to the α-sheet, that is significant only either when the Fermi line lies near the Γ-point or in the proximity of the corners of the BZ, $(\pm\pi, \pm\pi)$ points. In the central figure, the contribution corresponding to the β-band is shown. Here we can see that the correction is maximum (most negative) in the zones between the diagonals, due to the nearly flat regions of the Fermi line corresponding to the β-band.

Finally, the corrections to the γ-band are shown in the right hand side of Figure[3.10] (notice the different scales in the three graphs). In this case the corrections are maxima near the antinodal points $(\pm\pi, 0)$ and $(0, \pm\pi)$, due to the

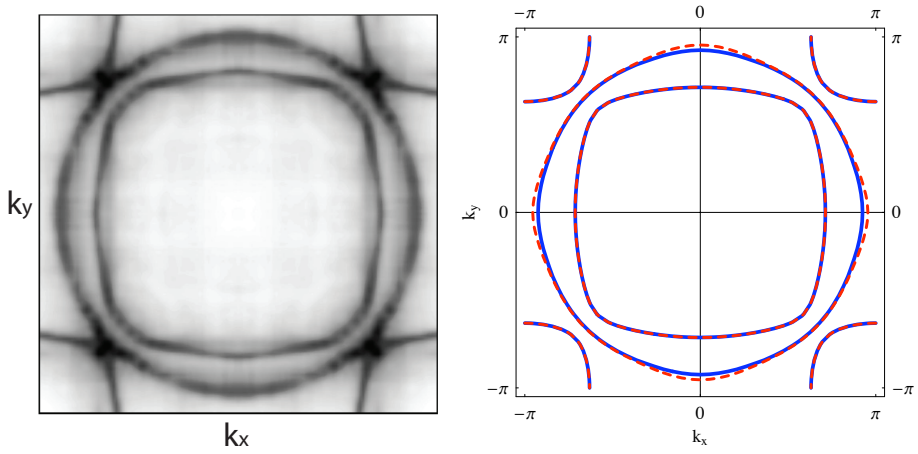

(a) (b)

Figure 3.8: (a) Fermi surface of Sr_2RuO_4reported by Damascelli *et al.* in Ref.[65] (b) Bare (continue blue) and interacting (dashed red) Fermi surface obtained by the present method.

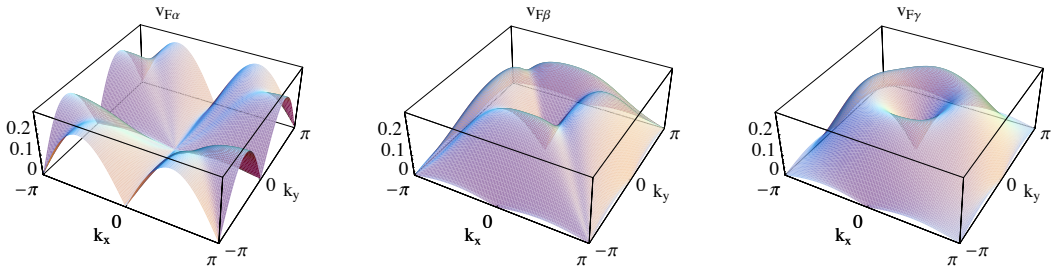

Figure 3.9: Fermi velocity of the non-interacting bands: Left graph corresponds to the α-band, center graph corresponds to β-band and right graph corresponds to γ-band of Sr_2RuO_4.

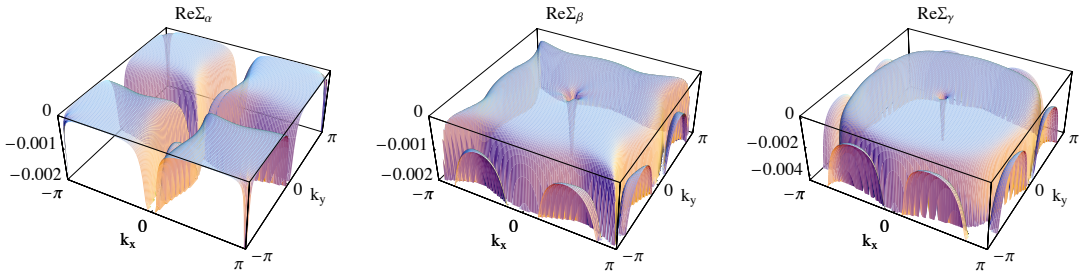

Figure 3.10: Real part of the self-energy corrections for the three bands of Sr_2RuO_4 in the first square BZ: Left graph corresponds to the α-band, middle to the β-band, and right graph corresponds to γ-band. We have used the parameter values $U = 0.01$ and $\Lambda = 1$. Notice the different scales in the three graphs.

proximity of this band to a Van Hove point. In reference[61] it is pointed out that calculated γ-band properties depend very sensitively on how close it approaches the Van Hove points $(\pi,0)$, $(0,\pi)$.

The main corrections occur at the γ-band as it is shown in Figure[3.8(b)] where the bare and renormalized FS are depicted. Here non-interacting FS (full blue line) is changed, due to electron-electron correlations, to the interacting FS (dashed red line).

The corrections in the α and β bands are due to curvature effects, while the corrections to the γ band are due to Fermi velocity effects, because of the proximity of this band to the saddle points, as it has been pointed out above. Then, in agreement with ARPES measurements[23] and other theoretical results[61], the main corrections induced in the FS of Sr_2RuO_4 occur at the γ-band corresponding sheet. The importance of the FS geometry has been analyzed in Ref.[61] where the non-analytic corrections to the specific heat and susceptibility of a 2D Fermi liquid have been considered and the results applied to Sr_2RuO_4. Both, the dependence of the γ band properties on how close the band approach the Van Hove points and the dominant interaction in the γ band are found in Ref.[[61]], because it has the largest mass and the largest susceptibility enhancement.

Similarly, the importance of the band structure properties of these materials can be seen in the context of multi-layer ruthenates, for which the proximity of their Fermi surface to a Van Hove singularity can give rise to a quantum critical end-point in the magnetic phase diagram, as it is found, within a mean-field analysis, in Ref.[66].

Once we know the self-energy, one can calculate the spectral function $A(\vec{\mathbf{k}},\omega)$, given in Eq.(2.7). We have done so for each band of Sr_2RuO_4in the limit $\omega \to 0$. The result is represented in Fig.[3.11].

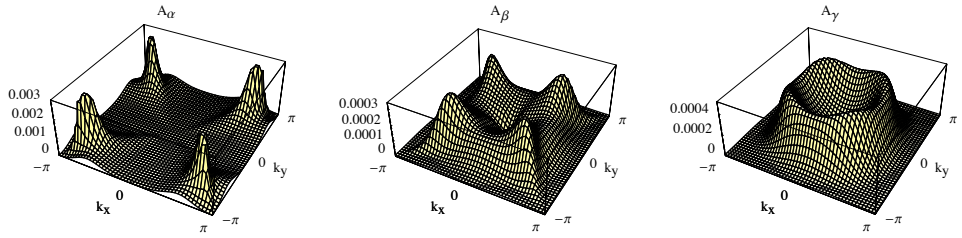

(a)

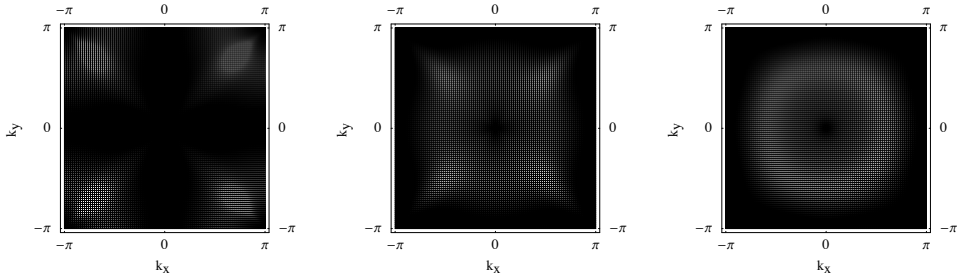

(b)

Figure 3.11: Spectral function of the three bands of Sr_2RuO_4.

3.4 Conclusions.

The unconventional physics shown by anisotropic materials, as high-T_c superconductors and ruthenates, poses big difficulties when a theoretical model has to be chosen. On the other hand, although it is generally accepted that the many-body interactions of electrons play a key role in the underlying physics of these compounds and may be related to the occurrence of superconductivity in the cuprates, a consensus has not been reached about the origin of important features widely observed by different experimental techniques. The anisotropy momentum space shown by many electronic properties of the planes adds complexity to the possible theories.

In the cuprates, the pseudogap phase, metallic but with a broken Fermi surface (segments known as Fermi arcs[67]) is an example of the remarkable momentum dependence of the interactions. Furthermore the band renormalization observed by ARPES in different families of high T_c superconductors, known as kink in the dispersion, which indicates a strong coupling to a collective mode (see Ref.[[**?**]] and references therein), shows different energy scales and temperature dependence at the nodal and antinodal regions of the BZ, suggesting two different kinks of different origin, which nature is under debate: both phonon and magnetic mode have been suggested as possible causes.

More recently a high energy anomaly in the spectral function has been observed in three different families of high-T_c superconductors, and apparently in several ruthenate compounds[68]. This anomaly indicates that the quasi-particles at ϵ_F are dressed not only by the interactions with bosons at low energy, but also by interactions at higher energies. This peculiar high energy behavior together with the unconventional low energy properties, poses a challenge on theoretical models.

The knowledge of the dressed FS is crucial to understand the behavior of correlated materials, especially when an effective model is needed to explain the unconventional physics. We have presented in this chapter a simplified way of taking into account the self-energy corrections to the Fermi surface. We have made use of the different dependence of the self-energy on the high energy cutoff in order to analyze the main features of the changes of the FS. The analysis presented here is valid only at weak coupling, and we do not consider corrections to the interactions or to the wave-function renormalization. On the other hand, the expressions obtained are analytical and related to the local features of the non-interacting FS in a simple way, so that they can be readily used to get an estimate of the corrections expected.

The results suggest that the main self-energy corrections, which are always negative in our scheme, peak when the FS is close to the $(\pm\pi, 0), (0, \pm\pi)$ points in the Brillouin zone. If these contributions are cast as corrections to the hopping elements of the initial Hamiltonian, we find that the nearest neighbor hopping, t, is weakly changed (as it does not contribute to the band dispersion in these regions). The next nearest neighbor hopping, t' which shifts the bands by $-4t'$ in this region, acquires a negative correction. This implies that the absolute value of t' grows when $t' > 0$, or decreases, when $t' < 0$, in reasonable agreement with the results reported in[33]. Note that the tendency observed in our calculation towards the formation of flat regions near these points, when analyzed in higher order perturbation theory, will lead to stronger corrections. Our results also confirm the pinning of the FS near saddle points, due to the interactions. The analysis presented here is consistent with the measured Fermi surfaces of the cuprates[9] and qualitatively agree with the doping evolution reported by ARPES[9, 19, 20]. The self-energy corrections found for the FS of Sr_2RuO_4, which mainly renormalize the γ sheet, are as well in qualitative agreement with ARPES measurements[23] and previous calculations[61]. The broad spectrum of experimental data available at this moment makes comparison between results from different techniques one of the most efficient methods to obtain information about response and correlation functions of unconventional materials. To get an estimation of the self-energy corrections to the Fermi surface in a simple way, independent of the model, as the one here proposed, is helpful in order to gain

insight into many low-energy physics aspects.

Chapter 4

Electronic correlations in the honeycomb lattice. Application to graphene.

4.1 Abstract

The electron-electron interactions effects on the electronic band structure and on the shape of the Fermi surface of graphene are investigated. The actual discrete nature of the lattice is fully taken into account. A π-band tight-binding model, with nearest-neighbor interactions, is considered. We calculate the self-energy corrections at zero temperature. Long and short range Coulomb interactions are included. The exchange self-energy obtained at the Hartree-Fock level for doped graphene presents the same symmetry as the Fermi surface so that the trigonal warping topology is preserved. The band velocity is renormalized to higher value. Self-energy corrections calculated beyond Hartree-Fock, do deform anisotropically the Fermi surface shape, besides renormalizing the band velocity. Results are compared to experimental observations and to other theoretical results.

4.2 Introduction

Carbon is a vital elements for life on Earth and shows a remarkable versatility. Pure carbon can take many forms ranging from graphite to diamond, alongside more recently discovered forms such as the fullerenes, C_{60}, carbon nanotubes and graphene.

The atomic structure of Carbon is $C_6 : 1s^2 2s^2 2p^2$. When atoms are brought together, the way the electrons bond will determine the properties of the material. For carbon atoms two different types of bonding are possible: sp^3 formed by

mixing an s orbital and the three p orbitals forming four equivalent hybrids, carbon atoms form a tetrahedral pattern with four nearest neighbor forming strong bonds, and sp^2 bonding by mixing an s orbital and two p orbitals, leaving the thirth p orbital unchanged. The three hybrids are coplanar with trigonal geometry, carbon atoms arrange in the hexagonal lattice, as in graphite, the σ-coplanar hybrids give rigidity to the lattice while the π-orbitals give the carriers. Carbon atoms with sp^3 bonding form diamond, transparent, the hardest material known, abrassive and insulator. Carbon atoms with sp^2 bonding give graphite, opaque, one of the softest materials lubricant and conductor. Graphite is a layered material very anisotropic, distances between atoms in the layers are 1.4Åwhile the distance between layers is of 3.5Å. From band structure calculations the hopping integrals are of 2.4eV in the planes and 0.3eV between planes, therefore graphite has been study by adopting a two-dimensional model, neglecting interlayer coupling. In 2004 monocrystalline graphitic films of a few atoms thick, including a single atomic layer of graphite, were fabricated in the University of Manchester[69, 70]. Although graphene, a single-layer of graphite, was previously thougth not to be thermodinamically stable, it turned out to be stable under ambient conditions and the team was able to controll the transport properties of the film by varying an external voltage. The films were prepared by mechanical exfoliation (repeated peeling) of highly oriented pyrolitic graphite (HOPG). The dependency of the resistivity, conductivity and Hall coefficient on the gate voltage are quantitatively explained by a model of a 2D metal with a small overlap between conductance and valence bands. Other groups have obtained graphene films [71] and its properties have been measured. It is found that the graphene properties are distinctive of a 2D electron gas described by the Dirac equation rather than the Schrodinger equation, in agreement with theoretical predictions.

Since its discovery graphene has attracted a considerable interest in condensed matter physics , not only because of its unconventional properties but as well because it is the basic block that forms graphite by stacking up several planes, carbon nanotubes by rolling a graphene sheet, and of fullerenes. Furthermore, the peculiar electronic properties shown by graphene make it a promising candidate to a future nanoelectronics.

The electronic properties of graphene are well described by a π-band tight-binding model [72]. At half-filling, the valence and conduction π-bands touch only at the corners, $\mathbf{K}$, of the hexagonal Brillouin zone (BZ) at the Fermi level, E_F. The low-energy physics is described by the relativistic Dirac equation. The dispersion relation turns up to be isotropic and linear near E_F. The low-energy excitations of the systems are Dirac fermions with zero effective mass and a vanishing density of states at the $\mathbf{K}$ points, known as Dirac points. Because of these peculiarities, graphene is considered a model system to investigate basic questions

of quantum mechanics. Due to its transport properties graphene is a promising material for nanoelectronics applications. Recent improvements in experimental resolution have led to high precision measurements of the Fermi surface, and also to the determination of the many-body effects in the spectral function, as reported by angle resolved photoemission spectroscopy experiments [9]. Under these circunstances interest in graphite has been renewed and there are new experimental measurements. In a high-resolution angle resolved photoemission spectroscopy (ARPES) study on disordered graphite samples, coexistence of sharp quasiparticle dispersions and disordered features was found [73], and was explained in terms of Van Hove singularities in the angular density of states. Later on the linear and isotropic dispersion of the bands in the vecinity of the BZ corners **H** points has been directly observed by using ARPES in graphite, coexisting with parabolic dispersion bands [74]. The constant energy maps taken near the **H** point present circular shape from E_F to -0.6eV and start to deviate from the circle at -0.9eV. A linear energy dependence of the quasiparticle lifetime has been as well measured by ultrahigh resolution ARPES on high quality crystals of graphite[75], in agreement with theoretical predictions [49]. The low-energy excitations seems to be dominated by phonons, while those for higher energies are characterized by the electron-hole pair creation[75]. In a combined ARPES and theoretical ab-initio quasiparticle study of the π-band structure and the Fermi surface in graphite single crystals it is found that electron-electron correlation plays an important role in semi-metallic graphite and should be taken into account for the interpretation of experimental results [76]. The electron correlations renormalize the electronic dispersion increasing the Fermi velocity. The equi-energy contours of the photoemission intensity in a BZ point in the **KH** direction show trigonal warping even at -0.1 eV [76].

Electron-electron interactions in graphene are expected to play an important role due to its low dimesionality. From the experimental point of view graphene presents advantages with respect to other 2D systems. Graphene can be controlled externally and exposed to vacuum therefore can be directly probed by different techniques. The quasiparticle dynamics in graphene samples has been addressed by high-resolution ARPES [77]. It was found that the conical bands are distorted due to many body interactions, which renormalize the band velocity and the Dirac crossing energy E_D. Electron-hole pair generation effects are important near the Fermi energy and electron-phonon coupling contribution to the self-energy is also important in the Fermi level region (an electron-phonon coupling constant of $\lambda \approx 0.3$ is deduced with the standard formalism). Around E_D, electron-plasmon coupling is invoqued to explain the peak found in the imaginary part of the self-energy, just below E_D whose width and intensity scales with E_D. Although the three scattering mechanisms contribute to strongly renormalize

the bands, it is claimed that the quasiparticle picture is valid in graphene over a spectacularly wide energy range [77]. More recently, the doping dependence of graphene electronic structure has been investigated by ARPES in graphene samples at different dopings [78]. Upon doping with electrons, the Fermi surface grows in size, its trigonal warping evolving into a concave triangular shape. An electron-phonon coupling to in-plane optical vibrations is invoqued to explain the experimental results. The electron-phonon coupling constant extracted from the data presents a strong dependence on $\vec{\mathbf{k}}$, with maximal value along the KM direction. The presence of a Van Hove singularity (VHS) in the KMK direction, confirmed upon doping, could be a possible explanation of the enhancement of the electron-phonon coupling. The layered nature of graphite/graphene as well as the presence of the VHS in the density of states near the ϵ_{F}, which would enhance many-body effects, make contact with the physics of cuprates superconductors. The similarities between graphene and the cuprates have been already noticed [79] and the important role of many body effects in the basic physics of graphene has been investigated earlier [80]

From the theoretical point of view, graphene offers many possibilities. The self-energy have been object of special interest, since it gives relevant information from fundamental properties. Furthermore, theoretical results can be compare to recent ARPES reported self-energies. In general, self-energy calculations for graphene are carried out in the continuum limit, taken into account the 2D Dirac equation which gives the linear dispersion relation. Many approximations have been followed to investigate the self-energy in graphene. Within the G_0W approximation [81] with a full dynamically screened Coulomb interaction, the inelastic quasiparticle lifetimes have been obtained. The scattering rates calculated for different carrier concentrations are in good agreement with ARPES data from Bostwick *et.al.* [77] but without including phonon effects, contrary to the interpretation of the experimental data [77]. The nature of the undoped and doped graphene has been as well discussed theoretically in terms of the behavior of the imaginary part of the self-energy [82]: a Fermi liquid behavior is found for doped graphene while the zero doping case exhibits a quasiparticle lifetime linear and a zero renormalization factor indicating that, close to Dirac point, undoped graphene behaves as marginal Fermi liquid in agreement with previous theretical work[49].

By evaluating exchange and random-phase-approximation (RPA) correlation energies, an enhancement of the quasiparticle velocities near the Dirac point is found in lightly doped graphene described by the massless Dirac equation taking into account the eigenstates chirality [83].

In this chapter, we calculate the corrections induced by the electron-electron interaction on the electronic band structure and on the Fermi surface shape of

graphene.The Fermi surface is one of the key features needed to understand the physical properties of a material and its shape provides important information. On the other hand, due to the 2D character of graphene electronic interaction should be important. We consider the symmetry of the honeycomb lattice in order to investigate doped graphene and possible effects in the trigonal warping topology of the Fermi surface. We calculate first the self-energy at the Hartree-Fock level and besides the renormalization of the band velocities, a deformation of the Fermi surface is found at this level that tends to contrarest the trigonal warping. When beyond Hartree-Fock corrections are included, the self-energy deforms the Fermi surface shape in an anisotropic way.

The paper is organized as follows. In section II the model is presented and we explain the calculation of the self-energies. Section III presents the results of the calculation and Section IV contains a discussion of the results compared to experimental data and to other theoretical results and the main conclusions of the work.

4.3 The method

4.3.1 The model for the graphene layer

Graphene is an atomic layer of carbon atoms arranged in a hoenycomb lattice with two atoms per unit cell as shown in Fig.4.1(a). The distance between nearest neigbor atoms is $a = 1.42$ Å, $\vec{a}_1$ and $\vec{a}_2$ are the primitive lattice vectors. The Brilouin zone (BZ) is an hexagon depicted in Fig.4.1(b). We adopt the π-band tight-binding model with only nearest-neigbor hopping[72], since it captures the main physics of the system as probed by more realistic models and by experimental results.

The Hamiltoniam kinetic term will be

$$\mathcal{H}_{kin}(\vec{\mathbf{k}}) = t \begin{pmatrix} 0 & g(\vec{\mathbf{k}}) \\ g^*(\vec{\mathbf{k}}) & 0 \end{pmatrix} \tag{4.1}$$

where $t = 2.82eV$ is the hopping parameter and the function $g(\vec{\mathbf{k}})$

$$g(\vec{\mathbf{k}}) = -\left(e^{-ik_y a} + 2e^{ik_y a/2} \cos\left(\frac{\sqrt{3}}{2} k_x a \right) \right) \tag{4.2}$$

By diagonalizing Eq.(4.1) the dipersion relation $\epsilon^0_{c,v}(\vec{\mathbf{k}}) = \pm t|g(\vec{\mathbf{k}})|$ is obtained

$$\epsilon^0_{c,v}(\vec{\mathbf{k}}) = \pm t \sqrt{1 + 4\cos\left(\frac{3}{2} a k_y\right)\cos\left(\frac{\sqrt{3}}{2} a k_x\right) + 4\cos^2\left(\frac{\sqrt{3}}{2} a k_x\right)} \tag{4.3}$$

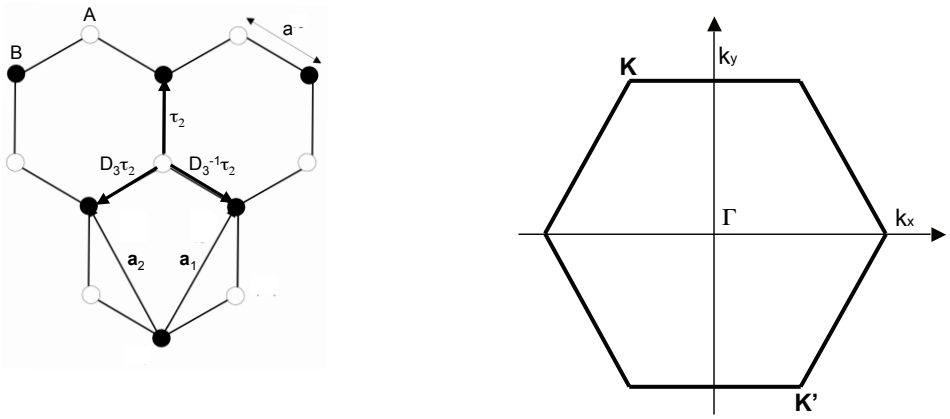

(a) (b)

Figure 4.1: (a) Schematic representation of the graphene honeycomb lattice, with two atoms (solid and empty circles) per unit cell. The basic vectors $\vec{\mathbf{a}}_1$ and $\vec{\mathbf{a}}_2$ of the lattice are shown. (b) First Brillouin zone corresponding to the honeycomb lattice.

-(+)sign corresponds to valence (conduction) band. The two bands are degenerated at the six corners of the BZ, **K** points. The corresponding Bloch wave functions are

$$\Psi_{\vec{\mathbf{k}};c,v}(\vec{\mathbf{r}}) = \frac{1}{\sqrt{2}}\left(U_{1\vec{\mathbf{k}}}(\vec{\mathbf{r}}) \pm \frac{g^*(\vec{\mathbf{k}})}{|g(\vec{\mathbf{k}})|}U_{2\vec{\mathbf{k}}}(\vec{\mathbf{r}})\right) \tag{4.4}$$

The tight-binding functions are built from the atomic $2p$ orbitals $\phi_z(\vec{\mathbf{r}})$ (see for example Ref.[84])

$$U_{i\vec{\mathbf{k}}}(\vec{\mathbf{r}}) = \sqrt{\frac{A}{S}}\sum_{\vec{\rho}_n} e^{\imath\vec{\mathbf{k}}\cdot(\vec{\rho}_n+\vec{\tau}_i)}\phi_z(\vec{\mathbf{r}}-\vec{\rho}_n-\vec{\tau}_i) \tag{4.5}$$

where in the normalization factor, A and S stands for the areas of the unit cell and the crystal respectively, $\vec{\rho}_n = n_1\vec{\mathbf{a}}_1 + n_2\vec{\mathbf{a}}_2$ is the lattice vector, and $\vec{\tau}_{1,2}$ define the atom position in a unit cell. We use $\vec{\tau}_1 = 0$ and $\vec{\tau}_2 = \frac{1}{3}(\vec{\mathbf{a}}_1 + \vec{\mathbf{a}}_2) = a\widehat{\mathbf{u}}_y$ (see Fig.4.1(a)). At half-filling (undoped graphene) the Fermi energy lies at the common point of the two bands (we take this energy as our zero energy) and the Fermi surface (FS) is formed by six points at the six BZ corners, as can be observed in Fig.4.1(b) where the constant energy contours for the 2D dispersion relation are depicted. These six points (only two of them are inequivalent) are known as Dirac points because around them, by a long-wavelength expansion, the kinetic energy term of the Hamiltoniam can be approximated by the 2D Dirac equation

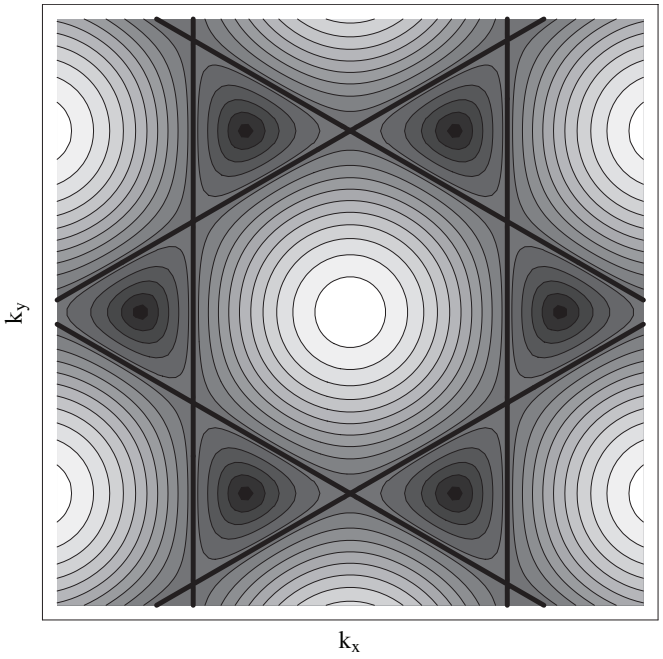

Figure 4.2: Constant energy contours obtained with Eq.(4.3) in the 2D graphene BZ. The thick black lines corresponds to the Van Hove filling.

for massless particles $H_D = v_F(\sigma_x k_x + \sigma_y k_y)$. This Hamiltonian gives the linear dispersion relation for the bands (conical shaped bands) and the density of states vanishes linearly with E. The low-energy physics of graphene is described by this Hamiltonian in the closeness of **K**. Upon doping lightly , following the constant energy maps shown in Fig.4.1(b), the FS points developped into circles and with further doping they take the rounded triangular shapes. When the doping is such that the chemical potential μ equals the hopping integral value, 2.82eV, the FS has the perfect straight-sided triangles and the Van Hove singularity (VHS) is reached. The presence of this VHS in graphene has been experimentaly confirmed by ARPES[78]. The electron interaction term will be

$$\mathcal{H}_{int}(\vec{\mathbf{r}}) = e_0^2 \begin{pmatrix} \frac{1}{|\vec{\mathbf{r}}_{AA}|} & \frac{1}{|\vec{\mathbf{r}}_{AB}|} \\ \frac{1}{|\vec{\mathbf{r}}_{BA}|} & \frac{1}{|\vec{\mathbf{r}}_{BB}|} \end{pmatrix} \tag{4.6}$$

where $\vec{\mathbf{r}} = \vec{\mathbf{r}}_{AB}$ connects an atom of the A sublattice with one of the B sublattice and so forth. In the momentum space, $V(\vec{\mathbf{q}}) = 2\pi e^2/\epsilon_0 q$, with ϵ_0 being the dielectric constant. The Fourier transformation in 2D gives a $1/q$ dependence and the electron-electron scattering is stronger than in 3D where the Fourier transformation gives the $1/q^2$ dependence. We will consider the long-range Coulomb interaction, the short-range nearest neighbor Coulomb repulsion and finally we analyze the corrections due to a Hubbard on-site interaction. We will limit to the

weak-coupling regime as it is generaly accepted for graphene.

4.3.2 Calculation of the self-energy

First-order pertubation

We calculate first the exchange self-energy contribution, that corresponds to the diagram shown in Fig.4.3(a), one-loop or Fock diagram. The corresponding self-energy have the form:

$$\Sigma^x_\lambda(\vec{\mathbf{k}}, i\omega_n) = -\sum_{\lambda'=c,v}\sum_{\vec{\mathbf{q}}}\frac{1}{\beta}\sum_{i\nu_n} G^0_{\lambda'}(\vec{\mathbf{k}}+\vec{\mathbf{q}}, i\omega_n + i\nu_n) v_{\lambda\lambda'}(\vec{\mathbf{k}}, \vec{\mathbf{k}}+\vec{\mathbf{q}}) \tag{4.7}$$

where $G^0_\lambda(\vec{\mathbf{k}})$ is the bare single-particle Green function and $v_{\lambda\lambda'}(\vec{\mathbf{k}}, \vec{\mathbf{k}}+\vec{\mathbf{q}})$ are the Coulomb interaction matrix elements, that for the exchange diagram reads

$$\begin{aligned} v_{\lambda,\lambda'}(\vec{\mathbf{k}}, \vec{\mathbf{k}}+\vec{\mathbf{q}}) &= \int d\vec{\mathbf{r}}_1 \int d\vec{\mathbf{r}} \langle \Psi_{\vec{\mathbf{k}},\lambda}(\vec{\mathbf{r}}_1)| \langle \Psi_{\vec{\mathbf{k}}+\vec{\mathbf{q}},\lambda'}(\vec{\mathbf{r}}_1 - \vec{\mathbf{r}})| \frac{e_0^2}{r} |\Psi_{\vec{\mathbf{k}},\lambda}(\vec{\mathbf{r}}_1 - \vec{\mathbf{r}})\rangle |\Psi_{\vec{\mathbf{k}}+\vec{\mathbf{q}},\lambda'}(\vec{\mathbf{r}}_1)\rangle \\ &= V(\vec{\mathbf{q}}) F_{\lambda\lambda'}(\vec{\mathbf{k}}, \vec{\mathbf{k}}+\vec{\mathbf{q}}) \end{aligned} \tag{4.8}$$

where $V(\vec{\mathbf{q}}) = \int d\vec{\mathbf{r}} \frac{e_0^2}{r} e^{\prime \vec{\mathbf{q}}\cdot\vec{\mathbf{r}}}$ and $F_{\lambda\lambda'}(\vec{\mathbf{k}}, \vec{\mathbf{k}}')$ arises from the overlap of the wave functions obtained by diagonalizing the Hamiltonian[84, 85, 86],

$$\begin{aligned} F_{\lambda\lambda'}(\vec{\mathbf{k}}, \vec{\mathbf{k}}+\vec{\mathbf{q}}) &= \int d\vec{\mathbf{r}}_1 |\langle \Psi_{\vec{\mathbf{k}},\lambda}(\vec{\mathbf{r}}_1)| \Psi_{\vec{\mathbf{k}}+\vec{\mathbf{q}},\lambda'}(\vec{\mathbf{r}}_1)\rangle|^2 \\ &= \frac{1}{4} I^2(|\vec{\mathbf{q}}|) \left| 1 + \lambda\lambda' \frac{g(\vec{\mathbf{k}}) g^*(\vec{\mathbf{k}}+\vec{\mathbf{q}})}{|g(\vec{\mathbf{k}}) g(\vec{\mathbf{k}}+\vec{\mathbf{q}})|} \right|^2 \end{aligned} \tag{4.9}$$

Therefore the correct symmetry of the lattice is included in $v_{\lambda\lambda'}(\vec{\mathbf{k}}, \vec{\mathbf{k}}+\vec{\mathbf{q}})$. $I(\vec{\mathbf{q}})$ comes from the matrix elements that contain the $2p$ wave function of carbon atoms $\phi_z(r)$ and can be approximated by (see Ref.[85])

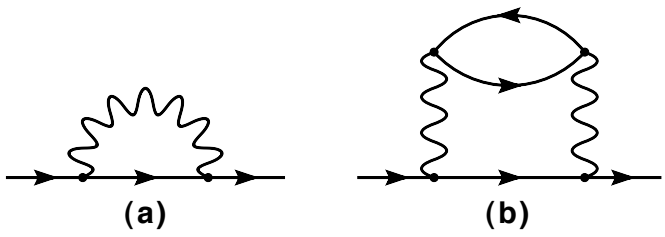

Figure 4.3: (a) Exchange diagram. (b) Two loop diagram.

$$I(\vec{\mathbf{q}}) = \left(1 + \left(\frac{qa_0}{Z}\right)^2\right)^{-3} \simeq \left(1 + \frac{q^2}{36}\right)^{-3} \tag{4.10}$$

where a_0 is the Bohr radius and Z is an effective core charge that is usually approximated by $Z \simeq 3.18$. This is well approximated by the limit $I(\vec{\mathbf{q}}) = 1$. Considering the $T = 0$ limit after performing the Matsubara sum we can write

$$\Sigma^x_\lambda(\vec{\mathbf{k}}) = -\sum_{\lambda'=c,v} \int_{BZ} \frac{d\vec{\mathbf{q}}}{(2\pi)^2} V(\vec{\mathbf{q}}) F_{\lambda,\lambda'}(\vec{\mathbf{k}}, \vec{\mathbf{k}} + \vec{\mathbf{q}}) \Theta(\mu - \epsilon^0_{\lambda'}(\vec{\mathbf{k}} + \vec{\mathbf{q}})) \tag{4.11}$$

where Θ is the Heaviside unit step function. The calculation requires a momentum integration over the first BZ and the calculation of the $F_{\lambda\lambda'}$ matrix elements corresponding to intraband ($\lambda = \lambda' = c$ and $\lambda = \lambda' = v$) and interband ($\lambda = c$ and $\lambda' = v$) excitations. We consider the Coulomb correlation $V(\vec{\mathbf{q}})$ to be long-range in the center of the BZ, a small region around Γ, and short-range, nearest-neighbor interaction, in the rest of the BZ. Finally, the correction of the dispersion relation due to the interactions will be given by:

$$\epsilon_\lambda(\vec{\mathbf{k}}) = \epsilon^0_\lambda(\vec{\mathbf{k}}) + \Sigma^x_\lambda(\vec{\mathbf{k}}) \tag{4.12}$$

Second-order pertubation theory

In order to study the effects induced by local interactions we compute the two-loop self-energy diagram shown in Fig.4.3(b). This two-loop diagram modifies the FS topology through its $\vec{\mathbf{k}}$ dependence and change the quasiparticle weight through its ω dependence. We follow the method explained in Chapter3 to study the interplay between the electron correlation and the FS topology. For a given doping, a concrete value of μ, we have a FS shape which changes from circles to triangles with the filling of the bands.

The interacting FS can be calculated as the solution of the equation:

$$\mu - \epsilon_\lambda(\vec{\mathbf{k}}) - \mathrm{Re}\Sigma^{(2)}_\lambda(\vec{\mathbf{k}}, \omega = 0) = 0 \tag{4.13}$$

where $\mathrm{Re}\Sigma^{(2)}_\lambda(\vec{\mathbf{k}}, \omega)$ is the real part of the self-energy of a λ band electron with momentum $\vec{\mathbf{k}}$.

As explained in [25], the real part of the two-loop self energy at zero frequency, corresponding to the diagram shown in Fig.4.3(b) can be computed from the equation

$$\Sigma_\lambda(\vec{\mathbf{k}}, \omega = 0) = -\frac{3}{32} \frac{U^2 a^4}{\sqrt{2}\pi^3} \frac{\Lambda^2 sgn(b(\vec{\mathbf{k}}, \lambda))}{v^3_F(\vec{\mathbf{k}}, \lambda) b(\vec{\mathbf{k}}, \lambda)} \tag{4.14}$$

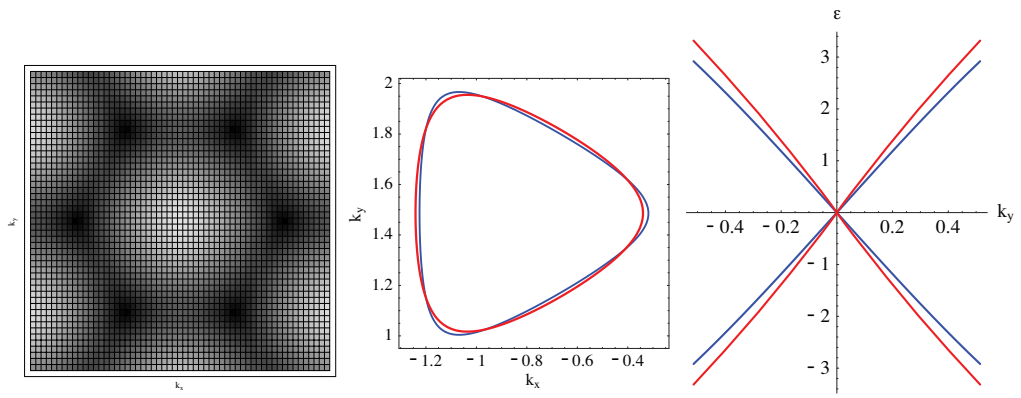

(a) (b) (c)

Figure 4.4: (a) Density plot of the self-energy obtained from Eq.(4.11). The dark regions are the ones with stronger correction. (b) Non-interacting (blue) and interacting (red) Fermi lines around the **K** point for a doped graphene layer with $\mu \approx 2.4eV$. (e) Bare (blue) and renormalized (red) bands for $\mu = E_D = 0$. We have adjusted the chemical potential of the renormalized band (by $\delta\mu \simeq 0.85eV$) to have the Fermi energy at the Dirac point.

For consistency, we consider the Hubbard interaction $U \lesssim \Lambda$, as well below the energy cutoff, which a stated above is not unresonable for graphene, U being a local interaction in the real space.

4.4 Results and discussion.

4.4.1 Corrections induced by the exchange self-energy

We now explain the results obtained from the exchange energy obtained from the formula Eq.(4.11) . As stated above, in the momentum integration we consider the long-range Coulomb interaction in a small region of the BZ, around Γ and the nearest neighbor interaction in the rest of the BZ. In Fig.4.4(a) a density plot of the self-energy is shown in the BZ. The self-energy gives the stronger corrections at the boundary lines of the BZ, keeping the same symmetry of the band structure. Therefore, the corrections to the FS topology are small, although not negligible, as can be observed in Fig.4.4(b) for a doping corresponding to $\mu = 2.4eV$. The self-energy corrections enhance the curvature of the triangle sides and round the vertex.

For a doping corresponding to a value of the chemical potential of $\mu = 2.82eV$, the FS is close to the VHS. The flatness of the bands in this region gives the almost perfect triangular shape of the surface. A correction can be obseved just at the

vertex of the triangle which, upon the correction, are rounded. The self-energy effects are more noticeable in the band slope, as can be observed in Fig.4.4(c) where the dispersion relation, calculated without and including the self-energy corrections, are shown. The exchange self-energy enhances the velocity of the bands renormalizing the kinetic energy. The enhancement of the velocity has been obtained by other calculations [87]. The increase of the quasiparticle velocity in graphene at low doping has been attributed to the loss in exchange energy when crossing the Dirac point switching the quasiparticle chirality[83] by evaluating graphene exchange and correlation energy. By calculating the imaginary part of the self-energy within the on-shell approximation at $T = 0$ [82] a renormalization of the velocity at E_F is as well reported. Following this work, doped graphene does not show deviation from the Fermi liquid behavior, while at zero doping graphene presents a behavior compatible with the marginal Fermi liquid description, with the linear energy dependence of the quasiparticle lifetime [82, 49]. The exchange energy effects on the FS topology turn out to be small for both, doped and undoped graphene. This result agree with the ARPES measurements which report the trigonal warping FS shape [74, 78] for lightly doped graphene.

The presence of the strong VHS, experimentaly confirmed [78] reveals some similarity to the cuprates [88]. The similarities between graphene and the cuprates has been already remarked by [79] not only because of the VHS but as well because of the similarity between the band structure of graphite and that of the nodal quasiparticles in the cuprate superconductors. The existence of an extended VHS as probed but the flatness of the bands in both graphene and cuprates is important because its effects on the divergences of the density of states. The VHS is related with the interactions which can be enhanced in its proximity and could increase in both, the cuprates and the graphite intercalated compounds, the superconductivity critical temperature [78] when E_F is placed at the VHS.

4.4.2 Corrections induced by a local interaction

We analyze the corrections induced by a local interaction in the real space, i.e. momentum independent. The self-energy is computed from Eq.(4.14) which gives the second order perturbation theory renormalization of the Green's function. As explained in ref.[25] this electron-electron interaction self-energy depends on local features of the non-interacting FS, as the Fermi velocity and the curvature at the Fermi level. We limit ourselves to the weak coupling regime as seems generally accepted for graphene, and where the perturbation approach is justified. The density plot of the self-energy is represented in Fig.4.5(a) around a **K** point. The density is $\vec{\mathbf{k}}$ dependend, although there is a hint of the symmetry of the underlying lattice.

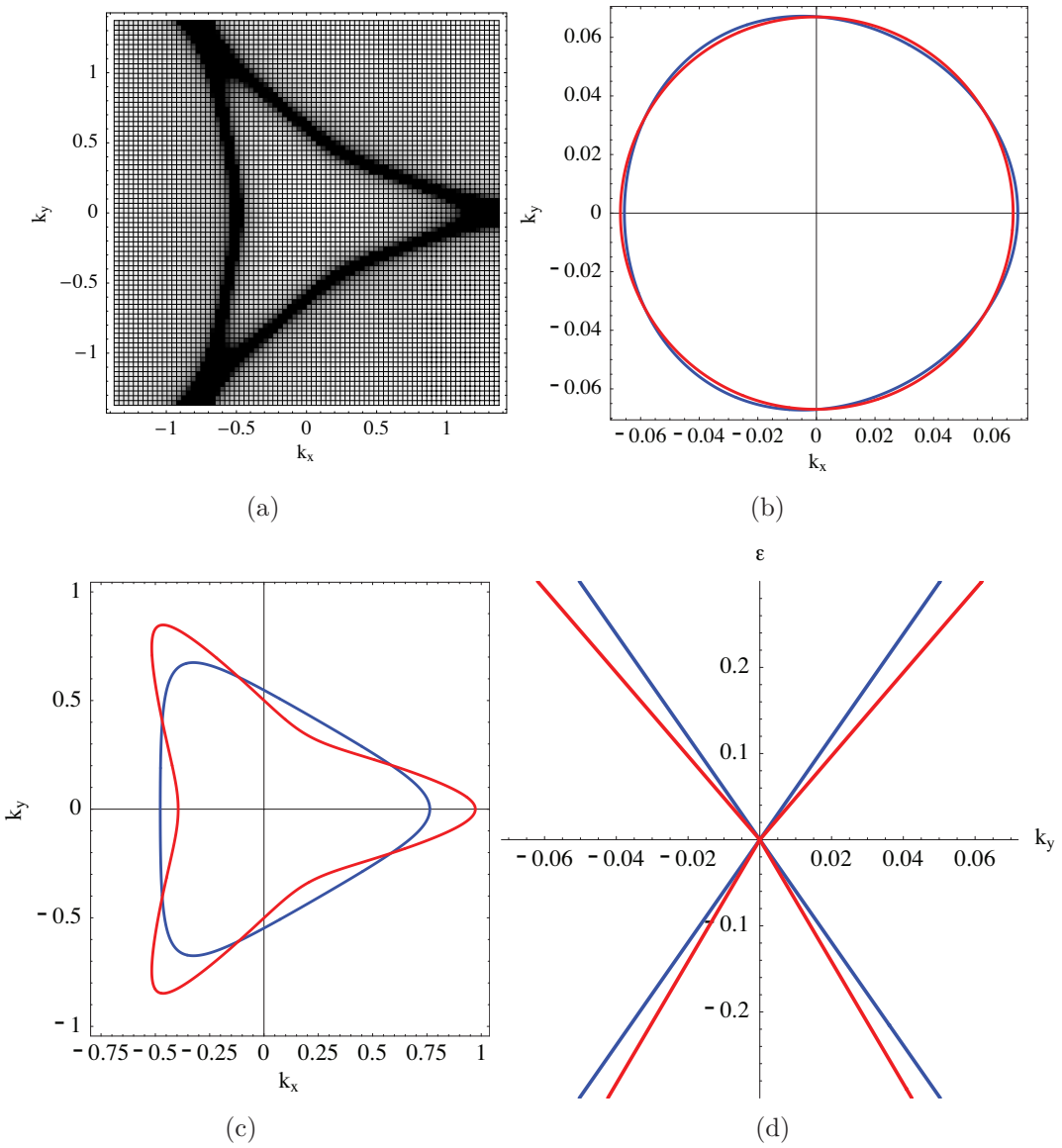

Figure 4.5: (a) Density plot of the self-energy obtained around the **K** point according to Eq.(4.14). The dark regions are the ones with stronger correction. We have set $U = 3t$ and $\Lambda = 9t$. (b) Non-interacting (blue) and interacting (red) Fermi lines around the **K** point for a doped graphene layer with $\mu \approx 0.2eV$. (c) Same as (b) but for $\mu \approx 2.4eV$. Notice the different scales of the coordinate axis. (d) Bare (blue) and renormalized (red) bands and particle-hole symmetry breaking due to the different renormalization of the Fermi velocity in the conduction and valence bands.

At low doping level with the FS of circular shape, a small but appreciable correction is found the correction differs dependending on $\vec{\mathbf{k}}$, as shown in Fig.4.5(b). Increasing the doping level the FS adops the round triangular shape. At this level the effects of the self-energy are noticeable, and present a strong anisotropy. The depormation of the Fermi surface is maximum along the KM direction of the BZ, as can be observed in Fig.4.5(c). The topology of the FS is changed by the correction adopting an almost concave shape, the underlying hexagonal symmetry ($2\pi/3$ rotation around **K** point) is preserved. Surprising enough this deformation, induced by pure electron-electron interaction self-energy, presents a strong similarity with the deformation found by ARPES [78] in graphene. On Fig.3 (a) from ref.[78] the Fermi contours derived from curvefitting the data obtained at various dopings are plotted. The anisotropic deformation of the Fermi contours are attributted to electron-phonon coupling to the graphene in-plane optical vibrations. The electron-phonon coupling constant $\lambda_\pi(\vec{\mathbf{k}})$ extracted from experimental data shows a strong anisotropy (around 5:1 ratio at highest doping) and a much higher strength than would be expected for π-bands and optical phonons in graphene. It is argue that the abrutness of the kink (change of the band velocity) and the broadening of the bands suggest a strong mass renormalization by electron-phonon coupling. The divergence of $\lambda_\pi(\vec{\mathbf{k}})$ along the KM direction is explained as due to the VHS along the KMK boundary line of the BZ, reached upon further doping. In our calculated self-energy the proximity to the VHS enhances its correction and it reaches its maximum at the Van Hove band filling where the E_F reaches the VHS, considering only a weak local electron interaction. Therefore, at low doping, when the FS lies very close to the **K** point the corrections to the FS shape are very small since the circular line lies far fom the VHS location, while a higher doping the Fermi line lies close to the VHS, specially the vertex of the triangle and therefore the deformation is higher in this direction. In [78] by studying the evolution of the coupling parameter $\lambda_\pi(k)$ with the doping level it is found that while the minimum coupling strength grows only slowly with doping, the maximum coupling parameter diverges as the corresponding segment of the Fermi contour approaches the VHS at the M point. As explained in [25, 89] the corrections induced by the self-energy calculated from Eq.(4.14) depend on local features of the non-interacting FS as the Fermi velocity v_F and the curvature of the Fermi line. The main self-energy effects in the square lattice are found to occur when the FS reaches the border of the BZ because there the real part of the self-energy presents pronounced dips close to the saddle points because the v_F vanishes at the VHS [25], as it is found here. (See Fig.3.6 for the case of a square lattice).

It should be notice that the self-energy correction calculated by second-order pertubation theory is always negative. The renormalization of the velocity of

the bands will have opposite effects due to the sign: the slope of the valence band will increase while that of the conduction band will decrease as shown in Fig.5(d). Therefore the renormalized bands are misaligned above and below the Dirac crossing point. In Ref.[90] it is observed that the ARPES measured bands of as-prepared graphene above and below the Dirac point (E_D) are misaligned, the projections of the π-states below E_D do not pass through the π^*-states above E_D, and the misalignement is attributed to the many-body interactions [90].

4.5 Conclusions

We have calculated the corrections induced by electron-electron interactions in the band structure of graphene. We limit ourselves to the weak coupling regime, as it is generally assumed to be appropriate for graphene. At first order and zero temperature, the exchange self-energy induces a deformation which contrarest the trigonal warping of the Fermi surface of doped graphene. The self-energy corrections round the tringle shape. At low doping, the correction to the circular Fermi surface are small. The Fermi velocity is enhanced.

The self-energy calculated by second-order perturbation theory, considering a local Hubbard interaction, shows a strong k-dependence, therefore the deformation induced in the FS topology is anisotropic. The deformation is highest in the KM direction of the BZ, the maximum value is reached at the Van Hove filling when the Fermi level is very close to the VHS. These results are in very good agreement with those experimentally obtained by McChesney *et al.* in [78]. The anisotropic deformation found by ARPES is attributed to a coupling to the graphene in-plane optical phonons. In Fig.4.5 the density of the self-energy and the Fermi surfaces at two different doping levels have been represented around the corner of the BZ. It should be notice that the **K'** counterpart has to be considered, (see Fig.4.2 where the hole hexagonal BZ is represented) in order to include all the possible scattering channels. Electron correlation renormalize the Fermi velocity, but due to the negative sign of the second-order perturbation self-energy, the correction to the valence band velocity is opposite to that of the conduction band. Our results highlight the importance of electron correlation in the low-energy physics of graphene.

Chapter 5

Interplay of metamagnetic and structural transitions in $Ca_{2-x}Sr_xRuO_4$.

5.1 Abstract

Metamagnetism in layered ruthenates has been interpreted as a novel kind of quantum critical behavior. Under the application of an external field, $Ca_{2-x}Sr_xRuO_4$ undergoes a metamagnetic transition accompanied by a first order structural transition. In this chapter we present a mean field study for a microscopic model that gives a natural explanation of some of the features of this system. The phase diagram calculated is equivalent to the experimental T-x phase diagram. The presented model also gives a good basis to discuss the critical metamagnetic behavior measured in the system.

5.2 Introduction

Calcium-doped single-layer strontium ruthenate exhibits a very rich phase diagram spanning the antiferromagnetic Mott insulator Ca_2RuO_4 at x=0 to the unconventional spin-triplet superconductor Sr_2RuO_4 at x=2. This variety of ground states is surprising since only the atomic radius of the sites of Ca/Sr atoms varies througout the compounds when x varies. $Ca_{2-x}Sr_xRuO_4$ has the perovskite structure shown in Figure5-1, similar to that of copper oxides. The transition-metal ruthenium atoms form the RuO_4 oxide planes and the RuO_6 octahedra. Ru atoms are surrounded by six oxygen ions O^{2-} and R wave functions $d_{x^2-y^2}$ and $d_{3z^2-r^2}$, called e_g orbitals, pointing toward the O^{2-} ions have haigher energy in comparison with the d_{xy}, d_{yz}, and d_{zy}, called t_{2g} orbitals, point-

ing between them. When electrons are placed into these orbitals, the Hund's rule determines the ground state. In these transition-metal oxides the orbital (the shape of the electron cloud in the crystal) degree of freedom of the electron has to be taken into accoont, besides the charge and spin degrees of freedom [91]. The anisotropic shape of the $d-$orbitals together with the Coulomb repulsion between electrons would play a main role in the understanding of some unconventional properties. The orbital physics has to be considered to analyze phenomena such as the high-critical temperature superconductivity from the cuprates with a d-wave order parameter, the colossal magnetoresistance, a very large decrease of the resistance upon application of an external magnetic field, which occurs in manganites, manganese oxides (explained by orbital ordering and correlation) and the metal-insulator transition upon doping.

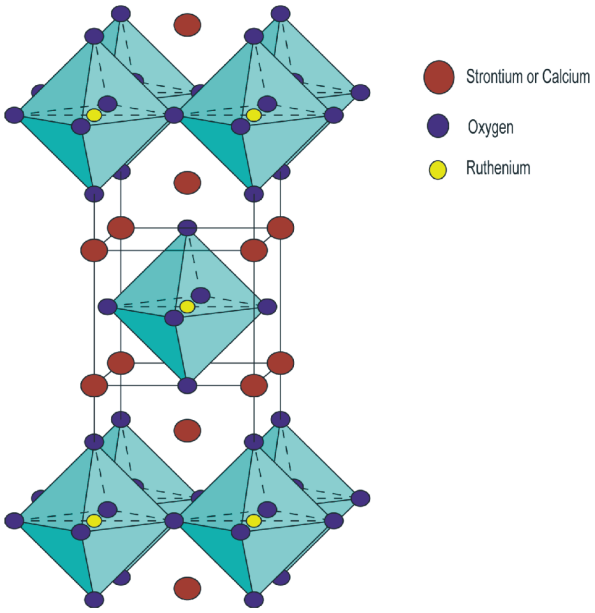

Figure 5.1: Layered perovskite structure of Sr_2RuO_4. This is the undistorted tetragonal structure with space group $I4/mmm$. When strontium is substituted for calcium, the distortins change the symmetry group.

The Mott insulating satate appears in the phase diagram of these materials. Following band theory, the insulating state occurs when all bands of the solid are full or empty, and conduction is blocked by the Pauli exclusion principle, because the orbitals are filled. In a Mott insulator the conduction is blocked by Coulomb repulsion, when it is strong enough to avoid the electron hopping from an atom to the next. In this Mott insulating state the spin and orbital degrees of freedom of the electrons are important. When carriers are doped into the Mott insulator

its new state will depend on the spin and on the orbital they enter.

$Ca_{2-x}Sr_xRuO_4$ is a multiorbital system [92] and a fundamental issue is whether Mott transitions take place in sequence or simultaneously for all bands by the chemical substitution. The competition between the intra- and inter-orbital interactions, as well as the Hund's coupling, determines the nature of the Mott transition. The phase diagram of $Ca_{2-x}Sr_xRuO_4$ is very interesting because, due to the smaller ionic radius of the Ca compared to that of the Sr atom, structural changes occur and the Mott transition may be tuned by structural cahanges only. The phase transitions are characterized by rotations or tilts of the RuO_4- octahedra as shown in Figure5.2. These structural deformations have strong impact on the electronic band widths.

At some doping levels, upon applying a magnetic field at low temperature, on $Ca_{2-x}Sr_xRuO_4$ samples, a metamagnetic transition is induced, with a step-like increase of the manetig moment of Ru atoms. This metamagnetic transitionresembles that observed in the double-layer ruthenate $Sr_3Ru_2O_7$, in particular both exhibit the octahedra rotation around $c - axis$.

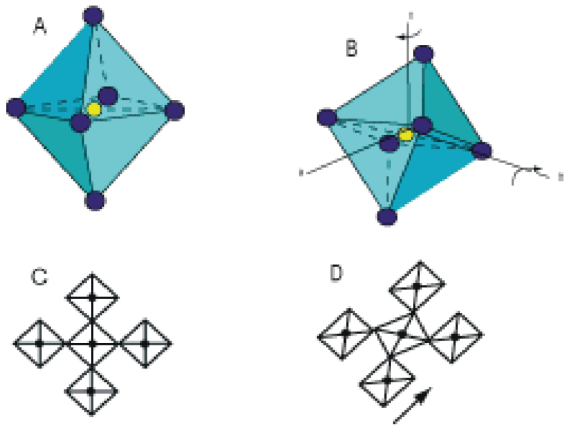

Figure 5.2: RuO_6 octahedra. A: Undistorted octahedron of $Sr_2RuO_4$with an elongated c-axis. B: Tilted and rotated octahedron of Ca_2RuO_4, with a shortened c-axis. C: Top view of tetragonal structure. D: Top view of the orthorombic distorted structure with the arrow indicating the elongation along the b axis.

$Ca_{2-x}Sr_xRuO_4$ is known to be a system with strong interplay of magnetic and orbital degrees of freedom[93]. In particular, recent magnetostriction experiments[94, 95] have shown that the metamagnetic transition in this material is accompanied by a structural transition in the symmetry of its lattice. This interplay of order parameters originating from different degrees of freedom of electrons can be found in a number of physical problems. In particular, the mutual influence of spin and orbital degrees of freedom plays an important role in the behavior of manganites,

ruthenates or titanates[96].

For the case of the present study, the competition between orbital and magnetic orders can be seen, for zero external magnetic field, in the T-x phase diagram shown in Fig.[5.3]. Before to describe in detail the evolution of $Ca_{2-x}Sr_xRuO_4$ with the strontium concentration x, it is worth noting that both, Sr^{2+} and Ca^{2+} are isovalent ions so that the substitution of one by the other does not change the number of conductance electrons. Sr_2RuO_4 is a good metal and the *a priori* expected change due to the substitution of Sr by Ca should be increasing metallicity, in the sense that we are doping with a smaller ion what should imply a widening of the band. This is not so: Ca_2RuO_4 behaves as a Mott insulator, and all the evolution between these end members builds a very rich phase diagram where different structural and magnetic phases compete each other (Fig.[5.3]).

A metamagnetic transition is observed in region II of the phase diagram at low temperatures[97, 94, 95]. In general, a metamagnetic transition can occur for a material which, under the application of an external field, it undergoes a first order transition to a phase with a non-zero ferromagnetic moment. This is experimentally observed by a very rapid increase of magnetization over a narrow region of applied magnetic field. As a result, the structural distortion of region II, reached upon cooling in zero field, can be inverted with the application of a high field at low temperature. Finally, in reference [95] the authors introduce the possibility for a metamagnetic *critical endpoint* (CEP) for $Ca_{1.8}Sr_{0.2}RuO_4$ at low temperatures, similarly to the quantum critical endpoint measured for $Sr_3Ru_2O_7$.

Among the rest of experimental results obtained for $Ca_{2-x}Sr_xRuO_4$ is specially surprising the $S = 1/2$ magnetic susceptibility measured for a large range of concentrations, $0.2 \lesssim x \lesssim 1.5$, contrary to the expected $S = 1$ spin according to the Hund's coupling [98]. This anomaly was the base for the treatment that Anisimov *et al.* [99] did on this system. They proposed a microscopic model where the γ band remains metallic, while the electrons in the $\{\alpha, \beta\}$ bands are localized. In this work we use a generalization of this model to study the effects of an external magnetic field on the system. In particular, by means of a mean field approximation, we find a structural transition from an undistorted to a distorted system. Starting from this and under the application of an external magnetic field, we find a first order magnetic transition accompanied by the restoring of the undistorted structure.

5.3 Electronic structure

We have pointed out in the previous section that Sr^{2+} and Ca^{2+} are isovalent ions so that the substitution of one by the other should not be expected to play much

of a role concerning the physical properties of the material. As we have seen in Chapter3, Sr_2RuO_4 is a good Fermi liquid. But surprisingly, the substitution of Sr by Ca breaks down this behavior: Ca_2RuO_4 is a Mott insulator and all the evolution between these end members builds a very rich phase diagram where different structural and magnetic phases compete each other, as we will see in the next section.

All the members of the $Ca_{2-x}Sr_xRuO_4$ family have the electronic configuration $\{Kr\}4d^4$. Due to a large crystal field and according to LDA results[99], Ru^{4+} ions are in the low-spin configuration t_{2g}. What it is different is the occupation of these orbitals in the two end members of the phase diagram: while for $x = 0$ we have an average occupation of two electrons in the d_{xy} orbital and the other two in the d_{yz} and d_{zx} orbitals, for $x = 2$ we have the fractional occupation of 4/3 in the d_{xy} band and 8/3 in the d_{yz}-d_{zx}-bands. For this doping $x = 2$ concentration, corresponding to Sr_2RuO_4, the system has a tetragonal symmetry with the RuO_6-octahedra slightly elongated along the c-axis. The splitting between the xy-orbitals and the degenerate $\{xz, yz\}$-orbitals is small. But the xy-orbitals π-hybridize with $2p$-orbitals of all 4 in-plane O-neighbors while the $xz(yz)$-orbitals π-hybridize only with the two O-neighbors along the $x(y)$-axis. As a result the xy-bandwidth is approximately twice the $\{xz, yz\}$ bandwidth. The LDA calculations (in agreement with the de Haas-van Alphen results) give three Fermi surface sheets, one with essentially xy and two with mixed $\{xz, yz\}$ character. The first one is usually called γ band while the others are labelled by α and β bands. It is important to notice that the γ band lies near a Van Hove singularity (which it is at approximately 50meV above the Fermi level). This singularity plays an important role for the magnetic instabilities that are associated to single and multi-layer ruthenates[66].

On the other hand, at the opposite part of the phase diagram we can find Ca_2RuO_4 for $x = 0$. For this concentration the structure undergoes a flattening of the RuO_6 octahedra with respect to the $x = 2$ case, accompanied by a rotation and tilting so that the Ru-O bond length is preserved but the Ru-Ru separation contracts. This makes the d_{xy}-orbital to lie lower in energy, what implies a change in the occupation of the bands, leading a completely full γ band what, together with the localization of the electrons in the d_{yz} and d_{zx} orbitals, make the system to be insulator. It is tempting to compare this system to the high-T_c cuprates, which have a similar perovskite structure with CuO_2 planes instead of RuO_2 planes like in the ruthenates. While the cuprates only have one band at the Fermi level, associated to the Cu-$d_{x^2-y^2}$-orbital, Sr_2RuO_4 has a triply degenerated t_{2g} bands. This orbital degree of freedom will play a crucial role in both, change in the magnetic properties as well as in the Mott transition for smaller x concentrations. The orbital occupation for intermediate concentrations, in particular near $x = 0.5$,

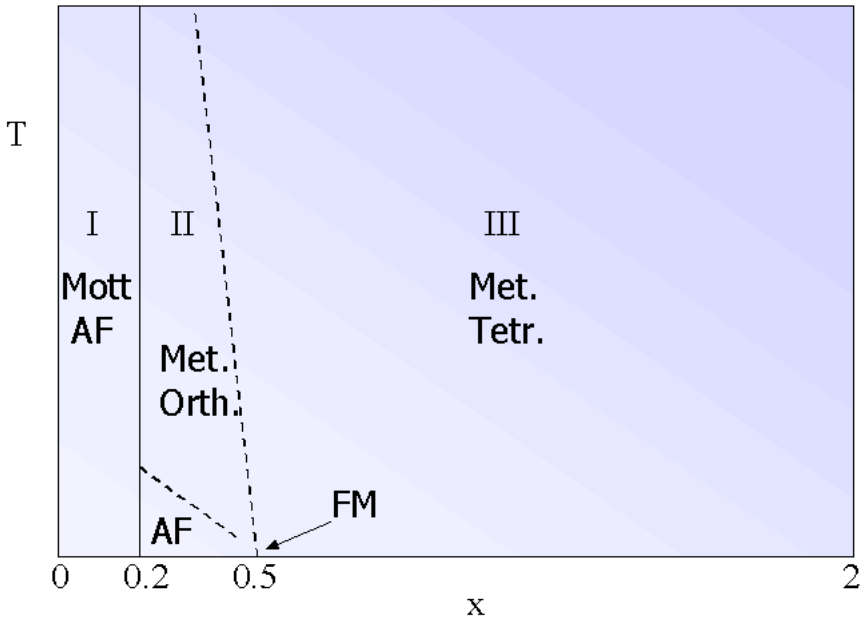

Figure 5.3: Sketch of the temperature-doping phase diagram of $Ca_{2-x}Sr_xRuO_4$. Region I corresponds to a Mott insulator with long range antiferromagnetic order. Region II is characterized by a metallic behavior with orthorombic lattice symmetry and antiferromagnetic correlations at low temperatures. Region III corresponds to a paramagnetic metal with tetragonal symmetry in the lattice. For $x \to 0.5$ there are strong ferromagnetic correlations at low temperatures.

will be discussed later.

5.4 $T - x$-phase diagram

In this section we briefly highlight the main features of the different regions included in the phase diagram of $Ca_{2-x}Sr_xRuO_4$, shown in Fig.[5.3]. It has two very different end members: for $x = 2$ we have the good Fermi liquid Sr_2RuO_4 and for $x = 0$, the antiferromagnetic Mott-insulator Ca_2RuO_4. Between them we find a complex phase diagram where we can distinguished three main regions:

- **Region-III** ($0.5 \leq x \leq 2$) In this zone we have a paramagnetic metallic system with **tetragonal** symmetry. For $x = 2$ we have Sr_2RuO_4 that is also superconductor below $T_c \sim 1.5K$. There is no orbital order and the occupation of the orbital is $(n_{(\alpha,\beta)}, n_\gamma) = (\frac{8}{3}, \frac{4}{3})$, giving a total spin of $S = 0$. For $0.5 \leq x \leq 1.5$ we have a **rotation** of the RuO_6 octahedra, although the symmetry still remains tetragonal. The conductivity is reduced by the

doping with Ca, and the susceptibility increases when we approach $x \to 0.5$, becoming a Curie-like susceptibility.

- **Region-II** $(0.2 \leq x \leq 0.5)$

  From region-III to region-II we have a structural phase transition, changing the symmetry of the system from tetragonal to **orthorhombic**. In this region, besides the rotation we have a tilting of the RuO_6 octahedra, which is the responsible for the reduction of the symmetry. These distortions lead to a reduction of the hybridization of the orbital and a corresponding narrowing of the bands, which enhance the correlation effects. As stated above, due to the smaller ionic radius of Ca compared to that of Sr, one would expect wider bands in the Ca-rich regions of the phase diagram. This is not so due to the distortion of the RuO_6 octahedra that accompanies this substitution of Sr by Ca.

  Therefore, these rotation and tilting lead to an elongation of the octahedra, making the d_{xy} orbital to lie higher in energy and favoring a transfer of charge from the γ to the α and β bands, one of the reasons why it was assumed that the occupation of the orbital in this region of the phase diagram is $(3, 1)$. On the other hand, the system has AFM order with total spin $S = \frac{1}{2}$. Here we find a ferro-orbital (FO) order with antiferromagnetic (AFM) spin correlations, that transform to antiferro-orbital (AFO) with ferromagnetic (FM) correlations for $x \to 0.5$. For low temperatures, the application of a magnetic field leads to metamagnetic transition and to a vanishing in the tilting of the RuO_6-octahedra, what would explain the several recent magnetostriction experiments on the material for $x = 0.2$ and $x = 0.5$[94, 95].

- **Region-I** $(0 \leq x \leq 0.2)$ In this region we find a Mott-insulator with a long-range AFM order below $100-150K$. It is found a clear first-order structural transition when we cross from region-II to region-I. The occupation here is $(2, 2)$, with a total spin of $S = 1$.

5.5 Experimental background

The most relevant experimental results that lead to the previous phase diagram are here described:

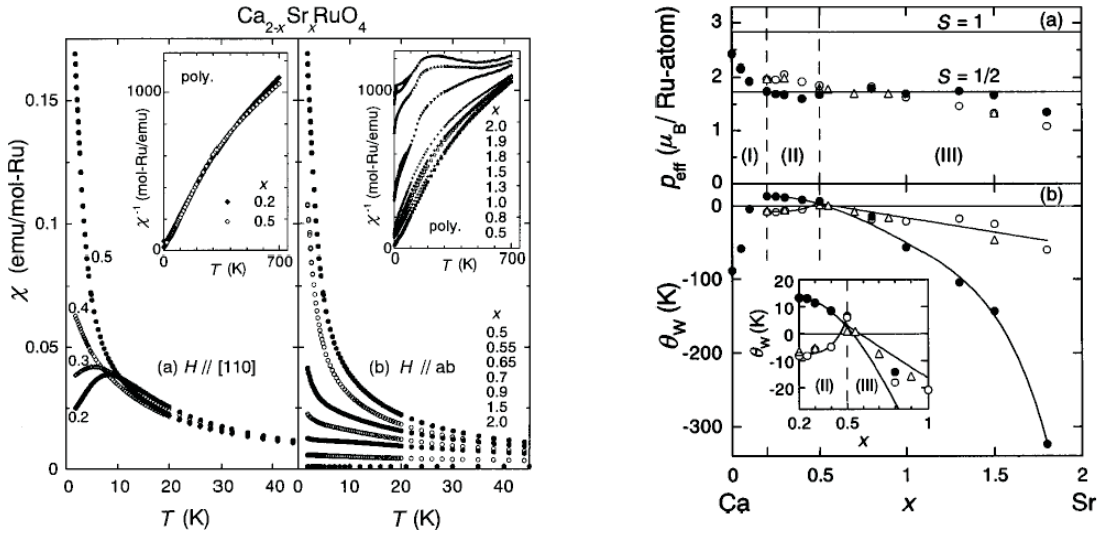

Figure 5.4: Left: temperature dependence of the magnetic susceptibility $\chi(T)$ for $Ca_{2-x}Sr_xRuO_4$. Right: Curie-Weiss parameters as a function of Sr concentration x in $Ca_{2-x}Sr_xRuO_4$. (Figures extracted from Ref.[98])

5.5.1 Susceptibility

In the left hand side of Fig.[5.4] we can see the experimental results for the temperature dependence of the in-plane susceptibility $\chi = M/H$ in region III (panel (a)) and II (panel (b)), where M and H are the magnetization and the applied magnetic field, respectively. All along these metallic regions, the $\chi(T)$ curves show a systematic variation with x. In order to clarify this evolution with x, a Curie-Weiss (CW) analysis of the data is carried out, that it is the typical analysis made over itinerant electron systems with spin fluctuations. They use the fitting expression

$$\chi = \chi_0 \frac{C}{T - \Theta_W} \tag{5.1}$$

where χ_0 is a temperature-independent term, C is the Curie constant, and Θ_W is the Weiss temperature. The effective Bohr magneton p_{eff}, which depends on the effective spin as $p_{eff} = 2\sqrt{S_{eff}(S_{eff}+1)}$, can be derived from the formula

$$C = \frac{N_A p_{eff}^2 \mu_B^2}{3k_B} \tag{5.2}$$

where N_A is the Avogadro's number, μ_B the Bohr magneton and k_B the Boltzman's constant.

As we saw in the previous section, the states at the Fermi level in Sr_2RuO_4 are mainly composed by the $4d - t_{2g}$ bands, so that the itinerant t_{2g} spins are respon-

sible for the dominating CW term in Eq.(5.1). The results of the fitting are shown in the right hand side of Fig.[5.4]. Let's first look into panel (b) where they show the results of the Weiss temperature as a function of x. We see that $\Theta_W \underset{x\to 0.5}{\longrightarrow} 0$. This means that for $x = 0.5$ we have a Curie-like susceptibility with a maximum at $T = 0$ as it can be seen in the left hand side of Fig.[5.4], where the peak in χ is found at zero temperature for concentrations approaching $x = 0.5$. For smaller x in region II (panel (a)) we see that the peak in the susceptibility moves towards larger temperatures. This is significative of antiferromagnetic correlations and the position of the peak set the Néel temperature. On the other hand, for higher x concentrations in region III (panel (b)) we see that the position of the peak is still at $T = 0$ but the values of χ decrease with x for a fixed temperature and eventually, the susceptibility becomes temperature-independent for high x, close to $x = 2$. This is a signal of Pauli paramagnetism in this region and consistent with the high values of Θ_W found for this zone. This can be seen in panel (b) of the right hand side of Fig.[5.4]. The inset shows also the change in the sign of the Weiss temperature for region II ($0.2 \leq x \leq 0.5$). Taking into account that positive values of Θ_W indicate the strength of ferromagnetic interactions and negative values of Θ_W indicate strength of antiferromagnetic interactions, we see that if $T > T_0$, where T_0 is the temperature that marks the structural phase transition from tetragonal to orthorombic, then $\Theta_W > 0$, pointing out that there are ferromagnetic correlations in the tetragonal phase, while if $T < T_0$ then $\Theta_W < 0$, what indicates antiferromagnetic interactions associated to the orthorombic phase. We can conclude that the change of sign in Θ_W points out a change in the magnetic coupling due to the structural transition.

Finally, in panel (a) we can see the results for the effective Bohr magneton p_{eff}. The two horizontal lines mark the values for p_{eff} that correspond to the effective spin values $S_{eff} = 1$ and $S_{eff} = 1/2$. The first anomaly that we can see here is that, contrary to the expected spin $S = 1$ associated to the Hund's coupling (see Fig.[5.5]) there is a large range of concentration $0.2 \lesssim x \lesssim 1.5$ where the fitting gives a spin of $S = 1/2$. The measured spin rises when one crosses towards the Mott insulating zone of the phase diagram, region III, and the $S = 1$ value is finally reached for $x = 0$ concentration.

In order to explain this spin $S = \frac{1}{2}$ in the susceptibility when we are in the $0.2 \lesssim x \lesssim 1.5$, we will assume all along this paper that the electron in the γ band remains metallic, while the hole in the $\{\alpha, \beta\}$ bands is localized[99].

5.5.2 Magnetization and magnetostriction.

The field dependence of the magnetization and magnetoresistance of $Ca_{2-x}Sr_xRuO_4$ can be found in Ref.[97]. Here the authors find a metamagnetic transition to a

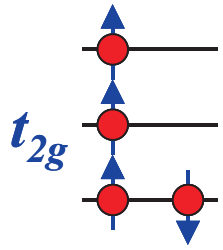

Figure 5.5: Expected S=1 configuration for the four electrons in the $4d$-t_{2g}-orbitals of Ru^{4+}. The e_g orbitals are empty.

highly polarized state, with a local moment of $S = 1/2$. These measurements are interestingly complemented by the magnetostriction experiments published in Ref.[94, 95], where the changes of the lattice constants as a function of the magnetic field for different temperatures in the region II of the phase diagram ($0.2 \leq x \leq 0.5$) are shown.

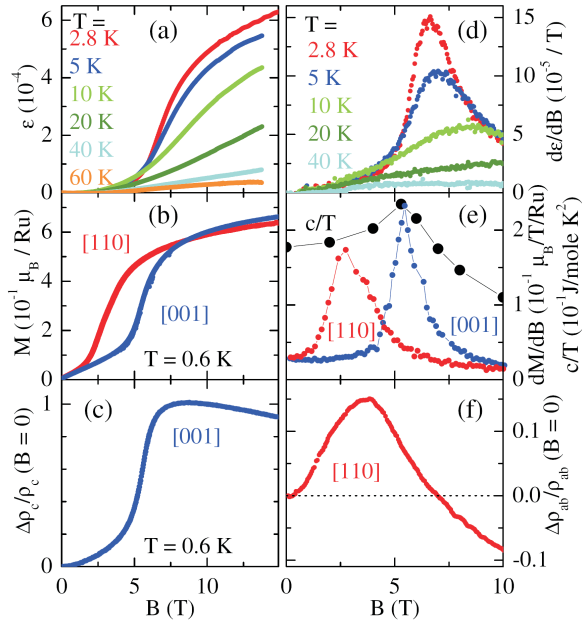

Figure 5.6: Magnetostriction (a) and magnetization (b) measurements for $x = 0.2$. (Figure extracted from Ref.[94]).

In Fig.[5.6](b) we can see the magnetization as a function of the applied field. The metamagnetic transition appears at different energy scales, depending on the orientation of the magnetic field ($H_{mm} = 5.7T$ for field applied along c and $H_{mm} = 2.0T$ for field perpendicular to c). We should remember that a metamagnetic transition can occur for a material which has an antiferromagnetic order

for zero external magnetic field, and which under the application of an external field, it undergoes a first order transition to a phase with a non-zero ferromagnetic moment. Even if the transitions seen in Fig.[5.6](b) do not look like a first order, because there is no a clear discontinuity in M for the critical field, this is due to the lack of homogeneity of the system. The spatial fluctuations in the crystal deformation, for example, would prevent this well defined jump in the magnetization at the transition field. The results show that when one crosses the transition into the high-field phase, there is an enhancement along the c direction, accompanied by a shrinking along both in-plane directions. Then, the application of a high field at low temperature can invert the structural distortion that occurs in region II upon cooling in zero field. This is, the structural change at the metameagnetic transition is directly related to the elongation of the RuO_6 octahedron. Finally, it is worth noting that the qualitative effects associated to the metamagnetic transition, namely the disappearance of the tilting of the RuO_6-octahedra, are independent of the magnetic field direction.

5.6 The model

In this work we assume that for doping concentrations x corresponding to regions II and the Ca-rich part of region III of the phase diagram the electrons occupying the α and β bands are localized due to strong electron-electron interaction while the half-filled γ band is assumed to remain itinerant and responsible for the metallicity of the material. This scenario, including an orbital-selective Mott transition (OSMT) in the α and β bands, was first proposed by Anisimov et al. in Ref.[99]. This is a very controversial issue [100, 92, 101] and it is still not clear to which extend this picture is applicable for $Ca_{2-x}Sr_xRuO_4$. However, recent theoretical studies on the two-band Hubbard model clearly reveal the possibility of an OSMT under rather general conditions.

Notice that, although half-filled, this γ band does not present particle-hole symmetry, in particular due to the Van Hove singularity that appears slightly above the Fermi energy and which peak is enhanced due to the band-narrowing associated to the Ca-doping. The localized hole per Ru in the quasi-one dimensional α and β bands gives a natural explanation to the experimentally measured spin $S = 1/2$ magnetic susceptibility[98]. The microscopic model used here contains these localized modes, neglecting the itinerant γ band. Under these assumptions it is natural to consider a two-dimensional extended Hubbard model for the α and β bands of the form

$$
\begin{aligned}
\mathcal{H}_{\alpha,\beta} = & -t \sum_{i,\vec{\mathbf{a}},s} \{ c^{\dagger}_{i+a_y,yz,s} c_{i,yz,s} + c^{\dagger}_{i+a_x,yx,s} c_{i,zx,s} + h.c. \} \\
& -\mu \sum_{i,s,\nu} c^{\dagger}_{i,\nu,s} c_{i,\nu,s} \\
& +U \sum_{i} \sum_{\nu} n_{i\nu\uparrow} n_{i\nu\downarrow} + U' \sum_{i} n_{i,zx} n_{i,yz} \\
& +J_H \sum_{i,s,s'} c^{\dagger}_{i,yz,s} c^{\dagger}_{i,zx,s'} c_{i,zx,s} c_{i,yz,s'} \ ,
\end{aligned}
\tag{5.3}
$$

where $c^{\dagger}_{m,i,s}$ ($c_{m,i,s}$) creates (annihilates) an electron on site i with orbital index ν ($= yz, zx$) and spin s ($n_{i,\nu,s} = c^{\dagger}_{i,\nu,s} c_{i,\nu,s}$, $n_{i,\nu} = n_{i,\nu,\uparrow} + n_{i,\nu,\downarrow}$; $\vec{\mathbf{a}} = (a_x, a_y) = (1,0)$ or $(0,1)$ basis lattice vector). With this hamiltonian we restrict ourselves to nearest-neighbor hopping and on-site interaction for the intra- and inter-orbital Coulomb repulsion, U and U', respectively, and the Hund's rule coupling J_H. The hopping terms considered in this model come from the π-hybridization between the Ru-d and O-p-orbitals and lead to the formation of two independent quasi-one-dimensional bands: the band associated to the d_{yz}-orbital disperses only in the y-direction while the band associated to the d_{zx}-orbital disperses in the x-direction.

In the strongly interacting limit the localized degrees of freedom become important. The orbital degrees of freedom lead to two different configurations, $|+\rangle$ and $|-\rangle$ corresponding to the singly occupied d_{zx} and d_{yz} orbitals, respectively. On the other hand, the spin 1/2 leads to other two states, $|\uparrow\rangle$ and $|\downarrow\rangle$. Both, spin and orbital degrees of freedom correspond to a 2D SU(2)-symmetric Hilbert space. Therefore, the isospin operators are defined as:

$$
I^z|\pm\rangle = \pm\frac{1}{2}|\pm\rangle, \qquad I^+|-\rangle = |+\rangle, \qquad I^-|+\rangle = |-\rangle \ . \tag{5.4}
$$

The orbital and magnetic degrees of freedom lead to four possible different configurations at each site, represented by the states $\{|\uparrow +\rangle, |\uparrow -\rangle, |\downarrow +\rangle, |\downarrow -\rangle\}$. From the two band hamiltonian $\mathcal{H}_{\alpha,\beta}$ it is possible to derive, within second order perturbation in t/U, the following effective hamiltonian that has the form of a Kugel-Khomskii model[99]:

$$
\begin{aligned}
\mathcal{H}_{eff} = J \sum_{i,\vec{\mathbf{a}}} \big[& \big\{ A(I^z_{i+\vec{\mathbf{a}}} + \eta_{\vec{\mathbf{a}}})(I^z_i + \eta_{\vec{\mathbf{a}}}) + B \big\} \mathbf{S}_{i+\vec{\mathbf{a}}} \cdot \mathbf{S}_i \\
& + [C(I^z_{i+\vec{\mathbf{a}}} + \eta'_{\vec{\mathbf{a}}})(I^z_i + \eta'_{\vec{\mathbf{a}}}) + D] \big]
\end{aligned}
\tag{5.5}
$$

where

$$A = \frac{3\alpha^2 + 1}{(3\alpha - 1)(\alpha + 1)} \tag{5.6}$$

$$B = \frac{-(1-\alpha)^2}{(3\alpha^2 + 1)(3\alpha - 1)(\alpha + 1)} \tag{5.7}$$

$$C = \frac{5 - 3\alpha}{4(3\alpha - 1)} \tag{5.8}$$

$$D = \frac{1}{(5 - 3\alpha)(3\alpha - 1)} \tag{5.9}$$

$$\eta_{\vec{\mathbf{a}}} = \frac{(3\alpha - 1)(\alpha + 1)}{2(3\alpha^2 + 1)}(a_x^2 - a_y^2) \tag{5.10}$$

$$\eta'_{\vec{\mathbf{a}}} = \frac{3\alpha - 1}{2(5 - 3\alpha)}(a_x^2 - a_y^2). \tag{5.11}$$

$J = 4t^2/U$ and we have imposed the approximatively valid relation $U = U' + 2J_H$. Notice that $\eta_{\vec{\mathbf{a}}}$ and $\eta'_{\vec{\mathbf{a}}}$ have opposite sign for the x- and y-axis bonds. The energy scale $JC > 0$ of the isospin coupling is the largest energy in the present model. Therefore, below a critical temperature $T_{AFO} \sim JC$ antiferro-orbital (AFO) order sets in. On the other hand, the value of the spin-spin interaction lies between $J_1 = J[A(\eta_{\mathbf{a}}^2 - 1/4) + B] < 0$ and $J_2 = J[A\eta_{\mathbf{a}}^2 + B]$ depending on the orbital occupation. Thus, in the presence of AFO order the spin will align ferromagnetically (FM) below a critical temperature $T_{FM} \sim -J_1$. If, however, AFO order is suppressed, as in the case of an orthorombic distortion, (see below) the spin-spin coupling is given by J_2. We mention here that the sign of J_2 depends on the value of α. For $\alpha < \alpha_c = 0.535$ we find $J_2 < 0$ and consequently FM order settled at low temperatures whereas for $\alpha > \alpha_c$ we have $J_2 > 0$ and antiferromagnetic (AFM) order sets in at sufficiently low temperatures. This can be understood noticing that α measures the ratio between inter- and intra-orbital Coulomb interaction. A large value of α implies a large inter-orbital Coulomb repulsion U' compared to the intra-orbital interaction U, what favors doubly occupied orbitals. This leads, as it is well known for Hubbard type interactions, to an AFM order for the spins. The opposite occurs for a small value of α. To relate the present model to the experimental phase diagram we choose $\alpha = 0.75 > \alpha_c$ for the rest of this work.

In order to account for the orthorombic distortion due to the tilting of the RuO_6 octahedra, we introduce a new term in the hamiltonian $\mathcal{H}_{dist}$, defined as

$$\mathcal{H}_{dist} = \frac{1}{2}GN\varepsilon^2 + K\varepsilon \sum_i I_i^x, \tag{5.12}$$

where N is the number of Ru atoms. The strain $\varepsilon \equiv \varepsilon_{xy}$ corresponds to a volume conserving shear deformation of the lattice which is one of the two basic

orthorombic distortions. The other basic deformation is form conserving and not considered here. For our purpose this is sufficient because any orthorombic distortion yields a bias for the local orbital configuration which suppresses AFO ordering. In other words, the orthorombic distortion introduces a transverse field coupled to the isospin with the coupling constant K. Together with $\mathcal{H}_{eff}$ the second term in Eq. (5.12) allows for a quantum phase transition as function of $K\varepsilon$ [102]. The first term in Eq. (5.12), on the other hand, is a measure of the lattice elastic energy. Here G is the elastic constant. The introduction of the term $\frac{1}{2}GN\varepsilon^2$ is important for the free energy minimization process. Furthermore, as discussed later, we can relate the elasticity G in our theoretical model to the Ca concentration x of the experimental phase diagram.

Finally, in order to study the metamagnetic transition, we introduce a coupling of the system to a magnetic field, by the inclusion of the term $\mathcal{H}_{mag}$,

$$\mathcal{H}_{mag} = -g\mu_B H \sum_i S_i^x, \tag{5.13}$$

where g is the electron gyromagnetic factor, μ_B is the Bohr magneton, $\mu_B = \frac{e\hbar}{2m_e}$ (we will use units such that $g\mu_B = 1$) and H is the magnetic field strength. With all these ingredients, the full hamiltonian can be written as

$$\mathcal{H} = \mathcal{H}_{eff} + \mathcal{H}_{dist} + \mathcal{H}_{mag}. \tag{5.14}$$

In the next section we treat this model in a mean field approximation.

5.7 Mean-field analysis.

It has been shown that a mean field decoupling for $\mathcal{H}_{eff}$ reproduces well some of the features of $Ca_{2-x}Sr_xRuO_4$ in the x region where the band filling responds to the (3,1) orbital occupation [99]. Here we extend this analysis to the full hamiltonian Eq.(5.14) and obtain the zero and finite magnetic field phase diagrams where the different competing orders of the system are represented.

We define the mean-field order parameters for the z-component of the isospin and for the spin, respectively:

$$\langle I_i^z \rangle = t_i = \begin{cases} t_A & if \quad i \in A \\ t_B & if \quad i \in B \end{cases} \tag{5.15}$$

$$\langle S_i^\delta \rangle = m_i^\delta = \begin{cases} m_A^\delta & if \quad i \in A \\ m_B^\delta & if \quad i \in B \end{cases} \tag{5.16}$$

where $\delta = x, z$. We have made use of the bipartite structure of our hamiltonian. The $A-$ and $B-$ subscripts stand for the corresponding sublattices.

The partition function of the system can be calculated by $\mathcal{Z}(\beta) = Tre^{-\beta\mathcal{H}}$, where $\beta = 1/k_BT$. The bipartite nature of the lattice splits our system into two different subsystems, so we can express the partition function as

$$\mathcal{Z}(\beta) = e^{-\beta E_0} \prod_{\substack{i \in A,B \\ \alpha \in t,s}} \mathcal{Z}_i^\alpha \tag{5.17}$$

where E_0 denote the energy density (per hole) corresponding to the term in our mean-field Hamiltonian that does not couple to any spin or isospin operator,

$$\begin{aligned} E_0 = J\Big(&-6A\, t_A t_B m_A m_B - 2(A\,\eta_{\vec{\mathbf{a}}}^2 + B) m_A m_B \\ &-2C\, t_A t_B + 2C\,{\eta'_{\vec{\mathbf{a}}}}^2 + 2D\Big) + \frac{G}{2}\varepsilon^2. \end{aligned} \tag{5.18}$$

Now we can define the orbital $\mathcal{Z}_i^t$ and the magnetic $\mathcal{Z}_i^s$ one-particle partition functions as [103]:

$$\mathcal{Z}_{i\in A,B}^t = Tr_i e^{-\beta \mathsf{H}_i^t I_i} \tag{5.19}$$

$$\mathcal{Z}_{i\in A,B}^s = Tr_i e^{-\beta \mathsf{H}_i^s S_i} \tag{5.20}$$

where H_i^t and H_i^s are the molecular field vectors that couple to the isospin and spin degrees of freedom. If we call F to the total free energy of the system, the free energy per site (per hole) $\mathcal{F} = F/N$, where $N = N_A + N_B$ is the total number of holes, would be:

$$\mathcal{F} = -\frac{1}{\beta}\ln\mathcal{Z} = E_0 - \frac{1}{\beta}\left(\ln\mathcal{Z}_A^t + \ln\mathcal{Z}_B^t + \ln\mathcal{Z}_A^s + \ln\mathcal{Z}_B^s\right) \tag{5.21}$$

It is worth defining the staggered $\phi_s = (\phi_A - \phi_B)/2$ and uniform $\phi_0 = (\phi_A + \phi_B)/2$ components of the order parameters, where ϕ stands for the isospin t_i and spin m_i^δ mean fields. When the magnetic field is applied, we will have a uniform component of the magnetization in the transverse direction $m_A^x = m_B^x = m_0$, and a staggered component in the z-direction, $m_A^z = -m_B^z = m_s$. The calculated free energy reads

$$\begin{aligned}\mathcal{F} = J\,\Big[&6A\,t_s^2(m_0^2-m_s^2) - 2(A\,\eta_{\vec{\mathbf{a}}}^2+B)(m_0^2-m_s^2)\\ &+2C\,t_s^2 + 2C\,\eta_{\vec{\mathbf{a}}}'^{\,2} + 2D\Big] + \frac{G}{2}\varepsilon^2\\ &-\frac{2}{\beta}\ln\left[2\cosh\left[\frac{\beta}{2}\sqrt{K^2\varepsilon^2 + 4J^2(A\,t_s(m_0^2-m_s^2)+C\,t_s)^2}\right]\right]\\ &-\frac{2}{\beta}\ln\left[2\cosh\left[\frac{\beta}{2}\sqrt{f(t_s,m_0,m_s)}\right]\right],\end{aligned} \tag{5.22}$$

where

$$\begin{aligned}f(t_s,m_0,m_s) = \big(&-g\mu_B H - 2J\,A\,t_s^2 m_0 + 2J(A\,\eta_{\vec{\mathbf{a}}}^2+B)m_0\big)^2\\ &+4J^2\left(A\,t_s^2 m_s - (A\,\eta_{\vec{\mathbf{a}}}^2+B)m_s\right)^2.\end{aligned} \tag{5.23}$$

In the following we discuss several limiting cases.

5.7.1 Absence of applied magnetic field.

In this case, due to the rotational invariance of the system for $H = 0$ (no direction is distinguished), the spins in the Heissemberg term of $\mathcal{H}_{eff}$ are effectively Ising spins that can point only up or down and. Therefore, we can treat $\vec{\mathbf{S}}_i$ as an Ising spin variable pointing in the z-direction. For $\alpha = 0.75$ we find the phase diagram shown in Fig.[5.7(a)]. We can distinguish two main regions: one characterized by a finite distortion $\varepsilon > 0$ which leads to a FO order, and other with zero-distortion $\varepsilon = 0$, characterized by a high-temperature para-orbital (PO) order and a low temperature AFO order. In addition, several magnetic orders appear in the two regions at different energy scales. We can see a bicritical point where the two second order lines (T_{FO} and T_{AFO}) meets the first order line that separates the two orbital ordered phases. On the other hand, there are two critical endpoints where the second order lines T_{AFM} and T_{FM} meet the first order transition line. In the following subsections we discuss more in detail these two regions.

Non-distorted system: tetragonal symmetry.

In this section we study the case $\varepsilon = 0$, corresponding to the region of the phase diagram Fig.[5.7(a)] placed on the right hand side to the first order transition line. Here $t_s = t_A = -t_B$, and $m_0 = m_A = m_B$ (as we stated above, the isospin order is reached before the spin order, and we get AFO order at T_{AFO} followed by FM at some lower temperature T_{FM}).

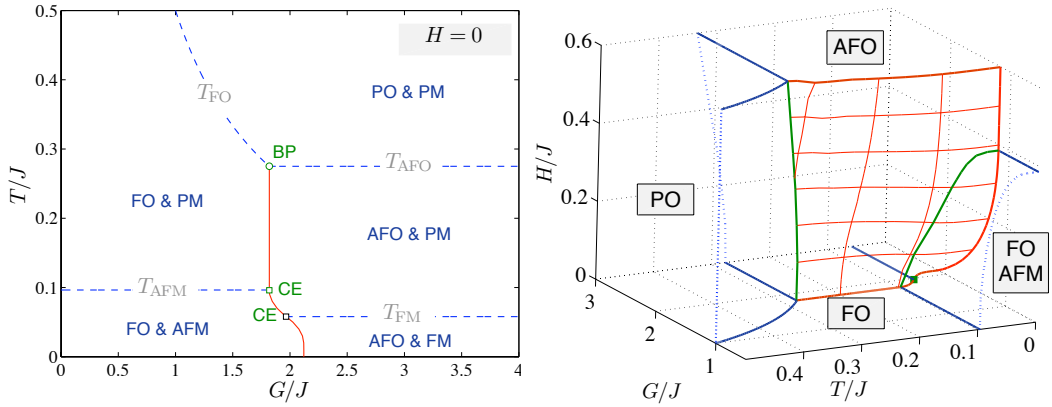

(a) $T-G$ phase diagram (b) phases3D

Figure 5.7: (a) $T-G$ phase diagram for $\alpha = 0.75$ and $H = 0$. Dashed blue lines set for second order phase transitions, while full red lines represent first order transitions. BP is a bicritical point and CE are two critical endpoints. (b) $T-G-H$ phase diagram for $\alpha = 0.75$. Blue surfaces set for second order phase transition, while red surfaces represent first order transitions. Green lines represents either a bicritical line or a critical endline.

From the free energy Eq.(5.22), and taking into account that $T_{AFO} > T_{FM}$, we can obtain from the condition $\partial_{t_s}\mathcal{F}|_{m_0=0} = 0$ that $2t_s = \tanh\left(\frac{CJt_s}{k_BT}\right)$ what gives us an antiferro-orbital critical temperature of

$$k_BT_{AFO} = \frac{JC}{2}. \tag{5.24}$$

On the other hand, assuming that the FM phase appears once the AFO order parameter has saturated, we can obtain from the equation $\partial_{m_0}\mathcal{F}|_{t_s=1/2} = 0$, using the approximation $\tanh(JC/2k_BT_{FM}) \simeq 1$ (the transition occurs at a small temperature), the next expression for T_{FM}:

$$k_BT_{FM} \simeq -\frac{J}{2}\left(B + A\left(\eta_{\vec{\mathbf{a}}}^2 - \frac{1}{4}\right)\right). \tag{5.25}$$

Distorted system: orthorombic symmetry.

Now we discuss the region of the zero-field phase diagram (Fig.[5.7(a)]) characterized by a finite distortion of the lattice. This is the region on the left hand side to the first order transition line. If we switch on the distortion in the system, we will have a finite T_{FO}, below which the ferro-orbital order appears. In the corresponding part of the phase diagram we can see two second order transitions (for t_s and m_0), and one first order transition (for ε). The ferro-orbital transition

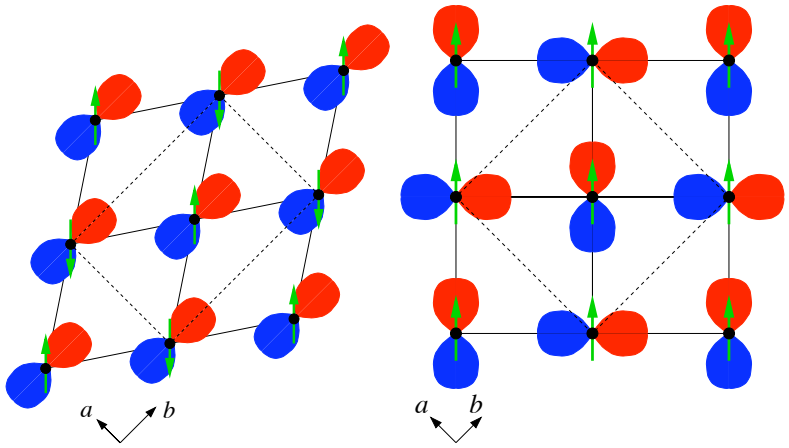

(a) AFO & FM (b) FO & AFM

Figure 5.8: Sketch of the low temperature competing orders of the system. In (a) it is represented a lattice with tetragonal symmetry with antiferro-orbital order plus ferromagnetism (AFO & FM). In (b), a lattice with orthorombic symmetry and ferro-orbital order plus antiferromagnetism (FO & AFM).

temperature can be calculated taking into account that this FO order has the highest transition temperature, and from the condition $\partial_\varepsilon \mathcal{F}|_{t_s,m_0=0} = 0$, what gives $G\varepsilon = K \tanh\left(\frac{K\varepsilon}{2k_B T_{FO}}\right)$ one easily obtain that

$$k_B T_{FO} \simeq \frac{K^2}{2G} \tag{5.26}$$

The T_{FM} temperature can be calculated as in the previous section, leading to Eq.(5.25). If the value of the parameter α is such that the magnetic transition is towards antiferromagnetism instead of towards ferromagnetism ($\alpha \geq 0.535$) the T_{AFM} transition temperature can be calculated from $\partial_{m_s} \mathcal{F}|_{t_s=0} = 0$. This condition gives that $2m_s = \tanh\left(\frac{Jm_s(B+A\eta_{\vec{\mathbf{a}}}^2)}{k_B T_{AFM}}\right)$, from which we can easily obtain

$$k_B T_{AFM} = \frac{J}{2}\left(B + A\eta_{\vec{\mathbf{a}}}^2\right). \tag{5.27}$$

Finally, in Fig.[5.8] we can see the low temperature competing orders that appear in the theoretical phase diagram shown in Fig.[5.7(a)]. For large G values we still have a zero-distortion $\varepsilon = 0$. In this case the symmetry of the lattice is tetragonal and the orbital and spin orders are AFO and FM respectively, as represented on the left hand side of Fig.[5.8]. On the other hand, for small values of G, the free energy minimization gives a ground state with a finite distortion of the lattice due to a rotation of ab-plane around the [110] axis, and characterized by a $\varepsilon > 0$ that breaks the tetragonal symmetry. In this case the orbital and

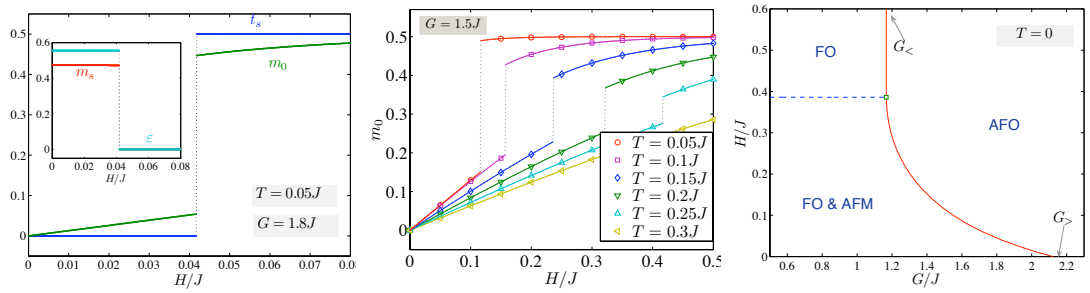

(a) (b) (c)

Figure 5.9: (a) Evolution of the transverse magnetization m_0 (green line) and staggered isospin order parameter t_s (dark blue line) as a function of the applied magnetic field, for the parameter values $\alpha = 0.75$, $G = 1.8J$ and $T = 0.05J$. The inset shows the drops of the distortion (light blue line) and staggered magnetization (red line) that occurs at the metamagnetic transition. (b) Evolution of the transverse magnetization m_0 as a function of the applied magnetic field for different temperatures, for the parameter values $\alpha = 0.75$, $G = 1.5J$. (c) $H - G$ phase diagram for $T = 0$. The values $G_<$ and $G_>$ bound the G-axis region where a metamagnetic transition is allowed. The first order line (full red) meets the second order line (dashed blue) at a QCEP.

magnetic orders are FO and AFM respectively, and the new symmetry of the lattice is orthorombic (as shown on the right hand side of Fig.[5.8]).

5.7.2 Applied magnetic field: metamagnetic transition.

Now we introduce in our analysis the effect of an external magnetic field applied in the x-direction, that enters in our hamiltonian by the term $\mathcal{H}_{mag} = -g\mu_B H \sum_i S_i^x$. In this case we obtain the phase diagram represented in Fig.[5.7(b)]. Here we can study how the phase transition lines of Fig.[5.7(a)] grow in the H-axes (z-direction). The two second order surfaces T_{FO} and T_{AFO} meets the first order surface (red sheet) at the green bicritical line drawn at the left hand side of the diagram. On the other hand, a critical endline (green line) can be seen on the right hand side of the diagram where the (blue) second order AFM surface touches the (red) first order surface. At high magnetic fields this line ends in a quantum critical endpoint (QCEP) at $T = 0$. Due to the fact that for finite field we always have a FM order, the second order transition line T_{FM} only touches the first order surface on the $H = 0$ plane, giving rise to a critical endpoint (CEP).

In addition, also a first order metamagnetic transition can be obtained from this model, as can be seen in Fig.[5.9(a)]. Here we show how the magnetization in the direction of the applied field m_0, the staggered isospin t_s, the strain ε and the staggered magnetization m_s change as a function of the field strength. Starting

from an AFM ground state at zero magnetic field, we find a first-order phase transition towards a FM state under the application of a magnetic field H. This magnetic transition is accompanied in our system by another structural transition, where an orthorombic FO phase changes discontinuously towards an AFO phase with tetragonal symmetry for the same metamagnetic critical field H_c. The first order surface (red region in Fig.[5.7(b)]) defines the metamagnetic surface, through which the uniform magnetization of the system jumps discontinuously under the application of an external magnetic field H.

In Fig.[5.9(b)] we see the metamagnetic transition for different values of the temperature. Here we can see how the critical field $H_c(T)$ increases when we rise the temperature, and how the magnetization also saturates first for transitions that occur at low temperatures. There exists a critical temperature that coincides with the AFO transition temperature $T_{CMM} = T_{AFO}$, above which no first order magnetic transition occurs. This is due to the fact that in our model, this first order transition in the magnetization is accompanied by the vanishing of the distortion and the appearance of antiferro-orbital order. Therefore, if we are above the critical AFO temperature T_{AFO}, no first order structural transition is possible either.

Finally, in Fig.[5.9(c)] we plot the H-G-phase diagram for zero temperature. It is worth noting that a first order metamagnetic transition (accompanied by a structural transition) can only occur at $T = 0$ if we apply a magnetic field in the FO & AFM zone, and only for elasticity values belonging to the region $G_< < G < G_>$, where

$$G_< = \frac{K^2}{J(C + A/4)} \tag{5.28}$$

$$G_> = \frac{K^2}{J\left(A\left[1/4 - 2\eta_{\vec{\mathbf{a}}}^2\right] - 2B + C\right)}. \tag{5.29}$$

Notice that at $G_>$ there is a first order structural phase transition for $T, H = 0$. In Fig.[5.9(c)] it can be seen that the metamagnetic critical field decreases as G is enhanced. The QCEP field at $G_<$ can be calculated from

$$\left.\frac{\partial \mathcal{F}}{\partial m_0}\right|_{t_s, m_s, T=0} = -g\mu_B H_{QCEP} \tag{5.30}$$

leading to the result

$$g\mu_B H_{QCEP} = 2J(B + A\eta_{\vec{\mathbf{a}}}^2). \tag{5.31}$$

5.8 Comparison to experiments

Finally we aim to justify the microscopic model proposed in section 5.6 by means of a direct comparison between theoretical and experimental results. In particular, we will look at the $T = 0$ phase diagram as well as at the magnetostriction and magnetization measurements that characterize the metamagnetic transition in $Ca_{2-x}Sr_xRuO_4$. The theoretical zero-field phase diagram (Fig.[5.7(a)]) can be directly compared to the experimental $T - x$-phase diagram obtained for $Ca_{2-x}Sr_xRuO_4$ [98] if we ignore the region-I with $x < 0.2$, where the Mott-insulating phase sets. This way we can relate the orders that appear in the left hand side of the phase diagram Fig.[5.7(a)] to the phases that are observed in region II of the experimental phase diagram sketched in Fig.[5.3]. In both cases we have a finite distortion of the lattice what leads to an orthorombic symmetry. The distortion, which in the real material is due to a tilting of the RuO_6-octahedra, in our results is associated to a rotation of the 2D lattice where the orbital and magnetic modes live. Once ε vanishes, we find a transition to a tetragonal phase with AFO order and FM for small temperatures, as that found in region III of the experimental phase diagram for $x > 0.5$. An identification between elasticity G and Sr concentration x makes sense because, in the theoretical model, the larger the G, the smaller the ε. In the experimental system, on the other hand, the larger the doping x, the weaker the tilting of the octahedra becomes.

The metamagnetic transition shown in Fig.[5.9(a)] can be related to the experimental metamgnetic transition [94, 95] in the following way: for zero magnetic field $H = 0$ and for a temperature and doping (G in our language) such that we are in the FO and AFM zone of the phase diagram (region II of Fig.[5.3]), we have a finite strain ε and a zero component of the magnetization along the x-direction. If we now switch on the transverse magnetic field, a finite component of m_0 appears, although for small enough fields, the strain is still present in the system. For some critical field $H_c(T, G)$ we find a first order transition in the magnetization m_0 that jumps discontinuously to some larger value, while the strain drops suddenly to zero at the same time. The transcription of this to the experiments is that the octahedra has restored its structure before its tilting, and now the c-axes has come back to the direction that it had in region III of the phase diagram, although this does not necessarily mean that the tetragonal symmetry is restored in the system. This explains the inversion of the structural distortion that occurs upon cooling at zero field, and that it is reverted by applying a high magnetic field at low temperatures, as seen in the experiments[94].

This first order transition in the magnetization corresponds to the metamagnetic transition observed in the experiments. Notice that in our case, when we do not take into account the inhomogeneity of the system, it looks like a *real* first

order transition. In the experiments the transition is much more smooth, and it does not present a clear discontinuity. This can be studied by modifying $\mathcal{H}_{dist}$ introducing a random field coupling[104].

The dependence of the first order magnetic transition on the temperature shown in Fig.[5.9(b)] can be related to the experimental measurements too. This is actually the expected behavior and reproduces some of the results shown in Ref.[95]. Notice again that in this case of $x = 0.5$ the metamagnetic transition, if there exists, it does not look like a first order transition due to the lack of homogeneity in the system, as it was discussed above. This behavior is also useful to explain the magnetostriction measurements done in this material. If we look for example at the magnetostriction measurements of Ref.[95], where they show $\Delta L(H)/L_0$ along the c axis as a function of the applied magnetic field, these results can be interpreted as the response of the lattice structure to the metamagnetic transition: the jump in the magnetization is coupled to an increase in the length of the c-lattice constant, restoring the structure that the lattice had before the octahedra tilting and, therefore leading to a vanishing of the distortion (see inset of Fig.[5.9(a)]).

Finally, the critical elasticity values found in Fig.[5.9(c)], bounding the segment on the G-axis where the first order magnetic and structural transitions are possible at $T = 0$, can be directly related to the concentration values x of the experimental phase diagram that bound the region where the metamagnetic transition has been measured. This means that $G_<$ would correspond to $x = 0.2$ and $G_>$ to $x = 0.5$. This is consistent with the experimental results that show a smaller energy scale for the transition at $x = 0.5$ compare to the one at $x = 0.2$. The metamagnetic transition is shifted towards lower fields when the Sr content is enhanced from $x = 0.2$ to 0.5. On the other hand, the first order structural transition occurred at zero temperature for $G_>$ in the theoretical model can be related to the structure quantum phase transition of $Ca_{2-x}Sr_xRuO_4$ at $x = 0.5$. Finally, the QCEP found in the present model at $(G_<, H_{QCEP})$ seems to be related to the low temperature critical endpoint discussed for $Ca_{2-x}Sr_xRuO_4$at $x = 0.2$ [95].

5.9 Conclusion

In summary, we have presented a microscopic model that accounts for the magnetic and orbital orders that seem to be important for the physics observed on regions II and Ca-rich zone of region III (near $x = 0.5$) of $Ca_{2-x}Sr_xRuO_4$. We have done a mean field analysis to obtain the magnetic and structural phases measured for this system. The main assumption of this model is that over the studied region, there is a Mott localization for the three electrons that occupy the

d_{yz} and d_{zx} orbitals, while the electron in the d_{xy} orbital remains itinerant [99]. Our model also reproduces the metamagnetic transition that $Ca_{2-x}Sr_xRuO_4$ undergoes as a magnetic field is applied.

The identification of the elasticity in the theoretical model to the Sr content x in the experimental system gives a good qualitative description of the different phenomena observed on this ruthenate. The energy scales also coincides in both experimental and theoretical systems. It should be notice that we have neglected several effects, like disorder or the interaction between the itinerant γ band to the localized α and β bands. Even so, our results give a good picture of the physics of $Ca_{2-x}Sr_xRuO_4$.

Finally, the model also seems to contain a kind of quantum criticality, namely a quantum critical endpoint that is reached when a line of critical endpoints ends at the $T = 0$ plane of the 3D phase diagram Fig.[5.7(b)]. It is tempting to relate this QCEP to the suggested metamagnetic critical endpoint for $Ca_{1.8}Sr_{0.2}RuO_4$ at very low temperatures [95].

Appendix A

Appendix to Chapter 3

A.1 Susceptibility

A.1.1 Forward scattering interaction.

In this section we calculate the pair bubble diagram Fig.**??** for the case where the electron and hole momenta in the bubble lie close to each other in the same branch of the Fermi surface

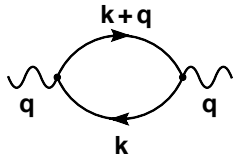

Figure A.1: Electron-hole pair bubble diagram.

This channel dominates the processes with small momentum transfers $\mathbf{q}$ (see Fig.A.2). This kind of processes plays a major role in systems with long-range interactions, where the scattering amplitudes diverge for small momentum transfers, but it is also important in several low energie properties of systems with short-range interactions, and may lead to quite subtle effects especially in low dimensions [105]. For example, forward scattering governs low-energy long-wavelength response of a Fermi liquid as well as the breakdown of Fermi liquid theory in one-dimensional systems. The particle-hole bubble is essentially the dynamical density-density correlation function of the non-interacting system, and it is important for subsequent explicit calculations of the self-energy and the effective interaction. The susceptibility can be calculated according to Eq.(3.7) where we have introduced the sharp cutoff Λ.

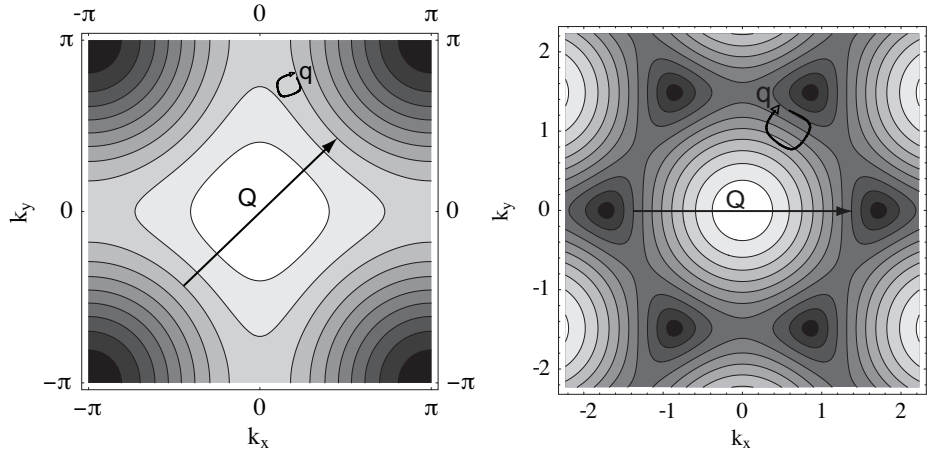

(a) (b)

Figure A.2: (a) The two processes studied in this work for a square lattice. (b) Same but for the honeycomb lattice.

$$i\Pi(\vec{\mathbf{q}},\omega) = \frac{U^2}{(2\pi)^3}\int d\omega' \int d^2k\, \Theta(\Lambda - |\epsilon_{\vec{\mathbf{k}}}|)\Theta(\Lambda - |\epsilon_{\vec{\mathbf{k}}+\vec{\mathbf{q}}}|) G_0(\vec{\mathbf{k}},\omega') G_0(\vec{\mathbf{k}}+\vec{\mathbf{q}},\omega+\omega') \tag{A.1}$$

The virtual states in the loop have to be kept within the band determined by the cutoff, and only states with energies between $-\Lambda$ and Λ are allowed. First, let us evaluate the frequency integral. The two possible contributions come from the cases where the two poles lie on different half-planes of the complex ω-plane. In the case where the two poles of the Green's functions lie in the same half-plane, closing the contour in the other half-plane gives zero for this integral. Therefore, using to the residue theorem, only the next cases remain:

1. $\epsilon_{\vec{\mathbf{k}}} > 0$ and $\epsilon_{\vec{\mathbf{k}}+\vec{\mathbf{q}}} < 0$

$$\int_{-\infty}^{+\infty} \frac{d\omega'}{2\pi} \frac{1}{\omega' - \epsilon_{\vec{\mathbf{k}}} + i\delta} \frac{1}{\omega' + \omega - \epsilon_{\vec{\mathbf{k}}+\vec{\mathbf{q}}} - i\delta} = \frac{-i}{\epsilon_{\vec{\mathbf{k}}} - \epsilon_{\vec{\mathbf{k}}+\vec{\mathbf{q}}} + \omega - i\delta} \tag{A.2}$$

2. $\epsilon_{\vec{\mathbf{k}}} < 0$ and $\epsilon_{\vec{\mathbf{k}}+\vec{\mathbf{q}}} > 0$

$$\int_{-\infty}^{+\infty} \frac{d\omega'}{2\pi} \frac{1}{\omega' - \epsilon_{\vec{\mathbf{k}}} - i\delta} \frac{1}{\omega' + \omega - \epsilon_{\vec{\mathbf{k}}+\vec{\mathbf{q}}} + i\delta} = \frac{i}{\epsilon_{\vec{\mathbf{k}}} - \epsilon_{\vec{\mathbf{k}}+\vec{\mathbf{q}}} + \omega + i\delta} \tag{A.3}$$

Then the vertex can be written as

$$\Pi(\vec{\mathbf{q}},\omega)=\frac{U^2}{(2\pi)^2}\left\{\int_{\substack{\epsilon_{\vec{\mathbf{k}}}<0\\ \epsilon_{\vec{\mathbf{k}}+\vec{\mathbf{q}}}>0}} d^2k\frac{\Theta(\Lambda-|\epsilon_{\vec{\mathbf{k}}}|)\Theta(\Lambda-|\epsilon_{\vec{\mathbf{k}}+\vec{\mathbf{q}}}|)}{\epsilon_{\vec{\mathbf{k}}}-\epsilon_{\vec{\mathbf{k}}+\vec{\mathbf{q}}}+\omega+i\delta}-\right.$$

$$\left.-\int_{\substack{\epsilon_{\vec{\mathbf{k}}}>0\\ \epsilon_{\vec{\mathbf{k}}+\vec{\mathbf{q}}}<0}} d^2k\frac{\Theta(\Lambda-|\epsilon_{\vec{\mathbf{k}}}|)\Theta(\Lambda-|\epsilon_{\vec{\mathbf{k}}+\vec{\mathbf{q}}}|)}{\epsilon_{\vec{\mathbf{k}}}-\epsilon_{\vec{\mathbf{k}}+\vec{\mathbf{q}}}+\omega-i\delta}\right\}=\Pi_a^{(2)}+\Pi_b^{(2)} \quad \text{(A.4)}$$

by using the identity

$$\frac{1}{\epsilon_{\vec{\mathbf{k}}}-\epsilon_{\vec{\mathbf{k}}+\vec{\mathbf{q}}}+\omega+i\delta}=P\left[\frac{1}{\epsilon_{\vec{\mathbf{k}}}-\epsilon_{\vec{\mathbf{k}}+\vec{\mathbf{q}}}+\omega}\right]-i\pi\delta(\epsilon_{\vec{\mathbf{k}}}-\epsilon_{\vec{\mathbf{k}}+\vec{\mathbf{q}}}+\omega) \quad \text{(A.5)}$$

the imaginary part of the bubble corresponding to the first piece is

$$\mathrm{Im}\Pi_a^{(2)}(\vec{\mathbf{q}},\omega)=\frac{U^2}{(2\pi)^2}(-\pi)\int_{\substack{\epsilon_{\vec{\mathbf{k}}}<0\\ \epsilon_{\vec{\mathbf{k}}+\vec{\mathbf{q}}}>0}} d^2k\Theta(\Lambda-|\epsilon_{\vec{\mathbf{k}}}|)\Theta(\Lambda-|\epsilon_{\vec{\mathbf{k}}+\vec{\mathbf{q}}}|)\delta(\epsilon_{\vec{\mathbf{k}}}-\epsilon_{\vec{\mathbf{k}}+\vec{\mathbf{q}}}+\omega) \quad \text{(A.6)}$$

In order to evaluate this integral we do the next transformations:

$$\int dk_x dk_y \longrightarrow \int dk_\perp dk_\parallel \longrightarrow \int d\varepsilon d\overline{\varepsilon} \quad \text{(A.7)}$$

If we use the change of variables

$$\left.\begin{array}{r} k_\perp = k_y+\frac{\beta}{v_F}k_x^2 \\ k_\parallel = k_x+q_x/2 \end{array}\right\} \quad \text{(A.8)}$$

the dispersion relation can be written as

$$\varepsilon=\epsilon_{\vec{\mathbf{k}}}=v_F k_\perp \quad \text{(A.9)}$$

$$\overline{\varepsilon}=\epsilon_{\vec{\mathbf{k}}+\vec{\mathbf{q}}}=v_F k_\perp+v_F q_\perp+2\beta k_\parallel^2+\frac{2}{9}\beta q_\parallel^2$$

If we want to integrate in ε and $\overline{\varepsilon}$ variables, we have to calculate the Jacobian for these new transformations. It is straightforward to show that

$$J\left(\frac{k_x,k_y}{\varepsilon,\overline{\varepsilon}}\right)=\left|\frac{\partial(k_x,k_y)}{\partial(\varepsilon,\overline{\varepsilon})}\right|=\left|\begin{array}{cc}\frac{\partial k_x}{\partial\varepsilon} & \frac{\partial k_x}{\partial\overline{\varepsilon}} \\ \frac{\partial k_y}{\partial\varepsilon} & \frac{\partial k_y}{\partial\overline{\varepsilon}}\end{array}\right|=-\frac{1}{4\beta v_F k_\parallel} \quad \text{(A.10)}$$

From A.9 we have:

$$\overline{\varepsilon} - \varepsilon = v_F q_\perp + 2\beta k_\parallel^2 + \frac{2}{9}\beta q_\parallel^2 \tag{A.11}$$

which gives

$$k_\parallel^2 = \frac{\overline{\varepsilon} - \varepsilon - v_F q_\perp - \frac{2}{9}\beta q_\parallel^2}{2\beta} \tag{A.12}$$

We define $\mathrm{M}_{\tilde{\mathbf{q}}}^{\mathrm{F}}$ as

$$\mathrm{M}_{\tilde{\mathbf{q}}}^{\mathrm{F}} = \mathrm{v_F q_\perp} + \frac{2}{9}\beta \mathrm{q}_\parallel^2 \tag{A.13}$$

so the total transformation can be expressed as

$$\int dk_x dk_y \longrightarrow \frac{1}{4\beta v_F} \int \left(\frac{\overline{\varepsilon} - \varepsilon - \mathrm{M}_{\tilde{\mathbf{q}}}^{\mathrm{F}}}{2\beta} \right)^{-\frac{1}{2}} d\varepsilon d\overline{\varepsilon} \tag{A.14}$$

We have for the positive frequencies the next expression for the imaginary part of the susceptibility, which measures the density of electron-hole pairs with energy ω:

$$\mathrm{Im}\Pi_a^{(2)}(\vec{\mathbf{q}}, \omega) = -\frac{U^2\pi}{(2\pi)^2} \int_{\substack{\varepsilon<0 \\ \overline{\varepsilon}>0}} d\varepsilon d\overline{\varepsilon} \Theta(\Lambda - |\varepsilon|)\Theta(\Lambda - |\overline{\varepsilon}|)\delta(\varepsilon - \overline{\varepsilon} + \omega) \left| J\left(\frac{k_x, k_y}{\varepsilon, \overline{\varepsilon}} \right) \right| \tag{A.15}$$

$$= -\frac{U^2\pi}{(2\pi)^2} \frac{1}{4\beta v_F} \sqrt{\frac{2\beta}{\omega - \mathrm{M}_{\tilde{\mathbf{q}}}^{\mathrm{F}}}} \int_{\varepsilon<0} d\varepsilon \Theta(\Lambda - |\varepsilon|)\Theta(\Lambda - |\varepsilon + \omega|) \tag{A.16}$$

We are interested on frequencies below the cutoff

$$\left.\begin{array}{c} \overline{\varepsilon} = \varepsilon + \omega \\ \overline{\varepsilon} > 0 \\ \varepsilon < 0 \end{array}\right\} \Rightarrow \varepsilon + \omega > 0 \Rightarrow \varepsilon > -\omega \tag{A.17}$$

and the integral would be of the form $\int_{-\omega}^{0} d\varepsilon = \omega$. In fact, integral in (A.15) is between the FS and the neighboring constant-energy surface, $\epsilon_{\vec{\mathbf{k}}} = \epsilon_{\mathrm{F}} - \omega$ or, equivalently, over that part of the surface $\epsilon_{\vec{\mathbf{k}}+\vec{\mathbf{q}}} - \epsilon_{\vec{\mathbf{k}}} = \omega$ which lies inside the FS and outside the one displaced by $\vec{\mathbf{q}}$. This gives the expression for $\mathrm{Im}\Pi_a^{(2)}$:

$$\mathrm{Im}\Pi_a^{(2)}(\vec{\mathbf{q}}, \omega) = -\frac{U^2\pi}{(2\pi)^2} \frac{\omega}{4v_F\beta} \sqrt{\frac{2\beta}{\omega - \mathrm{M}_{\tilde{\mathbf{q}}}^{\mathrm{F}}}} \qquad \omega > 0 \tag{A.18}$$

Similarly we can obtain the result for negative frequencies, $\mathrm{Im}\Pi_b^{(2)}$, which reads:

$$\mathrm{Im}\Pi_b^{(2)}(\vec{\mathbf{q}},\omega) = -\frac{U^2\pi}{(2\pi)^2}\frac{-\omega}{4\beta v_F}\sqrt{\frac{2\beta}{\omega - \mathrm{M}^{\mathrm{F}}_{\tilde{\mathbf{q}}}}} \qquad \omega < 0 \tag{A.19}$$

Then, the results for $\mathrm{Im}\Pi_a^{(2)}$ and for $\mathrm{Im}\Pi_b^{(2)}$ are the same, but a minus sign. But in $\mathrm{Im}\Pi_a^{(2)}$ the frequency has to be positive and in $\mathrm{Im}\Pi_b^{(2)}$ the frequency has to be negative, so we can generalize the result writing an absolute value of the frequency and have the result for the imaginary part of the bubble for processes where the electron and hole momenta lie in the same branch of the Fermi line and which pair frequency is well below the cutoff Λ as

$$\mathrm{Im}\Pi^{(2)}(\vec{\mathbf{q}},\omega) = -\frac{U^2\pi}{(2\pi)^2}\frac{|\omega|}{4\beta v_F}\sqrt{\frac{2\beta}{\omega - \mathrm{M}^{\mathrm{F}}_{\tilde{\mathbf{q}}}}} \tag{A.20}$$

The argument of the square root has to be positive, what gives an extra condition, $\omega\mathrm{sgn}(\beta) > \mathrm{M}^{\mathrm{F}}_{\tilde{\mathbf{q}}}\mathrm{sign}(\beta)$. We see that the cutoff Λ does not appear in the above result. This is because the $\vec{\mathbf{k}}$-integral is already limited by other small variables such as ω or $|\vec{\mathbf{q}}|$.

A.1.2 Backscattering interaction.

This case corresponds to the processes where the electron and hole interchange a momentum like $\mathbf{Q}$ in Fig.A.2. These processes can have an important contribution in the case of a short range interaction, as it is the case of a Hubbard term. The computation of $\Pi(\vec{\mathbf{q}},\omega)$, altough a little bit more complex, can be done in a similar way as for the forward channel. It is helpful to use the reflection symmetry $\varepsilon_{\vec{\mathbf{k}}+\vec{\mathbf{Q}}} = \varepsilon_{-\vec{\mathbf{k}}}$. For this case we obtain:

$$\mathrm{Im}\Pi^{\mathrm{B}}(\tilde{\mathbf{Q}}+\tilde{\mathbf{q}},\omega) = -\frac{\mathrm{U}^2}{16\pi}\frac{1}{\beta \mathrm{v_F}}\begin{cases} \sqrt{2\beta(|\omega| + \mathrm{M}^{\mathrm{B}}_{\tilde{\mathbf{q}}})} - \sqrt{2\beta(\mathrm{M}^{\mathrm{B}}_{\tilde{\mathbf{q}}} - |\omega|)} \,\text{if}\, |\omega| < \mathrm{M}^{\mathrm{B}}_{\tilde{\mathbf{q}}}\,\mathrm{sgn}(\beta) \\ \mathrm{sgn}(\beta)\sqrt{2\beta(|\omega|\mathrm{sgn}(\beta) + \mathrm{M}^{\mathrm{B}}_{\tilde{\mathbf{q}}})} \qquad \text{if} \quad |\omega| > |\mathrm{M}^{\mathrm{B}}_{\tilde{\mathbf{q}}}| \end{cases} \tag{A.21}$$

where $\mathrm{M}^{\mathrm{B}}_{\tilde{\mathbf{q}}} = \mathrm{v_F q_\perp} - \frac{2}{9}\beta \mathrm{q}^2_\parallel$.

A.2 Self-energy calculation

The self-energy $\Sigma(\vec{\mathbf{k}},\omega)$ for frequencies ω on the real axis shows clearly the effect of correlations on single-particle excitations. For a local interaction, the first-order

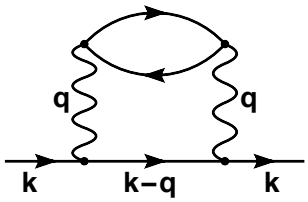

Figure A.3: Second order self-energy.

self-energy does not yield any many-body effects but merely shifts the chemical potential μ. In this section estimate the imaginary part of the self-energy according to diagram represented in Fig.A.2. The real part will be obtained from the imaginary part by Kramers-Kroning relations.

Actually we should take into account also the two-loops diagram shown in Fig.2.2(e) but since we are dealing with a constant interaction, the interaction lines can be contracted to a point, making the two diagrams look the same. Therefore the diagram in Fig.2.2(d) helds a relative factor of -2 with respect to diagram (e) due to the propagation of the two spin orientation around the fermion loop (see for example Ref.[106, 107]). For constant couplings, the imaginary part of the self-energy Eq.(3.6) can be expressed in terms of the spectral density of particle-hole excitations as[35]

$$\mathrm{Im}\Sigma^{(2)}(\vec{\mathbf{k}},\omega)=\frac{1}{(2\pi)^3}\int d\omega' d^2q \mathrm{Im}G^{(0)}\left(\vec{\mathbf{k}}-\vec{\mathbf{q}},\omega-\omega'\right)\mathrm{Im}\Pi(\vec{\mathbf{q}},\omega') \tag{A.22}$$

The imaginary part of the Green function will be:

$$\begin{aligned}\mathrm{Im}G^{(0)}(\vec{\mathbf{k}}-\vec{\mathbf{q}},\omega-\omega')&=\begin{cases}-\pi\delta\left(\omega-\omega'-\varepsilon(\vec{\mathbf{k}}-\vec{\mathbf{q}})\right)\varepsilon(\vec{\mathbf{k}}-\vec{\mathbf{q}})>0\\ +\pi\delta\left(\omega-\omega'-\varepsilon(\vec{\mathbf{k}}-\vec{\mathbf{q}})\right)\varepsilon(\vec{\mathbf{k}}-\vec{\mathbf{q}})<0\end{cases}\\ &=(-)\pi\delta\left(\omega-\omega'-\varepsilon(\vec{\mathbf{k}}-\vec{\mathbf{q}})\right)\mathrm{sgn}\left(\varepsilon(\vec{\mathbf{k}}-\vec{\mathbf{q}})\right)\end{aligned} \tag{A.23}$$

We rename in this case:

$$\begin{cases}\varepsilon=\mathrm{M}^{\mathrm{F}}_{\vec{\mathbf{q}}}=\mathrm{v_F q_\perp}+\frac{2}{9}\beta \mathrm{q}_\parallel^2\\ \overline{\varepsilon}+g=\varepsilon(\vec{\mathbf{k}}-\vec{\mathbf{q}})=v_F k_\perp-v_F q_\perp+2\beta k_\parallel^2+\frac{2}{9}\beta q_\parallel^2\end{cases} \tag{A.24}$$

where we have defined $g=v_F k_\perp+2\beta k_\parallel^2$. The Jacobian of the transformation reads

$$J\left(\frac{q_\perp,q_\parallel}{\varepsilon,\overline{\varepsilon}}\right)=\left|\frac{\partial(q_\perp,q_\parallel)}{\partial(\varepsilon,\overline{\varepsilon})}\right|=\begin{vmatrix}\frac{\partial q_\perp}{\partial\varepsilon} & \frac{\partial q_\perp}{\partial\overline{\varepsilon}}\\ \frac{\partial q_\parallel}{\partial\varepsilon} & \frac{\partial q_\parallel}{\partial\overline{\varepsilon}}\end{vmatrix}=\begin{vmatrix}v_F^{-1} & -v_F^{-1}\\ (\frac{4}{9}\beta q_\parallel)^{-1} & (\frac{4}{9}\beta q_\parallel)^{-1}\end{vmatrix}=\frac{9}{2\beta v_F q_\parallel}$$

Noting that $\overline{\varepsilon}+\varepsilon+g=\frac{4}{9}\beta q_{\parallel}^2+g$ we can write $q_{\parallel}$ as $q_{\parallel}=\frac{3}{2}\sqrt{\frac{\overline{\varepsilon}+\varepsilon}{\beta}}$. With this we can write the Jacobian of this transformation as

$$J\left(\frac{q_{\perp},q_{\parallel}}{\varepsilon,\overline{\varepsilon}}\right)=\frac{3}{\beta v_F}\sqrt{\frac{\beta}{\overline{\varepsilon}+\varepsilon}} \tag{A.25}$$

So we can express the imaginary part of the self-energy for this forward scattering case as

$$\begin{aligned}\mathrm{Im}\Sigma^{(2)}(\vec{\mathbf{k}},\omega)&=\frac{\pi}{(2\pi)^3}\left(\frac{U^2\pi}{(2\pi)^2}\frac{1}{4\beta v_F}\right)\int_{\mathbf{\Lambda}}sgn(\overline{\varepsilon}+g)\delta(\omega_k-\omega_q-\overline{\varepsilon}-g)|\omega'|\sqrt{\frac{2\beta}{\omega'-\varepsilon}}\left|J\left(\frac{q_x,q_y}{\varepsilon,\overline{\varepsilon}}\right)\right|\\&=\frac{3U^2}{64\sqrt{2}\pi^3}\frac{\mathrm{sgn}(\beta)}{v_F^2\beta}\int_{-\Lambda}^{\Lambda}d\omega'\int_{-\Lambda}^{\omega'}d\varepsilon\int_{-\varepsilon}^{+\Lambda}d\overline{\varepsilon}\frac{\delta(\omega-\omega'-\overline{\varepsilon}-g)}{\sqrt{\omega'-\varepsilon}\sqrt{\overline{\varepsilon}+\varepsilon}}\mathrm{sgn}(\overline{\varepsilon}+g)\omega'\mathrm{sgn}(\omega')\end{aligned} \tag{A.26}$$

If we perform the δ-integral over $d\overline{\varepsilon}$ we have that $\omega-\omega'-\overline{\varepsilon}-g=0\Rightarrow\overline{\varepsilon}=\omega-\omega'-g$. On the other hand, the argument of the δ-function must lie into the interval of integration, so we have that $\omega-\omega'-g>-\varepsilon\Rightarrow\varepsilon>\omega'+g-\omega$ and we have:

$$\mathrm{Im}\Sigma^{(2)}(\vec{\mathbf{k}},\omega)=\frac{3U^2}{64\sqrt{2}\pi^3}\frac{sgn(\beta)}{v_F^2\beta}\int_{-\Lambda}^{\Lambda}d\omega'\int_{\omega'+g-\omega}^{\omega'}d\varepsilon\frac{\omega'\mathrm{sgn}(\omega-\omega')\mathrm{sgn}(\omega')}{\sqrt{\omega'-\varepsilon}\sqrt{\omega-\omega'-g+\varepsilon}} \tag{A.27}$$

The integral in $d\varepsilon$ for ω and g positives is:

$$\int_{\omega'-\omega+g}^{\omega'}\frac{d\varepsilon}{\sqrt{(\omega'-\varepsilon)(\omega-\omega'-g+\varepsilon)}}=\pi \tag{A.28}$$

The remain integral in frequencies would be:

$$A\pi\int_{-\Lambda}^{\Lambda}d\omega'\omega'\mathrm{sgn}(\omega-\omega')\mathrm{sgn}(\omega') \tag{A.29}$$

$$=A\pi\left[-\int_{-\Lambda}^{-\omega}d\omega'\omega'-\int_{-\omega}^{0}d\omega'\omega'+\int_{0}^{\omega}d\omega'\omega'-\int_{\omega}^{\Lambda}d\omega'\omega'\right] \tag{A.30}$$

$$=A\pi\omega^2 \tag{A.31}$$

where $A=\frac{3U^2}{64\sqrt{2}\pi^3}\frac{\mathrm{sgn}(\beta)}{v_F^2\beta}$. Finally we have for the imaginary part of the self-energy:

$$\mathrm{Im}\Sigma^{(2)}(\vec{\mathbf{k}},\omega)=\frac{3}{64}\frac{U^2}{\sqrt{2}\pi^2}\frac{\mathrm{sgn}(\beta)}{v_F^2\beta}\omega^2 \tag{A.32}$$

.

Appendix B

Appendix to Chapter 4

B.1 Integration regions

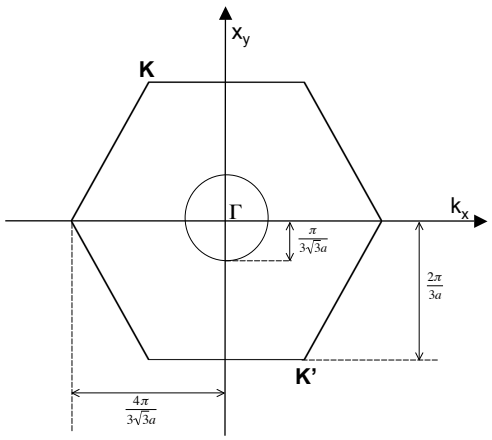

Figure B.1: Integration region in the Brilloin zone.

To study the Fermi line renormalization of a doped graphene sheet with chemical potential μ due to the exchange self-energy, we compute Eq.(4.11) numerically. In order to take into account the two limits of Coulomb interaction (short and long range), we divide the integral in Eq.(4.11) into two parts:

- One for the low momenta region of the Brillouin zone, around the Γ point, where $V_{\vec{\mathbf{q}}}$ in Eq.(**??**) is just the Fourier transform of the Coulomb interction in 2D $V_{\vec{\mathbf{q}}} = 2\pi e_0^2/q$. Here we are studying a long range Coulomb interaction and the symmetry of the lattice does not affect the form of the interaction

itself. This is valid for low $\vec{\mathbf{q}}$ values, what correspond to large $\vec{\mathbf{r}} = \vec{\mathbf{r}}_1 - \vec{\mathbf{r}}_2$ vectors in real space. We use this limit for the circular region $0 \leq |\vec{\mathbf{q}}| \leq \frac{1}{3}\frac{\pi}{\sqrt{3}a}$.

- If $|\vec{\mathbf{q}}| \geq \frac{1}{3}\frac{\pi}{\sqrt{3}a}$, then we use $V_{\vec{\mathbf{q}}} = 2V\left(\cos\left(\vec{\mathbf{q}}\cdot\vec{\tau}_2\right) + \cos\left(\vec{\mathbf{q}}\cdot D_3\vec{\tau}_2\right) + \cos\left(\vec{\mathbf{q}}\cdot D_3^{-1}\vec{\tau}_2\right)\right)$ that corresponds to a short range Coulomb repulsion where the full symmetry of the hexagonal lattice appears in the Fourier transform of the Coulomb interaction.

These integration region can be seen in Fig.[B.1]. Of course this is a very rugh approximation, although it is a good starting point to study the full range Coulomb interaction.

B.2 Self-energy correction due to a long range Coulomb interaction: beyond the linear approximation around the K point

For a weakly doped graphene layer, one can expand $g(\vec{\mathbf{k}})$ around a Dirac point (for example around $K = \left(4\pi/3\sqrt{3}a, 0\right)$ and around $K' = \left(-4\pi/3\sqrt{3}a, 0\right)$) and see that

$$g(\vec{\mathbf{k}}) \approx \begin{cases} \frac{3}{2}a(k_x + \imath k_y) - \frac{3}{8}a^2(k_x - \imath k_y)^2 & around\ \ K \\ -\frac{3}{2}a(k_x - \imath k_y) - \frac{3}{8}a^2(k_x + \imath k_y)^2 & around\ \ K' \end{cases} \tag{B.1}$$

and diagonalizing the 4×4 matrix we find the simplified dispersion relation

$$\epsilon_{\lambda,v}(\vec{\mathbf{k}}) \approx \lambda\frac{3}{2}at\sqrt{k^2 + \frac{1}{16}a^2k^4 - v\frac{1}{2}a(k_x^3 - 3k_xk_y^2)} \tag{B.2}$$

where again $\lambda = +, -$ for the conduction and valence band and $v = +, -$ for valley $\mathbf{K}$ and $\mathbf{K}'$ respectively. Being the Dirac point at $E_D = 0$, if we dope the system with electrons, then $\mu > 0$ and the Fermi line lies on the conduction band, while $\mu < 0$ for a hole doped system and with Fermi line on the valence band.

In this case we can write the exchange self-energy (diagram B.2) for a long range Coulomb interaction (long wavelength limit, with $q/2k_F \ll 1$) for which $V_c(\vec{\mathbf{k}} - \vec{\mathbf{k}}') = 2\pi e_0^2/|\vec{\mathbf{k}} - \vec{\mathbf{k}}'|$, using Eq.(4.11)

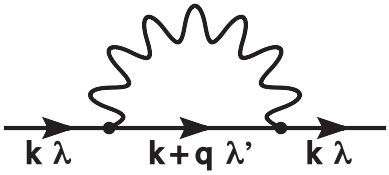

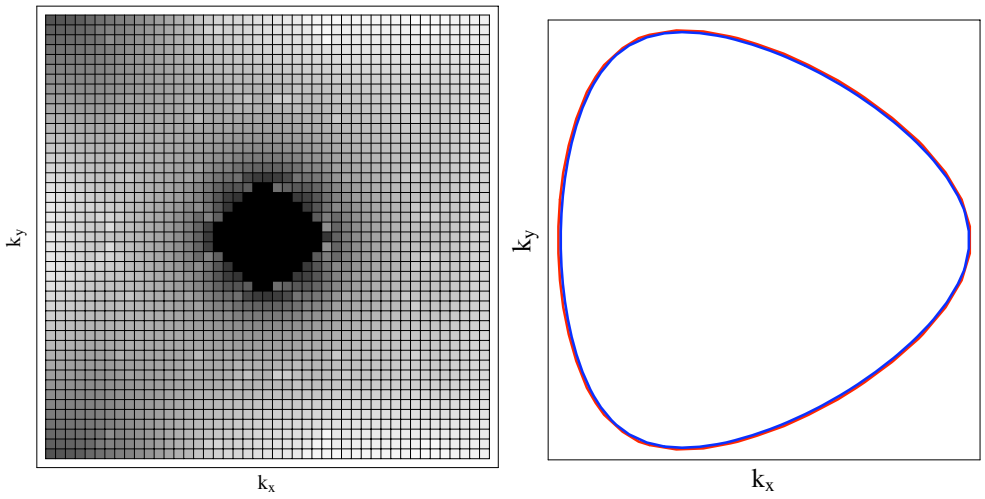

(a) (b)

Figure B.2: (a) Density plot of the self-energy obtained around the **K** point according to Eq.(B.3). The dark regions are the ones with stronger correction. (b) Non-interacting (blue) and interacting (red) Fermi lines around the **K** point for a doped graphene layer with $\mu \approx 2eV$.

$$\begin{aligned}\Sigma^x_\lambda(\vec{\mathbf{k}}) &= -\sum_{\lambda'}\int_\Lambda \frac{d\vec{\mathbf{q}}}{(2\pi)^2} V_c(\vec{\mathbf{q}}) F_{\lambda\lambda'}(\vec{\mathbf{k}},\vec{\mathbf{k}}+\vec{\mathbf{q}})\Theta(-\xi_{\lambda'}(\vec{\mathbf{k}}+\vec{\mathbf{q}})) \\ &= -\sum_{\lambda'}\int_\Lambda \frac{d^2q}{(2\pi)^2}\frac{2\pi e_0^2}{\sqrt{q_x^2+q_y^2}}\frac{1+\lambda\lambda'\cos\phi_{\vec{\mathbf{k}},\vec{\mathbf{k}}+\vec{\mathbf{q}}}}{2}\Theta(\mu-\epsilon_{\lambda'}(\vec{\mathbf{k}}+\vec{\mathbf{q}}))\end{aligned} \tag{B.3}$$

where we have also approximated the wave funtion Eq.(4.4) for its approximation near the Dirac points (see the Appendix B.3.2 for more details) in such a form that the overlap term can be simply expressed by $F_{\lambda,\lambda'}(\vec{\mathbf{k}},\vec{\mathbf{k}}') = \frac{1}{2}(1+\lambda\lambda'\cos\phi_{\vec{\mathbf{k}},\vec{\mathbf{k}}'})$. Notice that we have restricted the avalaible phase space to $|\epsilon_\lambda(\vec{\mathbf{k}})| \leq \Lambda$, where $\Lambda \approx 2.4eV$ that is the limit of validity of our expansion, and plays the role of cutoff in the valence band. In this approximation we are also considering only intra-valley scattering processes ($v = 1$) that are the kind of processes expected near half filling for a long range interaction.

The results obtained for a filling $\mu \approx 2eV$ are shown in Fig.[B.2(b)]. Here we can see how the non-interacting Fermi line (blue line) is renormalized by the electronic Coulomb interactions to the dressed Fermi line (red line). We can see that there is not appreciable renormalization of the Fermi line due to long range interaction effects. The only appreciable renormalization of the chemical

potential is seen at very low dopings, although no renormalization of the Fermi line shape is obtained due to the circular symmetry of the self-energy.

B.3 Matrix element of the Coulomb interaction

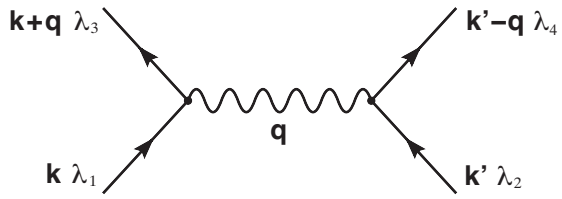

Figure B.3: Coulomb interacting vertex.

The matrix elements due to the Coulomb interaction represented in Fig.[B.3] $\langle\vec{\mathbf{k}},\lambda_1;\vec{\mathbf{k}}',\lambda_2|V_C|\vec{\mathbf{k}}+\vec{\mathbf{q}},\lambda_3;\vec{\mathbf{k}}'-\vec{\mathbf{q}},\lambda_4\rangle$ are

$$\begin{aligned} v_{\lambda_1\lambda_2\lambda_3\lambda_4}(\vec{\mathbf{k}},\vec{\mathbf{k}}';\vec{\mathbf{q}}) &= \langle\vec{\mathbf{k}},\lambda_1;\vec{\mathbf{k}}'\lambda_2|V_C|\vec{\mathbf{k}}+\vec{\mathbf{q}},\lambda_3;\vec{\mathbf{k}}'-\vec{\mathbf{q}},\lambda_4\rangle \\ &= \int d\vec{\mathbf{r}}_1\int d\vec{\mathbf{r}}_2\langle\Psi_{\vec{\mathbf{k}},\lambda_1}(\vec{\mathbf{r}}_1)|\langle\Psi_{\vec{\mathbf{k}}',\lambda_2}(\vec{\mathbf{r}}_2)|\frac{e_0^2}{|\vec{\mathbf{r}}_1-\vec{\mathbf{r}}_2|}|\Psi_{\vec{\mathbf{k}}'-\vec{\mathbf{q}},\lambda_4}(\vec{\mathbf{r}}_2)\rangle|\Psi_{\vec{\mathbf{k}}+\vec{\mathbf{q}},\lambda_3}(\vec{\mathbf{r}}_1)\rangle \end{aligned} \tag{B.4}$$

B.3.1 Short range interaction

If we only take into account the Coulomb interaction due to nearest neighbor electronic repulsion, we have that

$$V(\vec{\mathbf{r}}_1-\vec{\mathbf{r}}_2)=\begin{cases} V=\frac{e_0^2}{a}\,if & |\vec{\mathbf{r}}_1-\vec{\mathbf{r}}_2|=a \\ 0 & otherwise \end{cases} \tag{B.5}$$

in this case, for a fixed $\vec{\mathbf{r}}_1$ belonging to the A sublattice, in Fig.4.1(a) we can see tha the values of $\vec{\mathbf{r}}_2$ that gives a finite contribution are the three vectors that connect $\vec{\mathbf{r}}_1$ with its nearest neighbor

$$\vec{\mathbf{r}}_2=\begin{cases} \vec{\mathbf{r}}_1+\quad\vec{\tau}_2 \\ \vec{\mathbf{r}}_1+D_3\vec{\tau}_2 \\ \vec{\mathbf{r}}_1+D_3^{-1}\vec{\tau}_2 \end{cases} \tag{B.6}$$

On the other hand, if $\vec{\mathbf{r}}_1$ belongs to the B sublattice, its nearest neighbor will be defined by the vecotors

$$\vec{\mathbf{r}}_2 = \begin{cases} \vec{\mathbf{r}}_1 - \quad \vec{\tau}_2 \\ \vec{\mathbf{r}}_1 - D_3\vec{\tau}_2 \\ \vec{\mathbf{r}}_1 - D_3^{-1}\vec{\tau}_2 \end{cases} \tag{B.7}$$

we can write then

$$\begin{aligned} v_{\lambda_1\lambda_2\lambda_3\lambda_4}(\vec{\mathbf{k}},\vec{\mathbf{k}}';\vec{\mathbf{q}}) = \frac{e_0^2}{a}\int d\vec{\mathbf{r}}_1 \quad & \langle\Psi_{\vec{\mathbf{k}},\lambda_1}(\vec{\mathbf{r}}_1)|\Psi_{\vec{\mathbf{k}}+\vec{\mathbf{q}},\lambda_3}(\vec{\mathbf{r}}_1)\rangle \\ & \times\Big[\langle\Psi_{\vec{\mathbf{k}}',\lambda_2}(\vec{\mathbf{r}}_1\pm\vec{\tau}_2)|\Psi_{\vec{\mathbf{k}}'-\vec{\mathbf{q}},\lambda_4}(\vec{\mathbf{r}}_1\pm\vec{\tau}_2)\rangle \\ & \quad +\langle\Psi_{\vec{\mathbf{k}}',\lambda_2}(\vec{\mathbf{r}}_1\pm D_3\vec{\tau}_2)|\Psi_{\vec{\mathbf{k}}'-\vec{\mathbf{q}},\lambda_4}(\vec{\mathbf{r}}_1\pm D_3\vec{\tau}_2)\rangle \\ & \quad +\langle\Psi_{\vec{\mathbf{k}}',\lambda_2}(\vec{\mathbf{r}}_1\pm D_3^{-1}\vec{\tau}_2)|\Psi_{\vec{\mathbf{k}}'-\vec{\mathbf{q}},\lambda_4}(\vec{\mathbf{r}}_1\pm D_3^{-1}\vec{\tau}_2)\rangle\Big] \end{aligned}$$

Using the periodicity properties of the Bloch functions $|\Psi_{\vec{\mathbf{k}},\lambda}(\vec{\mathbf{r}}+\vec{\mathbf{R}})\rangle = e^{\imath\vec{\mathbf{k}}\cdot\vec{\mathbf{R}}}|\Psi_{\vec{\mathbf{k}},\lambda}(\vec{\mathbf{r}})\rangle$, where $\vec{\mathbf{R}}$ is a vector of the lattice, we can have

$$\begin{aligned} v_{\lambda_1\lambda_2\lambda_3\lambda_4}(\vec{\mathbf{k}},\vec{\mathbf{k}}';\vec{\mathbf{q}}) = \frac{e_0^2}{a}\int d\vec{\mathbf{r}}_1 \quad & \langle\Psi_{\vec{\mathbf{k}},\lambda_1}(\vec{\mathbf{r}}_1)|\Psi_{\vec{\mathbf{k}}+\vec{\mathbf{q}},\lambda_3}(\vec{\mathbf{r}}_1)\rangle \\ & \times\Big[\langle\Psi_{\vec{\mathbf{k}}',\lambda_2}(\vec{\mathbf{r}}_1)|e^{-\imath\vec{\mathbf{k}}'\cdot\vec{\tau}_2}e^{\imath(\vec{\mathbf{k}}'-\vec{\mathbf{q}})\cdot\vec{\tau}_2}|\Psi_{\vec{\mathbf{k}}'-\vec{\mathbf{q}},\lambda_4}(\vec{\mathbf{r}}_1)\rangle \\ & \quad +\langle\Psi_{\vec{\mathbf{k}}',\lambda_2}(\vec{\mathbf{r}}_1)|e^{-\imath\vec{\mathbf{k}}'\cdot D_3\vec{\tau}_2}e^{\imath(\vec{\mathbf{k}}'-\vec{\mathbf{q}})\cdot D_3\vec{\tau}_2}|\Psi_{\vec{\mathbf{k}}'-\vec{\mathbf{q}},\lambda_4}(\vec{\mathbf{r}}_1)\rangle \\ & \quad +\langle\Psi_{\vec{\mathbf{k}}',\lambda_2}(\vec{\mathbf{r}}_1)|e^{-\imath\vec{\mathbf{k}}'\cdot D_3^{-1}\vec{\tau}_2}e^{\imath(\vec{\mathbf{k}}'-\vec{\mathbf{q}})\cdot D_3^{-1}\vec{\tau}_2}|\Psi_{\vec{\mathbf{k}}'-\vec{\mathbf{q}},\lambda_4}(\vec{\mathbf{r}}_1)\rangle \\ & \quad +\langle\Psi_{\vec{\mathbf{k}}',\lambda_2}(\vec{\mathbf{r}}_1)|e^{\imath\vec{\mathbf{k}}'\cdot\vec{\tau}_2}e^{-\imath(\vec{\mathbf{k}}'-\vec{\mathbf{q}})\cdot\vec{\tau}_2}|\Psi_{\vec{\mathbf{k}}'-\vec{\mathbf{q}},\lambda_4}(\vec{\mathbf{r}}_1)\rangle \\ & \quad +\langle\Psi_{\vec{\mathbf{k}}',\lambda_2}(\vec{\mathbf{r}}_1)|e^{\imath\vec{\mathbf{k}}'\cdot D_3\vec{\tau}_2}e^{-\imath(\vec{\mathbf{k}}'-\vec{\mathbf{q}})\cdot D_3\vec{\tau}_2}|\Psi_{\vec{\mathbf{k}}'-\vec{\mathbf{q}},\lambda_4}(\vec{\mathbf{r}}_1)\rangle \\ & \quad +\langle\Psi_{\vec{\mathbf{k}}',\lambda_2}(\vec{\mathbf{r}}_1)|e^{\imath\vec{\mathbf{k}}'\cdot D_3^{-1}\vec{\tau}_2}e^{-\imath(\vec{\mathbf{k}}'-\vec{\mathbf{q}})\cdot D_3^{-1}\vec{\tau}_2}|\Psi_{\vec{\mathbf{k}}'-\vec{\mathbf{q}},\lambda_4}(\vec{\mathbf{r}}_1)\rangle\Big] \end{aligned} \tag{B.8}$$

and

$$\begin{aligned} v_{\lambda_1\lambda_2\lambda_3\lambda_4}(\vec{\mathbf{k}},\vec{\mathbf{k}}';\vec{\mathbf{q}}) &= \frac{e_0^2}{a}\int d\vec{\mathbf{r}}_1\langle\Psi_{\vec{\mathbf{k}},\lambda_1}(\vec{\mathbf{r}}_1)|\Psi_{\vec{\mathbf{k}}+\vec{\mathbf{q}},\lambda_3}(\vec{\mathbf{r}}_1)\rangle\langle\Psi_{\vec{\mathbf{k}}',\lambda_2}(\vec{\mathbf{r}}_1)|\Psi_{\vec{\mathbf{k}}'-\vec{\mathbf{q}},\lambda_4}(\vec{\mathbf{r}}_1)\rangle \\ &\quad\times\left(e^{-\imath\vec{\mathbf{q}}\cdot\vec{\tau}_2}+e^{-\imath\vec{\mathbf{q}}\cdot D_3\vec{\tau}_2}+e^{-\imath\vec{\mathbf{q}}\cdot D_3^{-1}\vec{\tau}_2}+e^{\imath\vec{\mathbf{q}}\cdot\vec{\tau}_2}+e^{\imath\vec{\mathbf{q}}\cdot D_3\vec{\tau}_2}+e^{\imath\vec{\mathbf{q}}\cdot D_3^{-1}\vec{\tau}_2}\right) \\ &= \frac{e_0^2}{a}(g^*(\vec{\mathbf{q}})+g(\vec{\mathbf{q}}))\int d\vec{\mathbf{r}}_1\langle\Psi_{\vec{\mathbf{k}},\lambda_1}(\vec{\mathbf{r}}_1)|\Psi_{\vec{\mathbf{k}}+\vec{\mathbf{q}},\lambda_3}(\vec{\mathbf{r}}_1)\rangle\langle\Psi_{\vec{\mathbf{k}}',\lambda_2}(\vec{\mathbf{r}}_1)|\Psi_{\vec{\mathbf{k}}'-\vec{\mathbf{q}},\lambda_4}(\vec{\mathbf{r}}_1)\rangle \end{aligned}$$

where $g(\vec{\mathbf{q}}) = \left(e^{\imath\vec{\mathbf{q}}\cdot\vec{\tau}_2}+e^{\imath\vec{\mathbf{q}}\cdot D_3\vec{\tau}_2}+e^{\imath\vec{\mathbf{q}}\cdot D_3^{-1}\vec{\tau}_2}\right)$ and finally

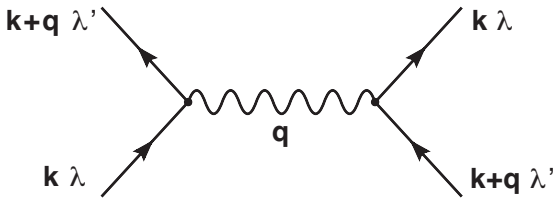

$$v_{\lambda_1\lambda_2\lambda_3\lambda_4}(\vec{\mathbf{k}},\vec{\mathbf{k}}';\vec{\mathbf{q}}) = V(\vec{\mathbf{q}})F_{\lambda_1\lambda_2\lambda_3\lambda_4}(\vec{\mathbf{k}},\vec{\mathbf{k}}';\vec{\mathbf{q}}) \tag{B.9}$$

where $V(\vec{\mathbf{q}}) = V(g(\vec{\mathbf{q}})+g^*(\vec{\mathbf{q}})) = 2\left(\cos\left(\vec{\mathbf{q}}\cdot\vec{\tau}_2\right)+\cos\left(\vec{\mathbf{q}}\cdot D_3\vec{\tau}_2\right)+\cos\left(\vec{\mathbf{q}}\cdot D_3^{-1}\vec{\tau}_2\right)\right)$ with $V = e_0^2/a$ and the overlap between eigenfunctions is taken into account by the term

$$F_{\lambda_1\lambda_2\lambda_3\lambda_4}(\vec{\mathbf{k}},\vec{\mathbf{k}}';\vec{\mathbf{q}}) = \int d\vec{\mathbf{r}}\langle\Psi_{\vec{\mathbf{k}},\lambda_1}(\vec{\mathbf{r}})|\Psi_{\vec{\mathbf{k}}+\vec{\mathbf{q}},\lambda_3}(\vec{\mathbf{r}})\rangle\langle\Psi_{\vec{\mathbf{k}}',\lambda_2}(\vec{\mathbf{r}})|\Psi_{\vec{\mathbf{k}}'-\vec{\mathbf{q}},\lambda_4}(\vec{\mathbf{r}})\rangle \tag{B.10}$$

This term is simplified for the Coulomb interaction that enters in the exchange self-energy diagram studied in this problem, shown in Fig.4.3(a). For this case, the vertex Fig.B.3 reduce to the diagram shown in Fig.B.3.1, where $\vec{\mathbf{k}}' = \vec{\mathbf{k}}+\vec{\mathbf{q}}$ and $F_{\lambda_1\lambda_2\lambda_3\lambda_4}(\vec{\mathbf{k}},\vec{\mathbf{k}}';\vec{\mathbf{q}}) \to F_{\lambda\lambda'}(\vec{\mathbf{k}},\vec{\mathbf{k}}+\vec{\mathbf{q}})$ with

$$F_{\lambda\lambda'}(\vec{\mathbf{k}},\vec{\mathbf{k}}+\vec{\mathbf{q}}) = \int d\vec{\mathbf{r}}\langle\Psi_{\vec{\mathbf{k}},\lambda}(\vec{\mathbf{r}})|\Psi_{\vec{\mathbf{k}}+\vec{\mathbf{q}},\lambda'}(\vec{\mathbf{r}})\rangle\langle\Psi_{\vec{\mathbf{k}}+\vec{\mathbf{q}},\lambda'}(\vec{\mathbf{r}})|\Psi_{\vec{\mathbf{k}},\lambda}(\vec{\mathbf{r}})\rangle \tag{B.11}$$

or

$$F_{\lambda\lambda'}(\vec{\mathbf{k}},\vec{\mathbf{k}}+\vec{\mathbf{q}}) = \int d\vec{\mathbf{r}}\left|\langle\Psi_{\vec{\mathbf{k}},\lambda}(\vec{\mathbf{r}})|\Psi_{\vec{\mathbf{k}}+\vec{\mathbf{q}},\lambda'}(\vec{\mathbf{r}})\rangle\right|^2 \tag{B.12}$$

B.3.2 Long range interaction

In this case, the matrix elements of diagram shown in Fig.B.3.1 are, using the change $\vec{\mathbf{r}}_1 - \vec{\mathbf{r}}_2 = \vec{\mathbf{r}}$

$$\begin{aligned}
v_{\lambda,\lambda'}(\vec{\mathbf{k}},\vec{\mathbf{k}}+\vec{\mathbf{q}}) &= \int d\vec{\mathbf{r}}_1\int d\vec{\mathbf{r}}\langle\Psi_{\vec{\mathbf{k}},\lambda}(\vec{\mathbf{r}}_1)|\langle\Psi_{\vec{\mathbf{k}}+\vec{\mathbf{q}},\lambda'}(\vec{\mathbf{r}}_1-\vec{\mathbf{r}})|\frac{e_0^2}{r}|\Psi_{\vec{\mathbf{k}},\lambda}(\vec{\mathbf{r}}_1-\vec{\mathbf{r}})\rangle|\Psi_{\vec{\mathbf{k}}+\vec{\mathbf{q}},\lambda'}(\vec{\mathbf{r}}_1)\rangle \\
&= \int d\vec{\mathbf{r}}_1\langle\Psi_{\vec{\mathbf{k}},\lambda}(\vec{\mathbf{r}}_1)|\langle\Psi_{\vec{\mathbf{k}}+\vec{\mathbf{q}},\lambda'}(\vec{\mathbf{r}}_1)|\int d\vec{\mathbf{r}}\frac{e_0^2}{r}e^{\imath\vec{\mathbf{q}}\cdot\vec{\mathbf{r}}}|\Psi_{\vec{\mathbf{k}},\lambda}(\vec{\mathbf{r}}_1)\rangle|\Psi_{\vec{\mathbf{k}}+\vec{\mathbf{q}},\lambda'}(\vec{\mathbf{r}}_1)\rangle \\
&= V_{\vec{\mathbf{q}}}\int d\vec{\mathbf{r}}_1|\langle\Psi_{\vec{\mathbf{k}},\lambda}(\vec{\mathbf{r}}_1)|\Psi_{\vec{\mathbf{k}}+\vec{\mathbf{q}},\lambda'}(\vec{\mathbf{r}}_1)\rangle|^2 \\
&= V_{\vec{\mathbf{q}}}F_{\lambda\lambda'}(\vec{\mathbf{k}},\vec{\mathbf{k}}+\vec{\mathbf{q}}) \qquad \text{(B.13)} \\
& \qquad \text{(B.14)}
\end{aligned}$$

where we have used the Fourier transform of the 2D Coulomb potential

$$V_{\vec{\mathbf{q}}} = \int d\vec{\mathbf{r}} \frac{e_0^2}{r} e^{\imath \vec{\mathbf{q}} \cdot \vec{\mathbf{r}}} = 2\pi \frac{e_0^2}{q} \tag{B.15}$$

and the overlap wave-function is defined as

$$F_{\lambda\lambda'}(\vec{\mathbf{k}}, \vec{\mathbf{k}} + \vec{\mathbf{q}}) = \int d\vec{\mathbf{r}}_1 |\langle \Psi_{\vec{\mathbf{k}},\lambda}(\vec{\mathbf{r}}_1) | \Psi_{\vec{\mathbf{k}}+\vec{\mathbf{q}},\lambda'}(\vec{\mathbf{r}}_1) \rangle|^2 \tag{B.16}$$

Wave function overlap near half-filling.

Near the Dirac points the wave function has the form

$$\Psi_{\vec{\mathbf{k}},\lambda}(\vec{\mathbf{r}}) = \begin{pmatrix} \psi_a(\vec{\mathbf{r}}) \\ \psi_b(\vec{\mathbf{r}}) \end{pmatrix} = \frac{e^{\imath \vec{\mathbf{k}} \cdot \vec{\mathbf{r}}}}{\sqrt{2}} \begin{pmatrix} e^{\imath \phi_{\vec{\mathbf{k}}}/2} \\ \lambda e^{-\imath \phi_{\vec{\mathbf{k}}}/2} \end{pmatrix} \tag{B.17}$$

where $\phi_{\vec{\mathbf{k}}} = \arctan(k_y/k_x)$. In this case, the braket $\langle \Psi_{\vec{\mathbf{k}},\lambda}(\vec{\mathbf{r}}_1) | \Psi_{\vec{\mathbf{k}}+\vec{\mathbf{q}},\lambda'}(\vec{\mathbf{r}}_1) \rangle$ is

$$\begin{aligned} \langle \Psi_{\vec{\mathbf{k}},\lambda}(\vec{\mathbf{r}}) | \Psi_{\vec{\mathbf{k}}+\vec{\mathbf{q}},\lambda'}(\vec{\mathbf{r}}) \rangle &= \frac{e^{-\imath \vec{\mathbf{k}} \cdot \vec{\mathbf{r}}}}{\sqrt{2}} \left(e^{-\imath \phi_{\vec{\mathbf{k}}}/2} \, \lambda e^{\imath \phi_{\vec{\mathbf{k}}}/2} \right) \frac{e^{\imath (\vec{\mathbf{k}}+\vec{\mathbf{q}}) \cdot \vec{\mathbf{r}}}}{\sqrt{2}} \begin{pmatrix} e^{\imath \phi_{\vec{\mathbf{k}}+\vec{\mathbf{q}}}/2} \\ \lambda' e^{-\imath \phi_{\vec{\mathbf{k}}+\vec{\mathbf{q}}}/2} \end{pmatrix} \\ &= \frac{1}{2} e^{\imath \vec{\mathbf{q}} \cdot \vec{\mathbf{r}}} \left(e^{\imath (\phi_{\vec{\mathbf{k}}+\vec{\mathbf{q}}} - \phi_{\vec{\mathbf{k}}})/2} + \lambda\lambda' e^{-\imath (\phi_{\vec{\mathbf{k}}+\vec{\mathbf{q}}} - \phi_{\vec{\mathbf{k}}})/2} \right) \qquad \text{(B.18)} \\ & \qquad \text{(B.19)} \end{aligned}$$

and, renaming $\phi_{\vec{\mathbf{k}}+\vec{\mathbf{q}}} - \phi_{\vec{\mathbf{k}}} = \phi_{\vec{\mathbf{k}},\vec{\mathbf{k}}+\vec{\mathbf{q}}}$, we obtain the widely used result for $|\langle \Psi_{\vec{\mathbf{k}},\lambda}(\vec{\mathbf{r}}_1) | \Psi_{\vec{\mathbf{k}}+\vec{\mathbf{q}},\lambda'}(\vec{\mathbf{r}}_1) \rangle|^2$

$$\begin{aligned} |\langle \Psi_{\vec{\mathbf{k}},\lambda}(\vec{\mathbf{r}}_1) | \Psi_{\vec{\mathbf{k}}+\vec{\mathbf{q}},\lambda'}(\vec{\mathbf{r}}_1) \rangle|^2 &= \frac{1}{4} e^{-\imath \vec{\mathbf{q}} \cdot \vec{\mathbf{r}}} (e^{-\imath \phi_{\vec{\mathbf{k}},\vec{\mathbf{k}}+\vec{\mathbf{q}}}/2} + \lambda\lambda' e^{\imath \phi_{\vec{\mathbf{k}},\vec{\mathbf{k}}+\vec{\mathbf{q}}}/2}) e^{\imath \vec{\mathbf{q}} \cdot \vec{\mathbf{r}}} (e^{\imath \phi_{\vec{\mathbf{k}},\vec{\mathbf{k}}+\vec{\mathbf{q}}}/2} + \lambda\lambda' e^{-\imath \phi_{\vec{\mathbf{k}},\vec{\mathbf{k}}+\vec{\mathbf{q}}}/2}) \\ &= \frac{1}{4} \left(1 + \lambda\lambda' e^{-\imath \phi_{\vec{\mathbf{k}},\vec{\mathbf{k}}+\vec{\mathbf{q}}}} + \lambda\lambda' e^{\imath \phi_{\vec{\mathbf{k}},\vec{\mathbf{k}}+\vec{\mathbf{q}}}} + (\lambda\lambda')^2 \right) \\ &= \frac{1 + \lambda\lambda' \cos \phi_{\vec{\mathbf{k}},\vec{\mathbf{k}}+\vec{\mathbf{q}}}}{2} \end{aligned} \tag{B.20}$$

B.4 Interacting hamiltonian in reciprocal space.

In general, we can express the Coulomb interating hamiltonian as

$$\mathcal{H}_{int} = \sum_{i_s j_{s'}; \sigma, \sigma'} V_{i_s j_{s'}} n_{i_s \sigma} n_{j_{s'} \sigma'} \tag{B.21}$$

where $i \in \{1, ..., N\}$ is the cell index, s is the sublattice index inside each unit cell (for each cell index i we have two sites indices $i_s = \{i_A, i_B\}$) and σ is the spin

label $\sigma = \{\uparrow, \downarrow\}$. With this notation, $n_{i_s\sigma}$ is the number of electrons with spin σ on the cell i with sublattice index s, and $V_{i_s j_{s'}} = e^2/|\vec{\mathbf{r}}_{i_s} - \vec{\mathbf{r}}_{j'_s}|$ is the Coulomb repulsion between electrons in sites i_s and $j_{s'}$.

The Fourier transform of the creation and destruction operators is

$$c^\dagger_{i_s\sigma} = \frac{1}{\sqrt{N}} \sum_{\vec{\mathbf{k}}} e^{-\imath \vec{\mathbf{k}}\cdot\vec{\mathbf{r}}_{i_s}} c^\dagger_{\vec{\mathbf{k}}\sigma}$$

$$c_{i_s\sigma} = \frac{1}{\sqrt{N}} \sum_{\vec{\mathbf{k}}} e^{\imath \vec{\mathbf{k}}\cdot\vec{\mathbf{r}}_{i_s}} c_{\vec{\mathbf{k}}\sigma} \tag{B.22}$$

(B.23)

We give the expression of the short range Coulomb interaction up to next-nearest neighbor:

$$\mathcal{H}_{int} = \mathcal{H}_U + \mathcal{H}_V + \mathcal{H}_{V'} \tag{B.24}$$

The local Hubbard term in the real space

$$\mathcal{H}_U = \sum_{i,s} U c^\dagger_{i_s\uparrow} c^\dagger_{i_s\downarrow} c_{i_s\downarrow} c_{i_s\uparrow} \tag{B.25}$$

transforms to the momentum space, using Eq.(B.22), as

$$\mathcal{H}_U = 2\frac{U}{N} \sum_{\vec{\mathbf{k}},\vec{\mathbf{p}},\vec{\mathbf{q}}} c^\dagger_{\vec{\mathbf{k}}\uparrow} c^\dagger_{\vec{\mathbf{p}}\downarrow} c_{\vec{\mathbf{p}}+\vec{\mathbf{q}}\downarrow} c_{\vec{\mathbf{k}}-\vec{\mathbf{q}}\uparrow}$$

The next nearest neighbor interaction

$$\mathcal{H}_V = \sum_{\langle i_s j_{s'}\rangle} \sum_{\sigma,\sigma'=\uparrow,\downarrow} V c^\dagger_{i_s\sigma} c^\dagger_{j_{s'}\sigma'} c_{j_{s'}\sigma'} c_{i_s\sigma} \tag{B.26}$$

can be similarly transformed to

$$\mathcal{H}_V = \frac{V}{N^2} \sum_{\sigma\sigma'} \sum_{\vec{\mathbf{k}},\vec{\mathbf{p}},\vec{\mathbf{q}}} 2\left(\cos\left(\vec{\mathbf{q}}\cdot\vec{\tau}_2\right) + \cos\left(\vec{\mathbf{q}}\cdot D_3\vec{\tau}_2\right) + \cos\left(\vec{\mathbf{q}}\cdot D_3^{-1}\vec{\tau}_2\right)\right) c^\dagger_{\vec{\mathbf{k}}\sigma} c^\dagger_{\vec{\mathbf{p}}\sigma'} c_{\vec{\mathbf{p}}+\vec{\mathbf{q}}\sigma'} c_{\vec{\mathbf{k}}-\vec{\mathbf{q}}\sigma} \tag{B.27}$$

where we have used again that the nearest neigbor of an electron on site $\vec{\mathbf{r}}_{i_A}$ are

$$\vec{\mathbf{r}}_{j_B} = \begin{cases} \vec{\mathbf{r}}_{i_A} + \quad \vec{\tau}_2 \\ \vec{\mathbf{r}}_{i_A} + D_3\vec{\tau}_2 \\ \vec{\mathbf{r}}_{i_A} + D_3^{-1}\vec{\tau}_2 \end{cases} \tag{B.28}$$

Finally, the next nearest neighbor Coulomb interaction

$$\mathcal{H}_{V'} = \sum_{\langle\langle i_s j_s \rangle\rangle} \sum_{\sigma,\sigma'=\uparrow,\downarrow} \sum_{s=A,B} V' c^\dagger_{i_s\sigma} c^\dagger_{j_s\sigma'} c_{j_s\sigma'} c_{i_s\sigma} \tag{B.29}$$

transform to the momentum space as

$$\mathcal{H}_{V'} = 2\frac{V'}{N^2} \sum_{\sigma\sigma'} \sum_{\vec{\mathbf{k}},\vec{\mathbf{p}},\vec{\mathbf{q}}} \left(\cos\left(\vec{\mathbf{q}}\cdot\vec{\mathbf{a}}_1\right) + \cos\left(\vec{\mathbf{q}}\cdot\vec{\mathbf{a}}_2\right) + \cos\left(\vec{\mathbf{q}}\cdot(\vec{\mathbf{a}}_2-\vec{\mathbf{a}}_1)\right)\right) c^\dagger_{\vec{\mathbf{k}}\sigma} c^\dagger_{\vec{\mathbf{p}}\sigma'} c_{\vec{\mathbf{p}}+\vec{\mathbf{q}}\sigma'} c_{\vec{\mathbf{k}}-\vec{\mathbf{q}}\sigma} \tag{B.30}$$

where in this case the next nearest neigbor of an electron on site $\vec{\mathbf{r}}_{i_A}$ are

$$\vec{\mathbf{r}}_{j_A} = \begin{cases} \vec{\mathbf{r}}_{i_A} \pm \quad \vec{\mathbf{a}}_1 \\ \vec{\mathbf{r}}_{i_A} \pm \quad \vec{\mathbf{a}}_2 \\ \vec{\mathbf{r}}_{i_A} \pm (\vec{\mathbf{a}}_2 - \vec{\mathbf{a}}_1) \end{cases} \tag{B.31}$$

From the previous results, if we restrict the sum to next-nearest neighbors for the Coulomb interaction, which in the lattice space can be expressed, using the bipartite nature of the hexagonal lattice

$$\mathcal{H}_{int}(\vec{\mathbf{r}}) = \begin{pmatrix} \frac{e_0^2}{|\vec{\mathbf{r}}_{AA}|} & \frac{e_0^2}{|\vec{\mathbf{r}}_{AB}|} \\ \frac{e_0^2}{|\vec{\mathbf{r}}_{BA}|} & \frac{e_0^2}{|\vec{\mathbf{r}}_{BB}|} \end{pmatrix} \tag{B.32}$$

where $\vec{\mathbf{r}} = \vec{\mathbf{r}}_{AB}$ conects an atom of the A sublattice with one of the B sublattice and so forth. Within this notation $\mathcal{H}_{int}$ can be expressed in th reciprocal space as

$$\mathcal{H}_{int}(\vec{\mathbf{q}}) = \begin{pmatrix} U + V' f(\vec{\mathbf{q}}) & V g(\vec{\mathbf{q}}) \\ V g^*(\vec{\mathbf{q}}) & U + V' f(\vec{\mathbf{q}}) \end{pmatrix} \tag{B.33}$$

where $U = V_{i_s i_s}$ is the local Coulomb repulsion between two electrons with opposite spin in the same site of the lattice, $V = V_{i_s i_{s'}}$ is the nearest-neighbor repulsion (the repulstion between two electrons in the same unit cell but each of them in one different atom i_A and i_B), and finally $V' = V_{\langle i_s j_s \rangle}$ is the next-nearest neighbor repulsion, between two electrons of the same sublattice s but in consecutive unit cells i and j. The factor $g(\vec{\mathbf{q}})$ has been given above and (see Appendix for more details about the calculation)

$$f(\vec{\mathbf{q}}) = 2\cos(\vec{\mathbf{q}}\cdot\vec{\mathbf{a}}_1) + 2\cos(\vec{\mathbf{q}}\cdot\vec{\mathbf{a}}_2) + 2\cos(\vec{\mathbf{q}}\cdot(\vec{\mathbf{a}}_2-\vec{\mathbf{a}}_1)) \tag{B.34}$$

Appendix C

Appendix to Chapter 5

In this Appendix we give a detailed calculation of the mean field equations used in 5 for the most relevant cases.

C.1 Mean-field for $H = 0$

In this case we have that $\mathcal{H} = \mathcal{H}_1 + \mathcal{H}_2 + \mathcal{H}_{dist}$, where $\mathcal{H}_{eff} = \mathcal{H}_1 + \mathcal{H}_2$, with

$$\mathcal{H}_1 = J \sum_{i,\vec{\mathbf{a}}} \left[A(I^z_{i+\vec{\mathbf{a}}} + \eta_{\vec{\mathbf{a}}})(I^z_i + \eta_{\vec{\mathbf{a}}}) + B \right] \vec{\mathbf{S}}_{i+\vec{\mathbf{a}}} \cdot \vec{\mathbf{S}}_i \tag{C.1}$$

$$\mathcal{H}_2 = J \sum_{i,\vec{\mathbf{a}}} \left[C(I^z_{i+\vec{\mathbf{a}}} + \eta'_{\vec{\mathbf{a}}})(I^z_i + \eta'_{\vec{\mathbf{a}}}) + D \right] \tag{C.2}$$

As we have already mentioned, concerning the Heissemberg term in $\mathcal{H}_1$, and due to the rotationally invariance that we have for $H = 0$, we can treat $\vec{\mathbf{S}}_i$ as an Ising spin variable pointing in the z-direction:

$$\mathcal{H}_1 = J \sum_{i,\vec{\mathbf{a}}} \left[A(I^z_{i+\vec{\mathbf{a}}} + \eta_{\vec{\mathbf{a}}})(I^z_i + \eta_{\vec{\mathbf{a}}}) + B \right] S^z_{i+\vec{\mathbf{a}}} S^z \tag{C.3}$$

We define the mean-field order parameters for the z-component of the isospin:

$$\langle I^z_i \rangle = t_i = \begin{cases} t_A & \text{if} \quad i \in A \\ t_B & \text{if} \quad i \in B \end{cases} \tag{C.4}$$

and similarly for the z-component of the spin:

$$\langle S^z_i \rangle = m_i = \begin{cases} m_A & \text{if} \quad i \in A \\ m_B & \text{if} \quad i \in B \end{cases} \tag{C.5}$$

The mean-field decoupling for $\mathcal{H}_1$ reads:

$$\mathcal{H}_1 = J\sum_{i,\vec{\mathbf{a}}}\left\{A\left[(t_{i+\vec{\mathbf{a}}}+(I^z_{i+\vec{\mathbf{a}}}-t_{i+\vec{\mathbf{a}}}))(t_i+(I^z_i-t_i))+\eta_{\vec{\mathbf{a}}}(I_{i+\vec{\mathbf{a}}}+I^z_i)+\eta^2_{\vec{\mathbf{a}}}\right]+B\right\} \times\left(m_{i+\vec{\mathbf{a}}}+(S^z_{i+\vec{\mathbf{a}}}-m_{i+\vec{\mathbf{a}}})\right)(m_i+(S^z_i-m_i)) \tag{C.6}$$

Neglecting terms containing products of the form $(\Phi_i-\phi)(\Phi_j-\phi)$, where $\phi=\langle\Phi_i\rangle$ denotes the expected value for a given operator Φ, we end up with a term like:

$$\begin{aligned}\mathcal{H}_{1,MF} = J\sum_{i,\vec{\mathbf{a}}}\big[&A(-3t_it_{i+\vec{\mathbf{a}}}m_im_{i+\vec{\mathbf{a}}}+t_im_im_{i+\vec{\mathbf{a}}}I^z_{i+\vec{\mathbf{a}}}+t_{i+\vec{\mathbf{a}}}m_im_{i+\vec{\mathbf{a}}}I^z_i\\ &+t_it_{i+\vec{\mathbf{a}}}m_iS^z_{i+\vec{\mathbf{a}}}+t_it_{i+\vec{\mathbf{a}}}m_{i+\vec{\mathbf{a}}}S^z_i)\\ &+A\eta_{\vec{\mathbf{a}}}\left(-2t_{i+\vec{\mathbf{a}}}m_im_{i+\vec{\mathbf{a}}}-2t_im_im_{i+\vec{\mathbf{a}}}+(t_i+t_{i+\vec{\mathbf{a}}})m_iS^z_{i+\vec{\mathbf{a}}}\right.\\ &\left.+(t_i+t_{i+\vec{\mathbf{a}}})m_{i+\vec{\mathbf{a}}}S^z_i+m_im_{i+\vec{\mathbf{a}}}I^z_i+m_im_{i+\vec{\mathbf{a}}}I^z_{i+\vec{\mathbf{a}}}\right)\\ &(A\eta^2_{\vec{\mathbf{a}}}+B)(-m_im_{i+\vec{\mathbf{a}}}+m_iS^z_{i+\vec{\mathbf{a}}}+m^z_{i+\vec{\mathbf{a}}}S^z_i)\big]\end{aligned} \tag{C.7}$$

For the second term of the hamiltonian we have, working in the same way:

$$\mathcal{H}_{2,MF} = J\sum_{i,\vec{\mathbf{a}}}\left[C\left(-t_it_{i+\vec{\mathbf{a}}}+(t_i+\eta'_{\vec{\mathbf{a}}})I^z_{i+\vec{\mathbf{a}}}+(t_{i+\vec{\mathbf{a}}}+\eta'_{\vec{\mathbf{a}}})I^z_i+{\eta'_{\vec{\mathbf{a}}}}^2\right)+D\right] \tag{C.8}$$

We should notice that, due to the term $\mathcal{H}_{dist}$, which introduces a transverse field coupled to the isospin, we will have a finite uniform (ferro-orbital) component of the isospin in the x-direction as long as ε is finite. Using the expresion Eq.(5.17) we can calculate the partition function, that is composed by the orbital $\mathcal{Z}^t_i$ and magnetic $\mathcal{Z}^s_i$ one-particle partition function:

$$\mathcal{Z}^t_{i\in A,B} = Tr_ie^{-\beta\mathsf{H}^t_iI_i} \tag{C.9}$$

$$\mathcal{Z}^s_{i\in A,B} = Tr_ie^{-\beta\mathsf{H}^s_iS_i} \tag{C.10}$$

where the molecular field vectors that couples to the isospin and spin degrees of freedom are defined by[103]

$$\mathsf{H}^t(I_i) = (K\varepsilon,0,\mathsf{H}^{z,t}_1+\mathsf{H}^{z,t}_2) \tag{C.11}$$

$$\mathsf{H}^s(S_i) = (0,0,\mathsf{H}^{z,s}_1+\mathsf{H}^{z,s}_2) \tag{C.12}$$

where $\mathsf{H}^{z,t}_{1(2)}$ comes from the terms of $\mathcal{H}_{1(2),MF}$ coupled to the z-component of the isospin I^z_i, and $\mathsf{H}^{z,s}_{1(2)}$ comes from the terms of $\mathcal{H}_{1(2),MF}$ coupled to the z-component of the spin S^z_i. Then we have

$$\mathsf{H}^t(I_i) = \left(K\varepsilon, 0, \sum_{\vec{\mathbf{a}}} J\left[A\, t_{i+\vec{\mathbf{a}}} m_i m_{i+\vec{\mathbf{a}}} + A\, \eta_{\vec{\mathbf{a}}}\, m_i m_{i+\vec{\mathbf{a}}} + C(t_{i+\vec{\mathbf{a}}} + \eta'_{\vec{\mathbf{a}}})\right] \right) \quad \text{(C.13)}$$

For example, if i belongs to the A-sublattice, taking into account that in that case $i + \vec{\mathbf{a}} \in B$, we can write:

$$\mathsf{H}^t(I_{i\in A}) = (K\varepsilon, 0, 2J[A\, t_B m_A m_B + C\, t_B]) \quad \text{(C.14)}$$

The factor 2 comes from the two nearest-neighbor that the electron on site i has in the lattice. Here we should notice that the linear terms in $\eta_{\vec{\mathbf{a}}}$ and $\eta'_{\vec{\mathbf{a}}}$ vanish due to the fact that the sum in $\vec{\mathbf{a}}$ gives us a different sign for them depending on if $\vec{\mathbf{a}}$ points either in the x-direction ($\vec{\mathbf{a}} = (1, 0)$) or in the y-direction ($\vec{\mathbf{a}} = (0, 1)$). The partition function for this element will be:

$$\mathcal{Z}_A^t = e^{-\frac{1}{2}\beta E_A^t} + e^{\frac{1}{2}\beta E_A^t} \quad \text{(C.15)}$$

where E_i^t is defined as the modulus of the molecular vector $\mathsf{H}^t(I_i)$:

$$E_i^t = \sqrt{K^2\varepsilon^2 + 4J^2(A\, t_{i+\vec{\mathbf{a}}} m_i m_{i+\vec{\mathbf{a}}} + C\, t_{i+\vec{\mathbf{a}}})^2} \quad \text{(C.16)}$$

For $i \in A$ we have $E_A^t = \sqrt{K^2\varepsilon^2 + 4J^2(A\, t_B m_A m_B + C\, t_B)^2}$. The $\mathcal{Z}_A^t$ partition function is then:

$$\mathcal{Z}_A^t = 2\cosh\left[\frac{\beta}{2}\sqrt{K^2\varepsilon^2 + 4J^2(A\, t_B m_A m_B + C\, t_B)^2}\right] \quad \text{(C.17)}$$

An equivalent result is obtained for $\mathcal{Z}_B^t$ by just interchanging $t_A \leftrightarrow t_B$ in the previous expression.

Similarly we have for the spin component:

$$\mathsf{H}^s(S_i) = \left(0, 0, \sum_{\vec{\mathbf{a}}} J[A\, t_i t_{i+\vec{\mathbf{a}}} m_{i+\vec{\mathbf{a}}} + A\, \eta_{\vec{\mathbf{a}}}\, (t_i + t_{i+\vec{\mathbf{a}}}) m_{i+\vec{\mathbf{a}}} + \Delta m_{i+\vec{\mathbf{a}}}]\right) \quad \text{(C.18)}$$

where we have called

$$\Delta = B + A\, \eta_{\vec{\mathbf{a}}}^2 \quad \text{(C.19)}$$

.

In this case with $H = 0$ there is no necessity to take $\mathsf{H}^s(S_i)$ as a vector, but we keep this form to make contact with the next case where a transverse magnetic field is coupled to the spin degrees of freedom. We can write:

$$E_i^s = 2J\left(A\, t_i t_{i+\vec{\mathbf{a}}} m_{i+\vec{\mathbf{a}}} + \Delta m_{i+\vec{\mathbf{a}}}\right) \tag{C.20}$$

and following the same procedure we obtain:

$$\mathcal{Z}_A^s = 2\cosh\left[\beta J(A\, t_A t_B m_B + \Delta m_B)\right] \tag{C.21}$$

and similar results for $\mathcal{Z}_B^s$ by just interchanging $m_A \leftrightarrow m_B$. The total one-particle partition function will be defined as:

$$\mathcal{Z} = e^{-\beta E_0}\, \mathcal{Z}_A^t \mathcal{Z}_B^t \mathcal{Z}_A^s \mathcal{Z}_B^s \tag{C.22}$$

where E_0 was given in Eq.(5.18). If F sets for the total free energy of the system, the free energy per site $\mathcal{F} = F/N$, where $N = N_A + N_B$ is the total number of holes, would be:

$$\mathcal{F} = -\frac{1}{\beta}\ln\mathcal{Z} = E_0 - \frac{1}{\beta}\left(\ln\mathcal{Z}_A^t + \ln\mathcal{Z}_B^t + \ln\mathcal{Z}_A^s + \ln\mathcal{Z}_B^s\right) \tag{C.23}$$

and

$$\begin{aligned}
\mathcal{F} = J\left[-6A\, t_A t_B m_A m_B - 2\Delta m_A m_B - 2C\, t_A t_B + 2C\, \eta_{\vec{\mathbf{a}}}'^{\,2} + 2D\right] + \frac{G}{2}\varepsilon^2 + \frac{b}{4}\varepsilon^4 \\
-\frac{1}{\beta}\ln\left[2\cosh\left[\frac{\beta}{2}\sqrt{K^2\varepsilon^2 + 4J^2(A\, t_B m_A m_B + C\, t_B)^2}\right]\right] \\
-\frac{1}{\beta}\ln\left[2\cosh\left[\frac{\beta}{2}\sqrt{K^2\varepsilon^2 + 4J^2(A\, t_A m_A m_B + C\, t_A)^2}\right]\right] \\
-\frac{1}{\beta}\ln\left[2\cosh\left[\beta J(A\, t_A t_B m_B + \Delta m_B)\right]\right] \\
-\frac{1}{\beta}\ln\left[2\cosh\left[\beta J(A\, t_A t_B m_A + \Delta m_A)\right]\right]
\end{aligned} \tag{C.24}$$

Now we can define the staggered and uniform components of the order parameters as

$$\begin{array}{cc} t_0 = \frac{t_A + t_B}{2} & t_s = \frac{t_A - t_B}{2} \\ m_0 = \frac{m_A + m_B}{2} & m_s = \frac{m_A - m_B}{2} \end{array} \tag{C.25}$$

In the present case the isospin order has the higher transition temperature for realistic values of the parameters in hamiltonian[99] Eq.(5.3). Then in the region where ε is still zero, we have antiferro-orbital order (AFO) below a given critical temperature T_{AFO} and for some lower temperature T_{FM} also the ferromagnetic order (FM) appears. If we switch on the distortion, letting ε to be finite, this will set a ferro-orbital order (FO) below T_{FO}, where ε shows up, and a magnetic

order at some lower temperature. The nature of this magnetic order will depend on the value of the parameter α and, more specifically, on the sign of the function $A\,\eta_{\vec{\mathbf{a}}}^2 + B$. As a result, we will have a transition either to a FM order if $\alpha \leq 0.535$, or to a AFM order if $\alpha \geq 0.535$.

C.1.1 Non-distorted case: $\varepsilon = 0$.

In this case $t_s = t_A = -t_B$, and $m_0 = m_A = m_B$. The free energy for this case can be written, using Eq.(C.24):

$$\begin{aligned}\mathcal{F} = J\left[6A\,t_s^2 m_0^2 - 2\Delta m_0^2 + 2C\,t_s^2 + 2C\,\eta_{\vec{\mathbf{a}}}'^2 + 2D\right] + \frac{G}{2}\varepsilon^2 + \frac{b}{4}\varepsilon^4 \\ -\frac{2}{\beta}\ln\left[2\cosh\left[\beta J(A\,t_s m_0^2 + C\,t_s)\right]\right] \\ -\frac{2}{\beta}\ln\left[2\cosh\left[\beta J(-A\,t_s^2 m_0 + \Delta m_0)\right]\right] \qquad \text{(C.26)}\end{aligned}$$

From this free energy Eq.(C.26), and using the fact that $T_{AFO} > T_{FM}$, it is possible to obtain the expressions for the critical temperatures of the AFO and FM phases given in Section5.7.1.

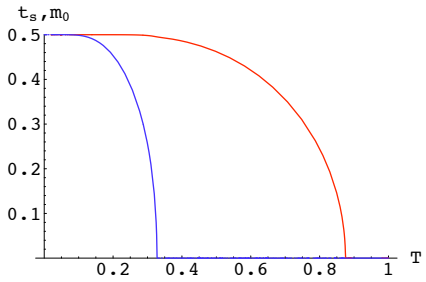

Figure C.1: Staggered isospin (red line) and uniform spin (blue line) components as a function of temperature for $\alpha = 0.5$ and $K = 0$.

If we minimize the free energy with respect to t_s and m_0 and plot the results, we find the curves shown in Fig.[C.1].

C.1.2 Distorted case: $\varepsilon > 0$.

In this section we develop the mean field equations used in Sec.5.7.1. As we pointed out above there is a transition to a FM order for $\alpha \leq 0.535$, and to an AFM order for $\alpha \geq 0.535$. The free energy for the first case ($\alpha \leq 0.535$) can be written as

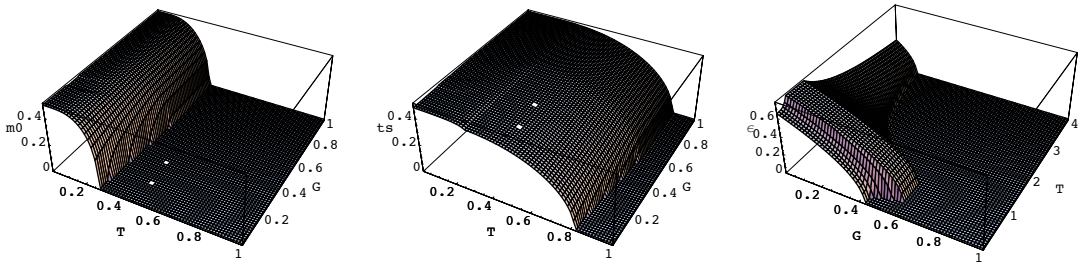

Figure C.2: $T-G$-plot of t_s (left), m_0 (center) and ε (right) for $\alpha = 0.5$. Notice that, for a better visualization of the curves, the T and G axes are interchanged in the right graph with respect to the two other.

$$\begin{aligned}\mathcal{F} = & J\left[6A\,t_s^2 m_0^2 - 2\Delta m_0^2 + 2C\,t_s^2 + 2C\,\eta_{\vec{\mathbf{a}}}'^2 + 2D\right] + \frac{G}{2}\varepsilon^2 + \frac{b}{4}\varepsilon^4 \\ & -\frac{2}{\beta}\ln\left[2\cosh\left[\frac{\beta}{2}\sqrt{K^2\varepsilon^2 + 4J^2(At_s m_0^2 + Ct_s)^2}\right]\right] \\ & -\frac{2}{\beta}\ln\left[2\cosh\left[\beta J(-At_s^2 m_0 + \Delta m_0)\right]\right] \end{aligned} \tag{C.27}$$

In this case we can plot the mean field parameters t_s, m_0 and ε as a function of T and G. For this case we obtain the results shown in Fig.[C.2]. Here we can see three second order transitions for the three order parameters (t_s, m_0 and ε). Similarly as in the previous section, the FO and FM transition temperatures can be calculated, giving the results shown in Sec.5.7.1.

C.2 Applied magnetic field: Metamagnetic transition

Now we apply an external magnetic field in the x-direction that enters in our hamiltonian by the term $\mathcal{H}_{mag} = -\mu_B H \sum_i S_i^x$. The mean-field decomposition can be done in the same way than in the previous sections but taking also into account the x-component of the spins in $\mathcal{H}_1$:

$$\mathcal{H}_1 = J\sum_{i,\vec{\mathbf{a}}}\left[A(I_{i+\vec{\mathbf{a}}}^z + \eta_{\vec{\mathbf{a}}})(I_i^z + \eta_{\vec{\mathbf{a}}}) + B\right](S_{i+\vec{\mathbf{a}}}^x S^x + S_{i+\vec{\mathbf{a}}}^z S^z) \tag{C.28}$$

This term leads to a molecular field vector $\mathsf{H}^t(I_i)$,

$$\mathsf{H}^t(I_i) = \left(K\varepsilon, 0, \sum_{\vec{\mathbf{a}},\alpha=x,z} J\left[A\, t_{i+\vec{\mathbf{a}}} m_i^\alpha m_{i+\vec{\mathbf{a}}}^\alpha + A\,\eta_{\vec{\mathbf{a}}}\, m_i^\alpha m_{i+\vec{\mathbf{a}}}^\alpha + C(t_{i+\vec{\mathbf{a}}} + \eta'_{\vec{\mathbf{a}}})\right] \right) \tag{C.29}$$

and $\mathsf{H}^s(S_i)$,

$$\mathsf{H}^s(S_i) = (\mathsf{H}_x^s(S_i), 0, \mathsf{H}_z^s(S_i)) \tag{C.30}$$

where

$$\begin{aligned}
\mathsf{H}_x^s(S_i) &= -\mu_B H + \sum_{\vec{\mathbf{a}}} J[A\, t_i t_{i+\vec{\mathbf{a}}} m_{i+\vec{\mathbf{a}}}^x + A\,\eta_{\vec{\mathbf{a}}}\,(t_i + t_{i+\vec{\mathbf{a}}}) m_{i+\vec{\mathbf{a}}}^x + \Delta m_{i+\vec{\mathbf{a}}}^x] \\
\mathsf{H}_z^s(S_i) &= \sum_{\vec{\mathbf{a}}} J[A\, t_i t_{i+\vec{\mathbf{a}}} m_{i+\vec{\mathbf{a}}}^z + A\,\eta_{\vec{\mathbf{a}}}\,(t_i + t_{i+\vec{\mathbf{a}}}) m_{i+\vec{\mathbf{a}}}^z + \Delta m_{i+\vec{\mathbf{a}}}^z]
\end{aligned} \tag{C.31}$$

We have used the notation for the mean-fields $\langle S_i^\alpha \rangle = m_i^\alpha$, with $\alpha = x, z$. Due to the presence of the magnetic field, we will have a uniform component of the magnetization in the transverse direction $m_A^x = m_B^x = m_0$, and a staggered component in the z-direction, $m_A^z = -m_B^z = m_s$. The free energy for this more general case is that given in Eq.(5.22):

Here we have again two competing configurations: FO + AFM for small values of G, that correspond to a finite distortion $\varepsilon > 0$ (we will label this configuration as II, for convenience in a future connection of the theoretical to the experimental phase diagram), and AFO + FM for larger values of G, that corresponds to a zero distortion $\varepsilon = 0$ (that we will label for the same reasons as III). From the extremal condition of the free energy Eq.(5.22), $\partial_\phi \mathcal{F} = 0$, with $\phi = t_s, m_0, m_s, \varepsilon$, we can obtain the next two set of self-consistent equations:

- Self-consistent equations for region-II

$$\begin{aligned}
\left.\frac{\partial \mathcal{F}}{\partial m_0}\right|_{t_s=0} &= -2m_0\Delta - \frac{\Delta(-\mu_B H + 2Jm_0\Delta)}{h_1(m_0, m_s)} \tanh\left[\frac{h_1(m_0, m_s)}{2k_B T}\right] = 0 \\
\left.\frac{\partial \mathcal{F}}{\partial m_s}\right|_{t_s=0} &= m_s\Delta - \frac{J\, m_s \Delta^2}{h_1(m_0, m_s)} \tanh\left[\frac{h_1(m_0, m_s)}{2k_B T}\right] = 0 \\
\left.\frac{\partial \mathcal{F}}{\partial \varepsilon}\right|_{t_s=0} &= G\varepsilon + b\varepsilon^3 - K \tanh\left[\frac{K\varepsilon}{2k_B T}\right] = 0
\end{aligned} \tag{C.32}$$

- Self-consistent equations for region-III

$$
\begin{aligned}
\left.\frac{\partial \mathcal{F}}{\partial t_s}\right|_{m_s,\varepsilon=0} &= 2Ct_s + 6A\,t_s m_0^2 - (C + A\,m_0^2)\tanh\left[\frac{J(C + A\,m_0^2)t_s}{k_B T}\right] \\
&\quad -2t_s m_0 \tanh\left[\frac{h_2(m_0,t_s)}{2k_B T}\right] = 0 \\
\left.\frac{\partial \mathcal{F}}{\partial m_0}\right|_{m_s,\varepsilon=0} &= 6Am_0 t_s^2 - 2m_0\Delta - 2A\,m_0 t_s \tanh\left[\frac{J(C + A\,m_0^2)t_s}{k_B T}\right] \\
&\quad -(\Delta - t_s^2)\tanh\left[\frac{h_2(m_0,t_s)}{2k_B T}\right] = 0
\end{aligned}
\tag{C.33}
$$

where

$$
\begin{aligned}
h_1(m_0,m_s) &= \sqrt{4J^2 m_s^2\Delta^2 + (-\mu_B H + 2Jm_0\Delta)^2} \\
h_2(m_0,t_s) &= 2Jm_0(\Delta - t_s^2) - \mu_B H
\end{aligned}
\tag{C.34}
$$

From these set of mean-field equations, and for the case of zero magnetic field ($H = 0$), we obtain the phase diagram shown in Fig.[5.7(a)]. For a finite applied magnetic field ($H > 0$) we obtain the phase diagram represented in Fig.[5.7(b)]. In order to calculate these phase diagrams, we solved independently the two set of equations Eq.(C.32,C.33) for each point of the $T - G - H$ space and search for the solutions that has the minimum free energy.

Future work and research interests.

In the future I would like to deepen on the physics of the strongly correlated materials I have been working on, like cuprates and ruthenates. I am particularly interested on the non-analytic corrections to the Fermi liquid behavior of these systems due to their Fermi surface topology. For these systems I would like to do a more accurate calculation for the momentum dependence of the quasiparticle weight, the one particle spectral function as well as a more detailed analysis of the charge and spin polarizability. This could be highly improved by the application of a more powerful numerical method as the Dynamical Mean Field Theory is. For the renormalization group approach project, it would be interesting to extend the method developed for the anisotropic-pairing superconductivity to the case with a generic shape of the FS. This method could also be modified to study the phase diagram of a Bose-Fermi mixture of ultracold atoms confined in a two-dimensional optical lattice. Finally, the study of $Ca_{2-x}Sr_xRuO_4$ should be extended to understand more deeply the critical phenomena seen in the phase diagram for the $x = 0.5$ filling, which is believed to be at a quantum critical point.

Bibliography

[1] L. D. Landau, "The theory of a fermi liquid," Zh. Eksp. Teor. Fiz., vol. 30, p. 1058, 1956. [Sov. Phys. JETP 3 (1957) 920].

[2] L. D. Landau Zh. Eksp. Teor. Fiz., vol. 32, p. 59, 1957. [Sov. Phys. JETP 5 (1957) 101].

[3] L. D. Landau Sov. Phys. JETP, vol. 8, p. 70, 1959.

[4] Theory of Interacting Fermi Systems. Addison-Wesley, 1964.

[5] Elementary Excitations in Solids. Advanced Book Classics, Westview Press, 1966.

[6] The Theory of Quantum Liquids. Advanced Book Classics, Westview Press.

[7] A. A. Abrikosov, L. P. Gorkov, and I. E. Dzyaloshinski, Methods of quantum field theory in statistical physics. Dover, 1975.

[8] K. Flensberg and H. Bruus, Many-body quantum theory in condensed matter physics. Oxford University Press, 2004.

[9] A. Damascelli, Z. Hussain, and Z.-X. Shen Rev. Mod. Phys., vol. 63, p. 473, 2003.

[10] C. M. Varma, Z. Nussinov, and W. Saarloos Physics Reports, vol. 361, p. 267, 2002.

[11] J. G. Bednorz and K. A. Mller Z. Phys. B: Condens. Matter, vol. 64, p. 189, 1986.

[12] L. D. Landau Z. Phys., vol. 64, p. 629, 1930.

[13] L. Onsager Phil. Mag., vol. 43, p. 1006, 1952.

[14] P. W. Anderson Science, vol. 235, p. 1196, 1987.

[15] J. Hubbard Proc. R. Soc. London, vol. 276, p. 238, 1963.

[16] T. Valla, P. D. Johnson, Z. Yusof, B. Wells, Q. Li, S. M. Loureiro, R. J. Cavas, M. Mikami, Y. Mori, M. Yoshimura, and T. Sasaki, "Coherence-incoherence and dimensional crossover in layered strongly correlated metals," Nature, vol. 417, p. 627, 2002.

[17] E. Arrigoni Phys. Rev. B, vol. 61, p. 7909, 2000.

[18] S. Bierman, A. Georges, A. Lichtenstein, and T. Giamarchi Phys. Rev. Lett., vol. 83, p. 276405, 2001.

[19] T. Yoshida, X. J. Zhou, K. Tanaka, W. L. Yang, Z. Hussain, Z. X. Shen, A. Fujimori, S. Komiya, Y. Ando, H. Esaki, T. Kakeshita, and S. Uchida 2005.

[20] A. Kaminski, S. Rosenkranz, H. M. Fretwell, M. R. Norman, M. Randeria, J. C. Campuzano, J.-M. Park, Z. Z. Li, and H. Raffy Phys. Rev. B, vol. 73, p. 174511, 2006.

[21] I. Tsukada and S. Ono 2006.

[22] N. P. Armitage, F. Ronning, D. H. Lu, A. Damascelli, K. M. Shen, D. L. Feng, H. Eisaki, Z. X. Shen, P. K. Mang, N. Kanebo, M. Grven, Y. Onose, Y. Taguchi, and Y. Tokura Phys. Rev. Lett, vol. 88, p. 257001, 2002.

[23] N. J. C. Ingle, K. M. Shen, F. Baumberger, W. Meevasan, D. H. Lu, Z. X. Shen, A. Damascelli, S. Nakatsuji, Z. Q. Mao, Y. Maeno, T. Kimura, and Y. Tokura Phys. Rev. B, vol. 72, p. 205114, 2005.

[24] S. Zhou, M. Gao, H. Ding, P. A. Lee, and Z. Wang Phys. Rev. Lett., vol. 94, p. 206401, 2005.

[25] R. Roldán, M. P. López-Sancho, F. Guinea, and S.-W. Tsai Europhysics Letters, vol. 76, pp. 1165–1171, 2006.

[26] B. Valenzuela and M. A. H. Vozmediano Phys.Rev.B, vol. 63, p. 153103, 2001.

[27] A. Virosztek and J. Ruvalds Phys. Rev. B, vol. 42, p. 4064, 1990.

[28] A. H. C. Neto and E. Fradkin, "Bosonization of fermi liquids," Phys. Rev. B, vol. 49, p. 10877, 1994.

[29] J. Fjaerestad, A. Sudbo, and A. Luther Phys. Rev. B, vol. 60, p. 13361, 1999.

[30] A. Neumayr and W. Metzner Phys. Rev. B, vol. 67, p. 035112, 2003.

[31] S. Ledowski and P. Kopietz, "Exact integral equation for the renormalized fermi surface," J. Phys.: Condens. Matter, vol. 15, p. 4779, 2003.

[32] H. Freire, E. Corrêa, and A. Ferraz Phys. Rev. B, vol. 71, p. 165113, 2005.

[33] M. Civelli, M. Capone, S. Kancharla, O. Pacollet, and G. Kotliar Phys. Rev. Lett., vol. 95, p. 106402, 2005.

[34] R. Shankar Rev. Mod. Phys., vol. 66, p. 129, 1994.

[35] W. Metzner, C. Castellani, and C. di Castro Adv. Phys., vol. 47, p. 3, 1998.

[36] A. A. Kordyuk, S. V. Borishenko, A. Koitzsch, J. Fink, M. Knupfer, and H. Berger Phys. Rev. B, vol. 71, p. 214513, 2005.

[37] H. Q. Lin and J. E. Hirsch Phys. Rev. B, vol. 35, p. 3359, 1987.

[38] A. A. Katanin and A. P. Kampf Phys. Rev. B, vol. 68, p. 195101, 2003.

[39] A. T. Zheleznyak, V. M. Yakovenko, and I. E. Dzyaloshinskii Phys. Rev. B, vol. 55, p. 3200, 1997.

[40] F. V. Abreu and B. Doucot Europhys. Lett., vol. 38, p. 533, 1997.

[41] A. Ferraz Europhys. Lett., vol. 61, p. 228, 2003. A. Ferraz, Phys. Rev. B **68**, 75115 (2003); H. Freire, E. Corrêa, and A. Ferraz, cond-mat/0304347.

[42] J. Labbé and J. Bok Europhys. Lett., vol. 3, p. 1225, 1987.

[43] J. Friedel J. Phys. (Paris), vol. 48, p. 1787, 1987.

[44] J. E. Dzyaloshinskii Pis'ma Zh. Eksp. Teor. Fiz., vol. 46, p. 118, 1987. [JETP Lett. **46**, 118 (1987)].

[45] H. J. Schulz Europhys. Lett., vol. 4, p. 609, 1987.

[46] F. Lederer, G. Montambaux, and D. Poilblanc J. Phys. (Paris), vol. 48, p. 1613, 1987.

[47] R. S. Markiewicz and B. G. Giessen Physica (Amsterdam), vol. 160C, p. 497, 1989.

[48] D. M. Newns, H. R. Krishnamurthy, P. C. Pattnaik, C. C. Tsuei, and C. L. Kane, "Saddle-point pairing: An electronic mechanism for superconductivity," Phys. Rev. Lett., vol. 69, p. 1264, 1992.

[49] J. González, F. Guinea, and M. A. H. Vozmediano Europhys. Lett., vol. 34, p. 711, 1996.

[50] J. González, F. Guinea, and M. A. H. Vozmediano, "Instability of anisotropic fermi surfaces in two dimensions," Phys. Rev. Lett., vol. 79, p. 3514, 1997.

[51] S. Fratini and F. Guinea, "Electronic susceptibilities in systems with anisotropic fermi surfaces," Phys. Rev. B, vol. 66, p. 125104, 2002.

[52] R. Hlubina and T. M. Rice, "Resistivity as a function of temperature for models with hot spots on the fermi surface," Phys. Rev. B, vol. 51, p. 9253, 1995.

[53] J. González, "Charge instabilities near a van hove singularity," Phys. Rev. B, vol. 045114, p. 63, 2001.

[54] V. Y. Irkhin, A. A. Katanin, and M. I. Katsnelson, "Robustness of the van hove scenario for high-tc superconductors," Phys. Rev. Lett., vol. 89, p. 076401, 2002. (the pinning found in this reference depends on the existence of an almost flat dispersion relation near the saddle point).

[55] P. Krotkov and A. V. Chubukov Phys. Rev. Lett., vol. 96, p. 107002, 2006.

[56] T. Valla, A. V. Fedorov, P. D. Johnson, Q. Li, G. D. Gu, and N. Koshizuka Phys. Rev. Lett, vol. 85, p. 828, 2000.

[57] A. Kaminski, H. M. Fretwell, M. R. Norman, M. Randeria, R. Rosenkrans, U. Chatterjee, J. C. Campuzano, J. Mesot, T. Sato, T. Takahashi, T. Terashima, M. Takano, K. Kadowaki, Z. Z. Li, and H. Raffy Phys. Rev. B, vol. 71, p. 014517, 2005.

[58] S. Ozcan, P. J. Turner, J. R. Waldra, R. J. Drost, P. H. Kes, and D. M. Broun Phys. Rev. B, vol. 73, p. 064506, 2006.

[59] A. A. Katanin and A. P. Kampf Phys. Rev. Lett., vol. 93, p. 106406, 2004.

[60] H. Freire, E. Corrêa, and A. Ferraz Physica C, vol. 408-410, p. 254, 2004.

[61] A. V. Chubukov and A. J. Millis 2006.

[62] A. P. Mackenzie and Y. Maeno Rev. Mod. Phys., vol. 75, p. 657, 2003.

[63] T. M. Rice and M. Sigrist J. Phys. Cond. Matter, vol. 7, p. L643, 1995.

[64] C. Bergeman, A. P. Mackenzie, S. R. Julian, D. Forsyte, and E. Ohmicho Adv. Phys., vol. 52, p. 639, 2003.

[65] A. D. *et al.* Phys. Rev. Lett., vol. 85, p. 5194, 2000.

[66] B. Binz and M. Sigrist Europhys. Lett., vol. 65, p. 816, 2004.

[67] A. K. *et al.* Nat. Phys., vol. 2, p. 447, 2006.

[68] J. Graf, G.-H. Gweon, K. McElroy, S. Y. Zhou, C. Jozwiak, E. Rotenberg, A. Bill, T. Sasagawa, H. Eisaki, S. Uchida, H. Takagi, D.-H. Lee, and A. Lanzara Phys. Rev. Lett., vol. 98, p. 067004, 2007.

[69] K. Novoselov Science, vol. 306, p. 666, 2004.

[70] K. Novoselov, A. Geim, S. Morozov, D. Jiang, M. Katsnelson, I. Grigorieva, S. Dubonos, and A. Firsov Nature, vol. 438, p. 197, 2005.

[71] Y. Zhang, Y.-W. Tan, H. Stormer, and P. Kim Nature, vol. 438, p. 201, 2005.

[72] P. R. Wallace Phys. Rev., vol. 71, p. 622, 1947.

[73] S. Y. Zhou, G. H. Gweon, C. D. Spataru, J. Graf, D.-H. L. andSteven G. Louie, and A. Lanzara Phys. Rev. B, vol. 71, p. 161403(R), 2005.

[74] S. Y. Zhou, G. H. Gweon, J. Graf, A. V. Fedorov, C. D. Spataru, R. D. Diehl, Y. Kopelevich, D. H. Lee, S. G. Louie, and A. Lanzara Nature Physics, vol. 2, p. 595, 2006.

[75] A. T. T. K. Sugawara, T. Sato and H. Suematsu Phys. Rev. Lett., vol. 98, p. 036801, 2007.

[76] A. Gruneis, C. Attaccalite, T. Pichler, V. Zabolotnyy, H. Shiozawa, S. Molodtsov, D. Inosov, A. Koitzsch, M. Knupfer, J. Schiessling, R. Follath, R. Weber, P. Rudolf, L. Wirtz, and A. Rubio 2007.

[77] A. Bostwick, T. Ohta, T. Seyller, K. Horn, and E. Rotenberg Nature Physics, vol. 3, p. 36, 2007.

[78] J. L. McChesney, A. Bostwick, T. Ohta, K. V. Emtsev, T. Seyller, K. Horn, and E. Rotenberg 2007.

[79] C. Bena and S. A. Kievelson Phys. Rev. B, vol. 72, p. 125432, 2005.

[80] J. González, F. Guinea, and M. A. H. Vozmediano Nucl. Phys., vol. 406, p. 771, 1993.

[81] E. H. Hwang, B. Y.-K. Hu, and S. D. Sarma 2007.

[82] S. D. Sarma, E. H. Hwang, and W.-K. Tse Phys. Rev. B, vol. 75, p. 121406, 2007.

[83] Y. Barlas, T. Perg-Barnea, M. Polini, R. Asgari, and A. MacDonald Phys. Rev. Lett., vol. 98, p. 236601, 2007.

[84] J. Blinowski, N. H. Hau, C. Rigaux, J. P. Vieren, R. L. Toullec, G. Furdin, A. Herold, and J. Melin J. Phys. (Paris), vol. 41, p. 47, 1980.

[85] K. W. K. Shung Phys. Rev. B, vol. 34, p. 979, 1986.

[86] M. F. Lin, C. S. Huang, and D. S. Chuu Phys. Rev. B, vol. 55, p. 13961, 1997.

[87] J. González, F. Guinea, and M. A. H. Vozmediano Phys. Rev. B, vol. 59, p. R2477, 1999.

[88] D. S. D. *et al.* Phys. Rev. Lett., vol. 71, p. 2781, 1993.

[89] R. Roldán, M. López-Sancho, and F. G. an S.-W. Tsai Phys. Rev. B, vol. 74, p. 235109, 2006.

[90] J. L. McChesney, A. Bostwick, T. Ohta, K. V. Emtsev, T. Seyller, K. Horn, and E. Rotenberg

[91] T. Tokura and N. Nagaosa Science, vol. 288, p. 462, 2000.

[92] A. Koga, N. Kawakami, T. M. Rice, and M. Sigrist Phys. Rev. Lett., vol. 92, p. 216402, 2004.

[93] S. Nakatsuji. PhD thesis, Kyoto University, 2000.

[94] M. Kriener, P. Steffens, J. Baier, O. Schumann, T. Zabel, T. Lorenz, O. Friedt, R. Muller, A. Gukasov, P. G. Radaelli, P. Reutler, A. Revcolevschi, S. Nakatsuji, Y. Maeno, and M. Braden Phys. Rev. Lett., vol. 95, p. 267403, 2005.

[95] J. Baier, P. Steffens, O. Schumann, M. Kriener, S. Stark, H. Hartmann, O. Friedt, A. Revcolevschi, P. G. Radaelli, S. Nakatsuji, Y. Maeno, J. A. Mydosh, T. Lorenz, and M. Branden 2006.

[96] M. Sigrist, "Notes of school," tech. rep.

[97] S. Nakatsuji, D. Hall, L. Balicas, Z. Fisk, K. Sugahara, M. Yoshioka, and Y. Maeno Phys. Rev. Lett., vol. 90, p. 137202, 2003.

[98] S. Nakatsuji and Y. Maeno Phys. Rev. B, vol. 62, p. 6458, 2000.

[99] V. I. Anisimov, I. A. Nekrasov, D. E. Kondakov, T. M. Rice, and M. Sigrist Eur. Phys. J. B, vol. 25, p. 191, 2002.

[100] A. Liebsch Europhys. Lett., vol. 63, p. 97, 2003.

[101] X. Dai, G. Kotliar, and Z. Fang cond-mat/0611075.

[102] S. Sachdev, Quantum phase transitions. Cambridge, 1999.

[103] R. Blinc and B. Zeks. Amsterdam: North-Holland.

[104] M. Sigrist and M. Troyer Eur. Phys. J. B, vol. 39, p. 207, 2004.

[105] W. Metzner, C. Castellani, and C. D. Castro Adv. Phys., vol. 47, pp. 317–445, 1998.

[106] J. González, F. Guinea, and M. A. H. Vozmediano Nucl. Phys. B, vol. 485, p. 694, 1997.

[107] R. Shankar Rev. Mod. Phys., vol. 66, p. 129, 1994.